UNIVERSIDADE FEDERAL DO CEARÁ

TECHNOLOGY CENTER

DEPARTMENT OF STRUCTURAL ENGINEERING AND CIVIL CONSTRUCTION

GRADUATE PROGRAM IN CIVIL ENGINEERING: STRUCTURES AND CIVIL CONSTRUCTION

MASTERS OF SCIENCE IN CIVIL ENGINEERING

MARINA ALVES MAIA

SEQUENTIAL APPROXIMATE OPTIMIZATION OF COMPOSITE STRUCTURES

FORTALEZA

2020

MARINA ALVES MAIA

SEQUENTIAL APPROXIMATE OPTIMIZATION OF COMPOSITE STRUCTURES

Dissertation submitted to the Course of Masters of Science in Civil Engineering of the Graduate Program in Civil Engineering: Structures and Civil Construction of the Technology Center of the Universidade Federal do Ceará, as partial fulfillment of the requirements for the degree of Master in Civil Engineering. Area of concentration: Structures

Advisor: Prof. D. Sc. Evandro Parente Junior

Co-advisor: Prof. D. Sc. Antônio Macário Cartaxo de Melo

FORTALEZA

2020

Dados Internacionais de Catalogação na Publicação
Universidade Federal do Ceará
Biblioteca Universitária
Gerada automaticamente pelo módulo Catalog, mediante os dados fornecidos pelo(a) autor(a)

M187s Maia, Marina Alves.
Sequential Approximate Optimization of Composite Structures / Marina Alves Maia. – 2020.
121 f. : il. color.

Dissertação (mestrado) – Universidade Federal do Ceará, Centro de Tecnologia, Programa de Pós-Graduação em Engenharia Civil: Estruturas e Construção Civil, Fortaleza, 2020.
Orientação: Prof. Dr. Evandro Parente Junior.
Coorientação: Prof. Dr. Antônio Macário Cartaxo de Melo.

1. Composite materials. 2. Surrogate model. 3. Sequential Approximate Optimization. I. Título.
CDD 624.1

MARINA ALVES MAIA

SEQUENTIAL APPROXIMATE OPTIMIZATION OF COMPOSITE STRUCTURES

Dissertation submitted to the Course of Masters of Science in Civil Engineering of the Graduate Program in Civil Engineering: Structures and Civil Construction of the Technology Center of the Universidade Federal do Ceará, as partial fulfilment of the requirements for the degree of Master in Civil Engineering. Area of concentration: Structures

Approved on __/__/__.

EXAMINING BOARD

_____

Prof. Evandro Parente Junior, D.Sc. (Advisor)

Universidade Federal do Ceará – UFC

_____

Prof. Antônio Macário Cartaxo de Melo D.Sc. (Co-advisor)

Universidade Federal do Ceará - UFC

_____

Prof. Marcelo Silva Medeiros Júnior, D.Sc.

Universidade Federal do Ceará – UFC

_____

Prof. Iuri Barcelos Carneiro Montenegro da Rocha, D.Sc.

Delft University of Technology - TU Delft

ACKNOWLEDGEMENTS

Em primeiro lugar, a Deus.

À minha mãe, Liduina Alves, e ao meu pai, Carmélio Maia, pelo apoio, amor incondicional e carinho em todos esses anos.

À minha família, pelo apoio, preocupação e cuidado diário. Em especial, à minha irmã, Mariana, e minhas tias, Palma e Jacinta.

Aos meus amigos que tive a sorte e o prazer de conhecer ao longo da graduação e que hoje continuam em minha vida. Poder compartilhar a vida com vocês foi e continua sendo uma enorme alegria para mim, em especial, Wendy Quintanilha, Carla Marília, Renan Maia, Gledson Mesquita, Geovanny Moreno e Augusto Tremarin.

Ao meu namorado, Luiz Henrique, pelo encorajamento, compreensão e carinho em mais esta jornada. Contar com seu apoio foi fundamental.

Aos colegas de laboratório do LMCV pela troca em todos esses anos que tanto contribuíram para a minha formação. Em especial, agradeço ao Elias Barroso, Leonardo Ribeiro e Samir Auad pela amizade e por serem sempre tão solícitos e pacientes.

Ao meu orientador, Evandro Parente, por ser exemplo de dedicação, compromisso e profissionalismo. Obrigada por compartilhar tanto nesses 6 anos de pesquisa.

Ao meu coorientador, Antônio Macário, pelas contribuições e ensinamentos valiosos em sala de aula desde a graduação.

Aos professores Marcelo e Iuri por aceitarem fazer parte da minha banca examinadora.

À UFC, DEECC, LMCV e FUNCAP, pelo apoio financeiro para a realização deste trabalho.

ABSTRACT

The design of composite structures is of relevance in many fields of engineering (civil, naval, aerospace, automobile, etc.) and as such has become an active research field. To fully explore the benefits of using composite materials, optimization techniques are often needed. However, the computational cost of the structural analyses may become a hindrance for the optimization process. This is especially critical when dealing with bio-inspired algorithms, where a high number of trial designs are typically employed. Thus, surrogate models are a valuable alternative to help reduce computational cost and enable the optimization of complex structures. In this work, two surrogate models were studied: Radial Basis Function (RBF) and Kriging. Both surrogate models were used in association with an optimization technique known as Sequential Approximate Optimization (SAO), in which the approximate response surface is continuously updated and improved by the addition of new points in the design space. For that matter, two infill criteria were assessed: the Expected Improvement (EI) and the Weight Expected Improvement (WEI). Both use the Particle Swarm Optimization to maximize their acquisition functions. To evaluate the structural response of the composite structures, the Isogeometric Analysis (IGA) was employed. A comparison between the SAO algorithms was carried out in terms of accuracy, efficiency, and robustness. The implementation was validated using a set of numerical examples from the literature. The examples include different types of structures using functionally graded and laminated composite materials. Results show the efficiency of the proposed algorithms and highlight the impact of the choice of the Infill Criterion on their performance. An expressive reduction in the number of High-Fidelity (HF) evaluations was obtained compared to traditional optimization, saving a significant amount of processing time. This is particularly promising when the structural analysis involves refined meshes or the consideration of nonlinear behaviour. In general, the RBF consistently provided the fastest surrogate model building and updating processes, while Kriging provided more accurate results with fewer HF evaluations in a wide range of applications.

Keywords: Composite materials. Surrogate Model. Sequential Approximated Optimization.

RESUMO

O projeto de estruturas de material compósito é de relevância em muitos campos da engenharia (civil, naval, aeroespacial, automobilística, etc.) e, como tal, tornou-se um tópico de pesquisa bastante ativo. De modo a potencializar os benefícios oriundos desse tipo de material, é necessário a utilização de técnicas de otimização. Contudo, o custo computacional das análises estruturais pode se apresentar como uma limitação para o processo de otimização. Este problema é particularmente crítico quando algoritmos bioinspirados são utilizados devido ao grande número de avaliações do modelo de alta fidelidade usualmente empregado. Dessa forma, os modelos substitutos (*surrogate models*) apresentam-se como uma alternativa valiosa para ajudar a reduzir o custo computacional e permitir a otimização de estruturas complexas. Neste trabalho, dois modelos substitutos são estudados: Funções de Base Radiais (*Radial Basis Function* - RBF) e Kriging. Estes foram incorporados a uma metodologia de otimização conhecida como Otimização Aproximada Sequencial (*Sequential Approximate Optimization* - SAO), onde a superfície de resposta aproximada é continuamente atualizada e melhorada pela inserção de novos pontos. Para isto, dois Critérios de Preenchimento foram avaliados: Melhoria Esperada e Melhoria Esperada Ponderada. Ambos utilizam o algoritmo de Otimização por Enxame de Partículas para maximizar suas funções de aquisição. Para obtenção das respostas estruturais do HFM, foi utilizada a Análise Isogeométrica. Uma comparação entre as diferentes metodologias é realizada em termos de precisão, eficiência e robustez. A verificação da implementação dos algoritmos SAO foi realizada com base em exemplos da literatura. Estes contemplam diferentes tipos de estruturas utilizando materiais com gradação funcional e estruturas de compósito laminado. Os resultados atestam a eficiência dos algoritmos propostos e evidenciam o impacto da escolha do Critério de Preenchimento no desempenho desses algoritmos. Uma expressiva redução no número de avaliações de alta fidelidade quando comparado à otimização tradicional foi obtida, o que resulta em uma significativa redução no esforço computacional. Isto é particularmente promissor quando a análise estrutural envolve malhas refinados ou a consideração do comportamento não-linear. Em geral, o RBF apresentou um processo mais rápido, tanto na construção quanto na atualização do modelo, enquanto o Kriging se destaca pela sua precisão com um menor número de avaliações de alta fidelidade em uma grande variedade de aplicações.

Palavras-chave: Materiais Compósitos. Modelo Substituto. Otimização Sequencial Aproximada.

LIST OF FIGURES

LIST OF ABBREVIATIONS AND ACRONYMS

ANN	Artificial Neural Networks
ASA	Active Set Algorithm
BIOS	Biologically Inspired Optimization System
CAD	Computer-Aided Design
CEI	Constrained Expected Improvement
CLT	Classical Lamination Theory
CPT	Classical Plate Theory
CV	Cross-Validation
DACE	Design and Analysis of Computer Experiments
DNN	Deep Neural Network
DoE	Design of Experiments
EGO	Efficient Global Optimization
EI	Expected Improvement
ES	Evolutionary Strategies
FAST	Finite element AnalyiS Tool
FEA	Finite Element Analysis
FG	Functionally Graded
FGM	Functionally Graded Materials
FPF	First-Ply Failure
FRC	Fibre-Reinforced Composites
FSDT	First-Order Shear Deformation Theory
GA	Genetic Algorithm
GS	Goal Seeking
HF	High-Fidelity
HFM	High-Fidelity Model
HSDT	Higher-Order Shear Deformation Theory
HSS	Hammersley Sequence Sampling
IGA	Isogeometric Analysis
LF	Likelihood Function
LH	Latin Hypercube
LHS	Latin Hypercube Sampling

LMCV	Laboratório de Mecânica Computacional e Visualização
LOOCV	Leave-One-Out Cross-Validation
MLE	Maximum Likelihood Estimation
MSE	Mean Squared Error
NRMSE	Normalized Root Mean Squared Error
NURBS	Non-Uniform Rational B-Splines
OK	Ordinary Kriging
OLHS	Optimized Latin Hypercube Sampling
OOP	Object-Oriented Programming
PF	Probability of Feasibility
PI	Probability of Improvement
PR	Polynomial Regression
PSO	Particle Swarm Optimization
RBF	Radial Basis Functions
RMSE	Root Mean Squared Error
SAO	Sequential Approximate Optimization
SF	Safety Factor
SQP	Sequential Quadratic Programming
SVR	Support Vector Regression
TTO	Tamura–Tomota–Ozawa
WEI	Weighted Expected Improvement

CONTENTS

1 INTRODUCTION

Composite materials brought significant advances for a wide range of applications in industries such as naval, aeronautical and civil [1]. These materials present lightweight properties, good fatigue and corrosion resistance, among other desired properties for high-performance structures [2]. This work will address two types of composite materials: Fibre-Reinforced Composites (FRC) and Functionally Graded Materials (FGM).

FRC are often manufactured in the form of thin layers, also referred to as *plies*, stacked in a specific sequence to achieve a set of performance requirements usually regarding strength and stiffness. These materials present higher stiffness/density and strength/density ratios compared to the traditional engineering materials (e.g. steel and concrete) and feature good thermal insulation properties and fatigue resistance [3]. Despite their excellent mechanical behaviour, these materials are not suitable for high temperature environments. In this scenario, the variation of the coefficient of thermal expansion can generate high residual stresses and damage onset, resulting in catastrophic failure of the structure (e.g. fracture and delamination). Furthermore, traditional FRC with polymeric resin cannot withstand high-temperatures [4, 5].

In such situation, FGM are a valuable and promising alternative. These materials were initially developed in Japan in the 1980s as a means of creating a thermal barrier for aerospace structures and fusion reactors [6]. The smoothly varying composition of FGM allows the elimination of the stress discontinuity problem, which, in laminated composites, can cause failure by delamination and consequent failure of the load transfer mechanism [7, 8].

A typical Functionally Graded (FG) material consists of an inhomogeneous composite made of two or more constituents (phases). The different microstructural phases have distinct functions and depending on the volume fraction distribution, different mechanical behaviour is observed [7]. For the well-known ceramic-metal combination, the ceramic is in charge of the thermal resistance and the metal is in charge of the strong mechanical performance and helps mitigate brittle failure. Of course, FGM are now broadly used for purposes other than being super refractory materials. Applications such as biomedical implants, rotating disks and solar power systems are reported in the literature [9, 10, 11].

Both laminated composites and FGM offer high tailorability in their manufacturing, which makes them an interesting topic for optimization purposes. Nikbakht *et al.*[12] and Nikbakt *et al.*[13] present a two-part review of publications on the optimization of FG and laminated structures, respectively. Among the highlighted works, Hussein and Mulani[14] argue that FG

structures could benefit from the minimization of the amount of required reinforcements (e.g. silicon carbide nanoparticles and carbon nanotubes) since these materials are very costly. Likewise, FRC are frequently employed to the optimization of plates, shells and beams, usually dealing with the maximization of the load-carrying capacity, buckling and frequency and minimization of mass or cost.

In many applications, the structural response of composite plates, beams and shells cannot be assessed by closed-form solutions. And even when this type of solution is available, either the geometry, the loading or the support conditions are very simple (i.e. no curved edges or cutouts) [4]. For instance, in laminated composites, the buckling load of a simply supported plate can only be straightforwardly evaluated for cross-ply laminates. Any other case is either an approximation or must be obtained using approximated methods such as the Finite Element Analysis (FEA) or Isogeometric Analysis (IGA), the former being the most used method in the literature. Recently, a review on buckling and vibration of FG conical shells showed that most of the studies regarding these types of problems are solved by numerical methods [15].

Unfortunately, despite steady advances in computing power, FEA and IGA may impose a serious limitation on time and computational cost of engineering design optimization. This is particularly critical when population-based meta-heuristics are employed due to the high number of evaluations involved in the global search for the optimal design.

This class of algorithms is well-suited for problems with discrete variables (but is not restricted to) as they do not demand any information on the gradient of the function. In laminated composite problems, this may be an important feature since the design variables are often considered as discrete due to manufacturing constraints. Recently, Nikbakt *et al.*[13] argued that meta-heuristics such as Genetic Algorithm (GA) and Particle Swarm Optimization (PSO) are more popular due to their efficiency and stability. Furthermore, meta-heuristics algorithms are less prone to be trapped in local minima [16].

Faced with this challenge, the basic approach to overcome the high-cost analysis problem is to create a model capable of approximating the expensive function with a cheaper one. This new model is called *meta-model* or simply *surrogate model*. Surrogate models may be understood as approximate models to the objective functions and/or constraints built upon a limited number of observations of the exact response called *sampling points*. To take full advantage of this approach, the sampling points are chosen based on a Design of Experiments (DoE) technique.

The DoE is a group of stochastic and deterministic methodologies used for formulating the sampling plan, examples of it include the Latin Hypercube Sampling (LHS) and the Hammersley Sequence Sampling (HSS). The surrogate model is then used to predict points on the design space that were not yet evaluated at a lower computational cost if compared to that of running a FEA.

Several methodologies were proposed for building a surrogate model, among them are RBF, Kriging, Artificial Neural Networks (ANN) and Support Vector Regression (SVR). In this work, the RBF and Kriging are employed to approximate the High-Fidelity Model (HFM) responses of composite structures. These are two of the most extensively employed surrogate models in recent years and both were originated from the geostatistics community [17, 18].

Kriging is a very flexible surrogate model due to the wide range of correlation functions available and to the high number of model parameters. Kriging has many variants: Simple Kriging, Regression Kriging, Ordinary Kriging (OK) and Co-Kriging, the OK being the most commonly employed in the literature [19]. On the optimization of laminated composite structures, this surrogate model is rapidly gaining importance [20, 21, 22, 23, 24]. Unfortunately, the literature in still scarce regarding FG structures [25].

As for RBF, it consists of a surrogate model with a much lower computational cost compared to that of Kriging. It is also a simpler, yet robust, surrogate model. RBF are well adapted for numerical experiments with deterministic errors and was credited as the most dependable by Jin *et al.*[26] in a comparative study involving four different surrogate models, namely Polynomial Regression, Multivariate Regression Splines, RBF and Kriging.

In any case, a crucial aspect of surrogate modelling involves how the sampling plan will be treated. The most basic approach is to build a surrogate model with a fixed sampling plan only once and use it throughout the whole optimization process. In this case, a large number of sampling points are needed to produce reasonable approximations, which goes against the idea of reducing the computational cost.

On the other hand, when the initial sampling plan is updated, we have the so-called Sequential Approximate Optimization (SAO). In this approach, the sampling plan is continuously updated with points in the design space capable of improving the surrogate model accuracy near regions of interest, helping the algorithm find the global optimum. These points are called infill points (or *update points*) and the criterion used to select them is called *infill criterion* [18].

Alternatively, one may use parallelization techniques to reduce execution time.

Several authors have reported speed gains and improved algorithm performance in laminated composite optimization using these techniques [27, 28, 29, 30]. However, this approach demands high-performance clusters.

The present work aims to use SAO to find the optimum design of composite structures. In addition, the performance of two surrogate models (RBF and Kriging) is assessed considering different techniques for obtaining the basis functions parameters and different updating methodologies for the sampling plan. These combinations are compared in terms of accuracy and computational efficiency.

1.1 Aims and scope

This work aims to develop and implement a methodology for the optimal design of composite structures using the SAO approach. This will hopefully contribute to the improvement of the optimization performance of laminated and FG structures. In addition to that, the successful application of SAO algorithms can enable the optimization of more complex structures since the number of High-Fidelity (HF) responses may be significantly reduced. For this purpose, the following specific objectives are set:

a) to develop and implement a methodology for the optimization of FG and laminated plates and shells using SAO techniques;
b) to properly integrate analysis and optimization interfaces, providing routines to the evaluation of structural responses of composite structures;
c) to implement the Ordinary Kriging model;
d) to apply the proposed methodology to the optimization of composite structures using HFMs and surrogate models;
e) to implement infill criteria and compare the effect of these different methodologies on SAO performance in terms of accuracy, efficiency and robustness;
f) to compare the performance of different surrogate models, namely RBF and Kriging, using a set of appropriate metrics ($\overline{NRMSE}$, STD_{NRMSE}, Speed-up and $\overline{n}_p$);
g) to compare the SAO performance on composite structures problems with conventional optimization using the HFM.

1.2 Organization of the text

The remainder of this work is organized as follows: in Chapter 2 the main concepts and the mechanical behaviour of FGM and laminated composites are introduced, including the techniques used to assess the effective properties of FG structures and the laminate theory considered. In Chapter 3, the details of the structural analysis, including the kinematic assumptions, internal forces evaluation, and a brief description of the analysis framework adopted are discussed. In Chapter 4, a review of the state-of-art on the optimization of composite structures is presented, as well as a discussion on the Particle Swarm Optimization algorithm. In the following, Chapter 5 presents the mathematical formulation of the surrogate models herein explored. In Chapter 6, the main infill criteria in the literature are briefly discussed.

In Chapter 7, the numerical examples used to demonstrate the efficiency of the proposed algorithms are discussed. Finally, in Chapter 8, the concluding remarks and suggestions for future works are presented.

2 COMPOSITE MATERIALS

Reddy[5] describes composite materials as the combination of two or more materials, also known as *phases*, in macroscopic scale that together produces desirable properties that could not be obtained using any of its constituents alone. These phases are usually referred to as *matrix* and *reinforcement*. Four types of composites may be listed according to the combination of matrix and reinforcement: (i) particulate composite materials, in which the reinforcing constituent are the particles, (ii) fibrous composite materials, in which the reinforcing constituents are the fibres, (iii) laminated composite, which consists of layers of one or more materials stacked up and finally, (iv) the combination of some or all of the three previous types.

The fibre-reinforced composites are usually employed in high-performance structures in the form of laminated composites. In this type of structure, each ply presents distinct mechanical behaviour depending on the arrangement of the fibres in the matrix, as illustrated in Fig. 1. In addition to that, aspects such as fibre distribution, the volume fraction of the constituents and their respective mechanical properties also affect the mechanical behaviour of the laminate. Commonly, fibres are made of inorganic materials, such as glass, carbon and ceramics, but they can also be made of organic material such as polymers, while the matrix is commonly made of polymers, although it is possible to find them as metals or ceramics [3].

Figure 1 – Different fibre configurations for composite reinforcement

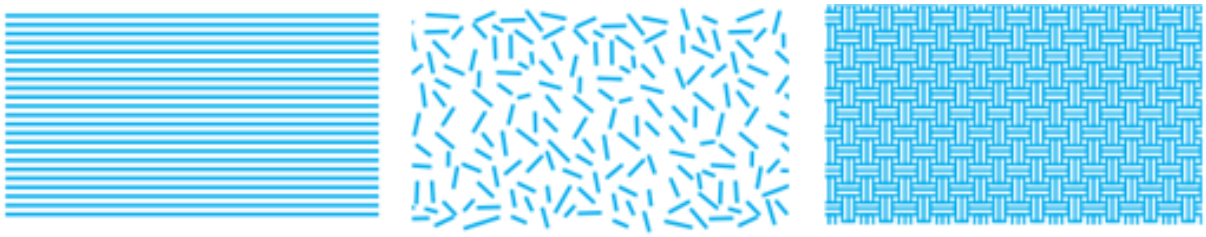

(a) Continuous (b) Discrete (or chopped) (c) Woven fabric

Source: National Chung Hsing University[31].

In this work, continuous and unidirectional fibres are considered. This is the typical choice when dealing with high-performance structures (e.g. aircrafts, ships, composite risers [32], etc.). In this case, fibres are the main load-carrying members, and the matrix should keep them together and act as a load-transfer medium between fibres. The matrix also protects fibres from exposure to the environment (e.g., moisture, abrasion, and corrosion).

Laminated composites can be easily tailored to meet specific design requirements by choosing the fibre orientation, the thickness, the constituent materials of each ply, and the

stacking sequence of the plies (also called *layup*).

As for the Functionally Graded Materials, these materials were initially designed in the 80s as a means of preparing thermal barrier materials through continuous changes in its composition, microstructure and porosity [33]. The reinforcement may be in the form of particulates, continuous or chopped fibres, whiskers and platelets [8], being the former the type addressed in this work.

Nowadays, the structural applications of FGM include beams [34] and plates [8] and secondary applications can be found in many forms such as biomedical implants [25] and rotating disks [10]. Just as FRC, FGM can be tailored for achieving specific structural requirements by varying the distribution of the constituents.

2.1 Fibre Reinforced Composites

A laminate stacking sequence can be roughly classified into the following types regarding the fibre orientation [35]:

i) Cross-ply: Special laminate that contains only 0° and 90° plies alternately, e.g. $[90^\circ/0^\circ/$ $/90^\circ/0^\circ]$;

ii) Angle-ply: Laminate with any fibre orientation angle, being at least one of them different from 0° and 90°, e.g. $[45^\circ/0^\circ/90^\circ]$.

Considering now the symmetry about the midplane (i.e. the equidistant plane from the outer surfaces of the laminate), a fibre-reinforced composite may be classified as:

i) Symmetric: Laminate where the lower half about the mid-plane is a mirror of the fibre orientations, material, thickness and distance from the midplane in relation to the upper half. These are usually identified with the subscript "s", as in $[-45^\circ/30^\circ/0^\circ]_s$, which refers to a six-layer laminate;

ii) Anti-symmetric: Laminate where the lower half about the midplane is a mirror of the materials and thickness, but the fibre orientations are the negative of the orientations in the upper half;

iii) Asymmetric: Laminate that presents no symmetry about the midplane;

iv) Balanced: Laminate that presents a negative fibre orientation for each positive one.

2.1.1 Mechanics of the laminate

The mechanical behaviour of a layer is studied in two levels: the macromechanics, in which fibre and matrix are treated as a single homogeneous material on a macroscopic scale and where the mechanical properties are assessed and 2) the micromechanics, in which the interaction of the constituents is examined on a microscopic scale, being useful in delineating the failure modes in FRC [36].

In a wider sense, the mechanical behaviour of the *laminate* is typically analyzed using either Equivalent Single Layer Theories (e.g. Classical Lamination Theory (CLT) and First-Order Shear Deformation Theory (FSDT)) or Layerwise Theories (e.g. Discrete Layer Theories and Zigzag theories). A recent and comprehensive review of such theories in the analysis of laminated composite plates has been presented by Maji and Mahato[37], including the 3D elasticity solutions. In this work, the FSDT is adopted.

This theory consists of an extension of the Reissner-Mindlin Plate Theory to laminated composite plates. The assumptions of FSDT are very similar to the ones in the CLT, but the former considers shear deformations in a simplified way by releasing the constraint on the angle of shear deformations. Based on Reissner-Mindlin's Theory, the transverse segments to the plate midplane remain straight and with the same length after deformation, but not necessarily perpendicular to the midplane after deformation, which results in $\varepsilon_z = 0$ and $\sigma_z = 0$ [4].

In laminates with unidirectional fibres, each ply is modeled with orthotropic behaviour in the coordinate system of the ply $(x_1;\ x_2;\ x_3)$, where x_1 is the fibre direction, x_2 is the direction perpendicular to the fibres in the plane of the ply and x_3 is the direction perpendicular to the ply. In addition to this local system, which varies according to each ply fibre orientation, it is considered a single global system for the laminate $(x;y;z)$, where z coincides with x_3, as illustrated in Fig. 2.

Figure 2 – Local and global axis for a single-ply

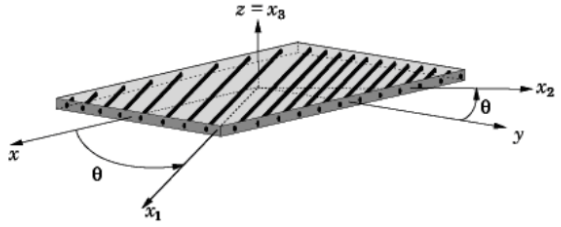

Source: Teófilo *et al.*[38].

Experimentally, it is known that the FRC behaviour until very close to failure may

be considered linear elastic [4]. Therefore, it can be described by the Generalized Hook's Law for orthotropic materials. Considering, the plane-stress state, the orthotropic behaviour of the ply and the symmetry of the constitutive matrices $\mathbf{Q}$ and $\mathbf{Q_s}$, we arrive at:

$$\begin{aligned} \sigma_1 = \mathbf{Q}\,\varepsilon_1 \quad &\Rightarrow \quad \begin{Bmatrix} \sigma_1 \\ \sigma_2 \\ \tau_{12} \end{Bmatrix} = \begin{bmatrix} Q_{11} & Q_{12} & 0 \\ Q_{12} & Q_{22} & 0 \\ 0 & 0 & Q_{66} \end{bmatrix} \begin{Bmatrix} \varepsilon_1 \\ \varepsilon_2 \\ \gamma_{12} \end{Bmatrix} \\ \tau_1 = \mathbf{Q}_s\gamma_1 \quad &\Rightarrow \quad \begin{Bmatrix} \tau_{13} \\ \tau_{23} \end{Bmatrix} = \begin{bmatrix} Q_{44} & 0 \\ 0 & Q_{55} \end{bmatrix} \begin{Bmatrix} \gamma_{13} \\ \gamma_{23} \end{Bmatrix} \end{aligned} \tag{2.1}$$

where the subscripts 1 refer to the local system of the ply and s to the transverse shear terms. The matrix coefficients Q_{ij} are given by:

$$\begin{aligned} &Q_{11} = \frac{E_1}{1-\nu_{12}\,\nu_{21}} \qquad Q_{12} = \frac{\nu_{21}\,E_1}{1-\nu_{12}\,\nu_{21}} \qquad Q_{22} = \frac{E_2}{1-\nu_{12}\,\nu_{21}} \\ &Q_{66} = G_{12} \qquad Q_{44} = G_{13} \qquad Q_{55} = G_{23} \end{aligned} \tag{2.2}$$

Note that the equilibrium equations for structural analysis are written in the global system, while the above equations are written in the local system. Therefore, one must use transformation matrices $\mathbf{T}$ and $\mathbf{T}_s$ to relate both systems as in:

$$\varepsilon_1 = \mathbf{T}\,\varepsilon \Rightarrow \begin{Bmatrix} \varepsilon_1 \\ \varepsilon_2 \\ \gamma_{12} \end{Bmatrix} = \begin{bmatrix} \cos^2\theta & \text{sen}^2\theta & \text{sen}\theta\cos\theta \\ \text{sen}^2\theta & \cos^2\theta & -\text{sen}\theta\cos\theta \\ -2\text{sen}\theta\cos\theta & 2\text{sen}\theta\cos\theta & \cos^2\theta - \text{sen}^2\theta \end{bmatrix} \begin{Bmatrix} \varepsilon_x \\ \varepsilon_y \\ \gamma_{xy} \end{Bmatrix} \tag{2.3}$$

$$\gamma_1 = \mathbf{T}_s\,\gamma \Rightarrow \begin{Bmatrix} \gamma_{13} \\ \gamma_{23} \end{Bmatrix} = \begin{bmatrix} \cos\theta & -\text{sen}\theta \\ \text{sen}\theta & \cos\theta \end{bmatrix} \begin{Bmatrix} \gamma_{xz} \\ \gamma_{yz} \end{Bmatrix} \tag{2.4}$$

Replacing Eq. (2.3) and Eq. (2.4) in Eq. (2.2) and applying the Principle of Virtual Work, the stress transformation can be simply obtained by pre-multiplying the stress in the local system by the transpose of $\mathbf{T}$ and $\mathbf{T}_s$. This way, the constitutive relation in the global system is given by:

$$\begin{aligned} &\sigma = \mathbf{T}^{\mathrm{T}}\,\mathbf{Q}\,\mathbf{T}\varepsilon \quad \Rightarrow \quad \sigma = \overline{\mathbf{Q}}\,\varepsilon \\ &\tau = \mathbf{T}_{\mathrm{s}}^{\mathrm{T}}\,\mathbf{Q}\,\mathbf{T}_{\mathrm{s}}\gamma \quad \Rightarrow \quad \tau = \overline{\mathbf{Q}}_{\mathrm{s}}\,\gamma \end{aligned} \tag{2.5}$$

where $\overline{\mathbf{Q}}$ and $\overline{\mathbf{Q}}_{\mathbf{s}}$ are the constitutive matrices in the global system.

Thus, depending on the fibre orientation and the material properties of each ply, the stress variation through the laminate is not necessarily linear despite the linear strain variation,

as illustrated in Fig. 3. This also explains the different failure modes of a laminate. In general, FRC may fail either by individual failure of one of its constituents or by its interface. Therefore, the consideration of an adequate failure criterion is crucial to ensure structural safety.

Figure 3 – Hypothetical variation of stress and strain through the laminate thickness

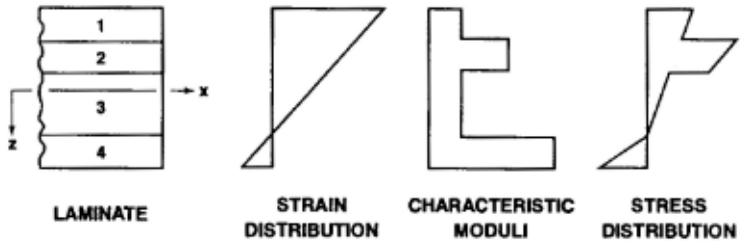

Source: Jones[4].

Failure criteria for laminated composites can be classified into three categories according to the level of interaction between stresses in different directions[39, 40]: Limiting or Non-interactive Criteria, as the Maximum Stress Criterion and the Maximum Strain Criterion, which are based on theories that consider stresses and strain individually for each direction; Interactive Criteria, such as Tsai-Hill, Tsai-Wu, and Hoffman Criteria, these are more elaborate theories that consider the interaction between directions, and finally there are Partially Interactive Criteria, such as the Puck Criterion, in which different failure modes for fibre and matrix are considered.

In this work, the Maximum Strain Criterion is employed. In this approach, the layer is said to fail if one of its strains $(\varepsilon_1, \varepsilon_2, \gamma_{12})$ exceeds the corresponding ultimate strain $(\varepsilon_1^u, \varepsilon_2^u, \gamma_{12}^u)$. The SF is taken as the minimum value obtained by computing the strains at the top and the bottom of each ply and relating it to to the respective ultimate strain as in:

$$SF_k = \min\left(\frac{\varepsilon_1^u}{\varepsilon_1^k}, \frac{\varepsilon_2^u}{\varepsilon_2^k}, \frac{\gamma_{12}^u}{\gamma_{12}^k}\right) \tag{2.6}$$

To define the failure of the laminate, the First-Ply Failure (FPF) approach is used. In this methodology, the laminate Safety Factor (SF) corresponds to the SF that satisfies all plies, that is:

$$SF^c = MIN_{k=1}^{N_p}(SF_k) \tag{2.7}$$

where N_p is the number of plies. This is a conservative approach, as the stress redistribution to the remaining plies is neglected. The methodology that considers the redistribution of stresses in

the laminate after the failure of the first ply is known as Progressive Failure. This process will likely lead to more accurate load capacity prediction, however, it is a far more complex approach as it requires the reduction of laminate stiffness as each ply fails.

2.2 Functionally Graded Materials

FGM are composite materials made of two or more phases with a continuous and smooth variation of the materials from one surface to another, as illustrated in Fig. 4 (a). This feature allows FGM to eliminate issues such as stress concentrations and provide superior thermo-mechanical performance [41].

Figure 4 – FG metal-ceramic

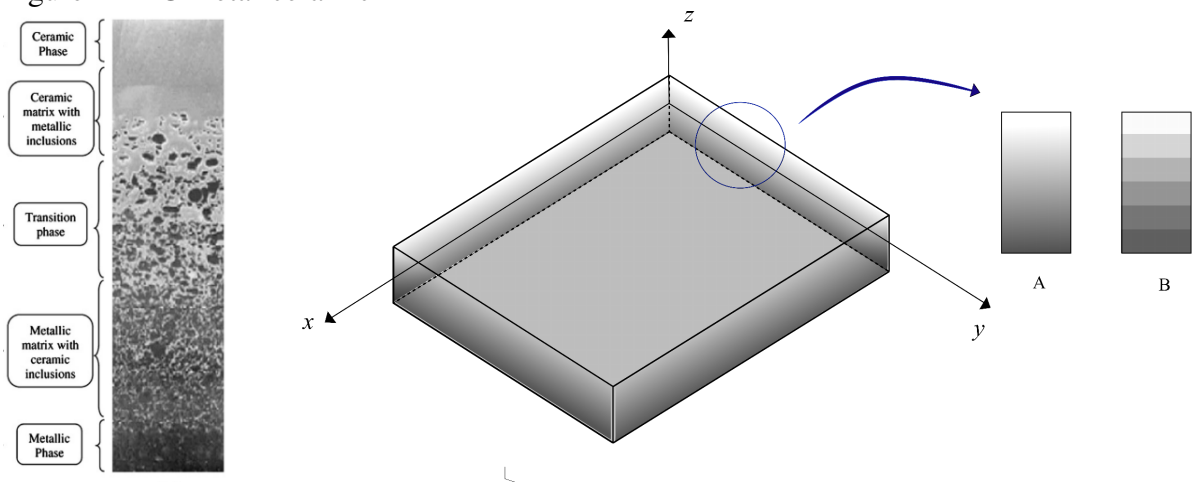

(a) Microstructure (b) Analytical models for a FG plate

Source: (a) Jha *et al.*[8], (b) the author

There are two basic approaches to model FGM. On the first choice, the volume fraction distribution is taken as continuous through one or more directions, as depicted by the cross-section A in Fig. 4 (b). In this work, unidirectional grading through the thickness is considered. On the second approach, the FG structure is taken as multilayered with the same volume fraction in each layer, as depicted by the cross-section B in Fig. 4 (b).

On the other hand, as a novel material, there are still a few gaps that need further investigation. Recently, Udupa *et al.*[42] listed the following topics: (i) lack of a proper database of gradient material, (ii) development of more robust models to predict the material behaviour and (iii) in practice, FGM demand not only higher manufacturing cost, but also more advanced manufacturing process.

The most popular combination is made of ceramic and metal. This way, the FGM

can benefit from the ductility and toughness of metals and the high strength and stiffness and low thermal conductivity properties of ceramics. Other types of mixtures such as ceramic-ceramic and ceramic-plastic are also found in the literature. Examples of metals include stainless steel, titanium, and aluminum oxide, whilst ceramic materials include zirconia and alumina [7].

2.2.1 Volume fraction distribution

To describe the variation of the material properties, a number of models have been proposed in the literature. The most commonly used are the Exponential function (E-FGM) [43], given by:

$$V_f = \exp\left(\ln\left(\frac{V_{f_b}}{V_{f_t}}\right)\left(\frac{2z+h}{2h}\right)^p\right) \tag{2.8}$$

the Power-law function (P-FGM) [44], given by:

$$V_f = \left(\frac{2z+h}{2h}\right)^p \tag{2.9}$$

and the Sigmoid function (S-FGM) [45], given by:

$$V_f = \begin{cases} 1 - \frac{1}{2}\left(\frac{h/2 - z}{h/2}\right)^p & \text{for } 0 \leq z \leq h/2, \\ \frac{1}{2}\left(\frac{h/2 - z}{h/2}\right)^p & \text{for } -h/2 \leq z \leq 0. \end{cases} \tag{2.10}$$

In Eq. (2.8) to Eq. (2.10), the volume fraction at the top ($z = +h/2$) is taken as 1.0 and at the bottom ($z = -h/2$) as 0.0, respectively, h is the total thickness of the shell and p is a non-homogeneity factor.

Alternatively, one may use experimental data of the volume fraction, if available, to fit a curve capable of capturing the jaggedness of the actual material composition [41]. In recent years, the use of B-splines has become a useful tool to model not only geometries through the Non-Uniform Rational B-Splines (NURBS), but also to describe the volume fraction distribution of FG structures. This is particularly useful in optimization problems [46, 47, 48, 49, 50] due to the high-order continuity of B-spline functions, which allows a continuous and smooth variation. Wang *et al.*[49] also draw attention to the fact that the use of B-splines can provide designs entirely different than those limited by certain mathematical functions. In addition, B-splines are always positive and thus, physical boundary constraints on interpolated volume fractions always lie in the range [0, 1] as expected.

Fig. 5 depicts the volume fraction distribution for the P-FGM, S-FGM and an example of a B-spline curve. Note how the S-FGM creates a smoother transition between the surfaces by using two P-FGMs. The curve on the right side illustrates how a B-spline curve may create a sandwich-like distribution if symmetric control points are imposed.

Figure 5 – Volume fraction distribution for different functions

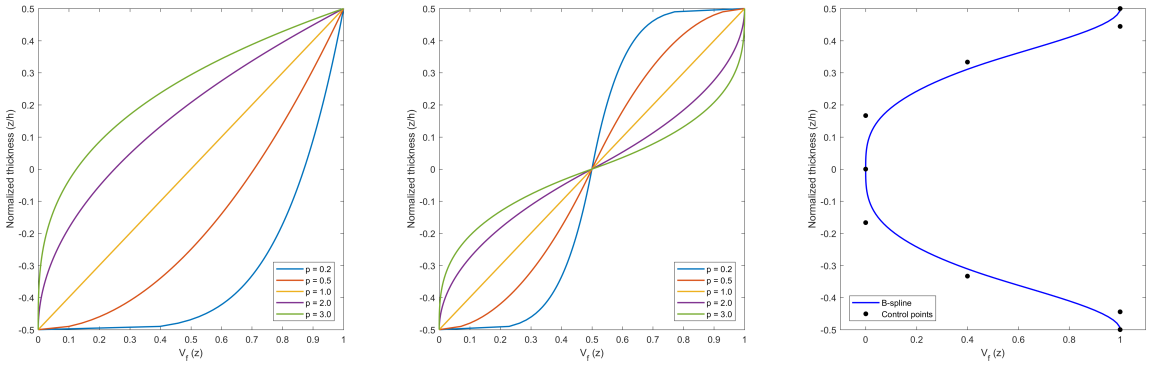

(a) P-FGM (b) S-FGM (c) B-spline

Source: the author.

2.2.2 *Effective properties*

Several micromechanics homogenization models have been developed over the years to infer the so-called effective properties of these materials based on the mechanical state of a material point on a macroscopic level [51]. This transition is known as *homogenization*. According to Pelletier and Vel[52], the most common methods for estimating the effective mechanical and thermal properties of FGM are the Rule of mixture (Voigt model) and the Mori-Tanaka Model. These are the homogenization schemes adopted in the numerical examples explored in this work and will be briefly discussed in the following.

In any case, an accurate model must include temperature and position dependence. For that matter, one may use Toulokian's equation [53]:

$$P(T) = P_0 \left(\frac{P_{-1}}{T} + 1 + P_1 T + P_2 T^2 + P_3 T^3 \right) \tag{2.11}$$

where P_i are the unique coefficients of each of the constituents for the temperature T (in Kelvin).

Shen and Wang[54] compared these two models for the vibration analysis of FG plates and suggested that the difference between them in the estimation of the global response is negligible, and recommended the use of the Rule of Mixture over the Mori-Tanaka model due to its simplicity. Conversely, on a study on FG pressurized cylinders considering different

homogenization schemes and volume distribution models, Medeiros JR. *et al.*[41] show that, despite its large popularity, the Voigt model provides large discrepancies with more sophisticated and accurate models. Among the homogenization schemes considered, the authors conclude that the Mori-Tanaka and the Generalized Self-Consistent yielded the best results.

Given the effective properties, the constitutive relation is analogous to that presented in Eq. (2.1). Note that the FGM are considered isotropic in the *x*-*y* plane, varying their properties along the *z* direction. Thus, the terms of the matrices $\mathbf{Q}$ and $\mathbf{Q_s}$ are simplified to:

$$Q_{11} = Q_{22} = \frac{E(z)}{1-\nu^2(z)} \qquad Q_{12} = \frac{E(z)\ \nu(z)}{1-\nu^2(z)} \qquad Q_{44} = Q_{55} = Q_{66} = \frac{E(z)}{2(1+\nu(z))} \tag{2.12}$$

When it comes to the failure criteria for FG structures, the von Mises yield criterion is a popular choice used to estimate the effective stress in optimization problems [52, 55, 56, 14, 57]. In this approach, the effective stress (σ_{vm}) of a isotropic material may be evaluated by:

$$\sigma_{vm} = \sqrt{\sigma_1^2 + \sigma_2^2 - \sigma_1\sigma_2 + 3\tau_{12}^2 + 3\tau_{13}^2 + 3\tau_{23}^2} \tag{2.13}$$

For FG structures, the effective stress has to be evaluated in multiple points through the grading direction and in all of them, the result of Eq. (2.13) cannot exceed the homogenized yield strength (σ_y). Thus, to obtain a SF, we simply divide the yield stress (σ_y) by the von Mises stress as in:

$$SF = \frac{\sigma_y}{\sigma_{vm}} \tag{2.14}$$

where σ_y may be estimated by the model proposed by Tamura[58]. For applications involving ceramic/metal composites, this model assumes that the composite yields once the metal constituent yields and introduces the parameter q to represent the ratio of stress to strain transfer. To properly estimate q, a significant number of experiments need to be carried out. In the literature, few combinations of materials were explored [59, 58]. After this definition, the Tamura–Tomota–Ozawa (TTO) model calculates the yield stress of the composite as:

$$\sigma_y = \sigma_{y_m}(V_m + \frac{q+E_m}{q+E_c}\frac{E_c}{E_m}V_c) \tag{2.15}$$

where E_m, E_c, V_m and V_c are the Young Modulus and the volume fraction of the metallic and ceramic phases, respectively, and σ_{y_m} is the yield stress of the metallic phase. For metal-metal FGM, σ_y may be simply evaluated following the linear Rule of Mixture [60].

2.2.2.1 Voigt Model

The Voigt model, commonly known as Rule of Mixture, is the simplest model used in most analyses of FG structures. It consists in a weighted average of the properties of the constituents, where each of them contributes with its volume fraction. This way, the elastic properties of the material at a given point along the thickness can be evaluated as [7]:

$$P_f = \sum_{j=1}^{N_c} P_j V_{f_j} \tag{2.16}$$

where P_f are the effective properties of the material and P_j and V_{f_j} are the properties and volume fraction of the j-th constituent and N_c is the number of constituents. The volume fraction represents the relative quantitative of each of the constituents in comparison to the volume of the whole system [7]. Therefore, $\sum_{j=1}^{N_c} V_{f_j} = 1$.

Considering the ceramic-metal example, the estimate of the Young's modulus would be calculated by:

$$E(z) = (E_m - E_c)\, V_m(z) + E_c \tag{2.17}$$

where m and c stand for metal and ceramic, respectively. Since the volume fraction represents the relative amount of material of one of the constituents in relation to the total amount of the system, we have:

$$V_c + V_m = 1 \tag{2.18}$$

2.2.2.2 Mori-Tanaka's Model

In case of composites with spherical inclusions embedded in a matrix, the Mori-Tanaka model evaluates the effective bulk modulus (K) and effective shear modulus (G) as follows:

$$\begin{aligned} K &= K_m + \frac{V_c}{\dfrac{1}{K_c - K_m} + \dfrac{V_m}{K_m + \dfrac{4G_m}{3}}} \\ G &= G_m + \frac{V_c}{\dfrac{1}{G_c - G_m} + \dfrac{V_m}{G_m + f_m}} \end{aligned} \tag{2.19}$$

where the parameter f_m is given by:

$$f_m = \frac{G_m(9K_m + 8G_m)}{6(K_m + 2G_m)} \tag{2.20}$$

After that, the effective Young's modulus (E) and Poisson's ratio (ν) are computed from:

$$E = \frac{9KG}{3K+G} \qquad \nu = \frac{3K-2G}{2(3K+G)} \tag{2.21}$$

Typically, the effective density (ρ) is estimated by the Voigt model even when the Mori-Tanaka is used to estimate the other elastic properties.

3 STRUCTURAL ANALYSIS

This chapter presents the structural analysis adopted in this work, including the kinematic formulation, the internal forces evaluation, and a brief review on the IGA formulation used.

3.1 Plates and shallow shells

The kinematic formulation of this work is based on the Reissner-Mindlin Theory, in which the plate cross sections remain plane after deformation, but not necessarily normal to the reference plane. This results in the consideration of an approximate transverse shear strain in the theory [5]. Thus, the displacements can be written in matrix form as:

$$\begin{bmatrix} \overline{u} \\ \overline{v} \\ \overline{w} \end{bmatrix} = \begin{bmatrix} 1 & 0 & 0 & 0 & z \\ 0 & 1 & 0 & -z & 0 \\ 0 & 0 & 1 & 0 & 0 \end{bmatrix} \begin{bmatrix} u \\ v \\ w \\ \theta_x \\ \theta_y \end{bmatrix} \Rightarrow \overline{\mathbf{u}} = \mathbf{Z}\,\mathbf{u} \tag{3.1}$$

where u, v and w are the midsurface displacements in the x, y and z directions; θ_x and θ_y are the rotations about x and y axes, respectively; z is the distance from a point to the midsurface.

Based on the displacement field presented in Eq. (3.1) and on the Marguerre theory, the in-plane strains are given by:

$$\boldsymbol{\varepsilon} = \begin{Bmatrix} \varepsilon_x \\ \varepsilon_y \\ \gamma_{xy} \end{Bmatrix} = \boldsymbol{\varepsilon}^m + z\boldsymbol{\kappa} \tag{3.2}$$

where m refers to the membrane strains and $\boldsymbol{\kappa}$ corresponds to the shell curvatures. The Marguerre theory extends the nonlinear plate theory of von Kármán for shallow shells [61]. In fact, the Marguerre membrane strains reduces to the von Kármán strains for an initially flat plate ($z_0 = 0$). Due to the consideration of moderately large displacements, it also allows the study on the stability of plates and shallow shells, including initial imperfections:

$$\boldsymbol{\varepsilon}^m = \begin{Bmatrix} \varepsilon_x^m \\ \varepsilon_y^m \\ \gamma_{xy}^m \end{Bmatrix} = \begin{Bmatrix} u_{,x} \\ v_{,y} \\ u_{,y} + v_{,x} \end{Bmatrix} + \begin{Bmatrix} w_{z,x}\, z_{0,x} \\ w_{z,y}\, z_{0,y} \\ w_{,x}\, z_{0,y} + w_{,y}\, z_{0,x} \end{Bmatrix} + \begin{Bmatrix} \frac{1}{2} {w_{,x}}^2 \\ \frac{1}{2} {w_{,y}}^2 \\ w_{,x}\, w_{,y} \end{Bmatrix} \tag{3.3}$$

where $z_0(x,y)$ is the initial midplane surface elevation. The deformation due to the bending are described by:

$$\begin{Bmatrix} \kappa_x \\ \kappa_y \\ \kappa_{xy} \end{Bmatrix} = \begin{Bmatrix} \theta_{y,x} \\ -\theta_{x,y} \\ \theta_{y,y} - \theta_{x,x} \end{Bmatrix} \tag{3.4}$$

The transverse shear strains are given by:

$$\gamma = \begin{Bmatrix} \gamma_{xz} \\ \gamma_{yz} \end{Bmatrix} = \begin{Bmatrix} w_{,x} + \theta_y \\ w_{,y} - \theta_x \end{Bmatrix} \tag{3.5}$$

Note that the shear strains are constant throughout the thickness of the shell, which is not consistent to the Elasticity Theory solution, in which the shear variation is parabolic. Thus, to adjust the transverse shear stiffness taken as constant through the thickness closer to the parabolic shear-stress distribution, the shear effects obtained by this theory are multiplied by a factor, say k_s, known as shear correction factor. As a result, the accuracy of the FSDT predictions depend significantly on the this factor. Usually, k_s is taken as $5/6$, as derived by Reissner[62] for homogeneous plates, which is also adopted in this work. However, it is worth mentioning that many authors [63, 64, 65] argued that this simplification for multilayered plates may imply in significant errors especially when the moduli ratio E_1/E_2 is large (e.g. $E_1/E_2 \approx 15$). This behaviour is also observed in FG structures when the moduli ratio between the constituents is large.

3.2 Internal forces

Due to the differences in the nature of each of the materials, the resultant forces and moments will be described in different sections. For laminated composites, each layer is treated as homogeneous and orthotropic, while FGM are considered as inhomogeneous and isotropic with varying properties through the thickness.

3.2.1 Laminated composites

The forces and moments can be obtained by integrating the stresses, given by Eq. (2.5), over the structure thickness h as in:

$$\begin{aligned}
\mathbf{N} &= \begin{Bmatrix} N_x \\ N_y \\ N_{xy} \end{Bmatrix} = \int_{-h/2}^{h/2} \begin{Bmatrix} \sigma_x \\ \sigma_y \\ \sigma_{xy} \end{Bmatrix} dz = \sum_{k=1}^{n_p} \int_{k-1}^{k} \overline{\mathbf{Q}}^k \boldsymbol{\varepsilon}^k dz \\
\mathbf{M} &= \begin{Bmatrix} M_x \\ M_y \\ M_{xy} \end{Bmatrix} = \int_{-h/2}^{h/2} \begin{Bmatrix} \sigma_x \\ \sigma_y \\ \sigma_{xy} \end{Bmatrix} z\, dz = \sum_{k=1}^{n_p} \int_{k-1}^{k} \overline{\mathbf{Q}}^k \boldsymbol{\varepsilon}^k z\, dz \\
\mathbf{Q} &= \begin{Bmatrix} Q_{xz} \\ Q_{yz} \end{Bmatrix} = \int_{-h/2}^{h/2} \begin{Bmatrix} \tau_{xz} \\ \tau_{yz} \end{Bmatrix} dz = k_s \sum_{k=1}^{n_p} \int_{k-1}^{k} \overline{\mathbf{Q}_\mathbf{s}}^k \boldsymbol{\gamma}^k dz
\end{aligned} \tag{3.6}$$

where k refers to the k-th ply

In terms of membrane strains, curvatures and shear strains, Eq. (3.6) may be rewritten in compact form as [5]:

$$\begin{Bmatrix} \mathbf{N} \\ \mathbf{M} \\ \mathbf{Q} \end{Bmatrix} = \begin{bmatrix} \mathbf{A} & \mathbf{B} & \mathbf{0} \\ \mathbf{B} & \mathbf{D} & \mathbf{0} \\ \mathbf{0} & \mathbf{0} & \mathbf{G} \end{bmatrix} \begin{Bmatrix} \varepsilon_m \\ \kappa \\ \gamma \end{Bmatrix} \tag{3.7}$$

where **A** is the membrane stiffness matrix, **D** is the bending stiffness, **B** is the membrane-bending coupling matrix, **G** is the transverse shear stiffness matrix, ε_m is the membrane strains vector and κ is the vector of curvatures. Note that the membrane and bending are coupled due to the **B** matrix, but the shear terms are uncoupled. For a symmetric laminate, there is no coupling between membrane and bending responses (i.e. $\mathbf{B} = \mathbf{0}$). The components of these matrices can be obtained by numerical or analytical integration. Summing up the contribution of each lamina, one obtain:

$$\begin{aligned}
A_{ij} &= \sum_{k=1}^{n_p} \overline{Q}_{ij}^k (z_k - z_{k-1}) \qquad & B_{ij} &= \sum_{k=1}^{n_p} \frac{\overline{Q}_{ij}^k (z_k^2 - z_{k-1}^2)}{2} \\
D_{ij} &= \sum_{k=1}^{n_p} \frac{\overline{Q}_{ij}^k (z_k^3 - z_{k-1}^3)}{3} \qquad & G_{ij} &= k_s \sum_{k=1}^{n_p} \overline{Q}_{ij}^k (z_k - z_{k-1})
\end{aligned} \tag{3.8}$$

where $i, j = 4, 5$ for the **G** matrix and $i, j = 1, 2, 3$ for all other matrices.

3.2.2 Functionally Graded Materials

Similarly, the internal forces and moments can be obtained for FGM as:

$$\begin{aligned}
\mathbf{N} &= \begin{Bmatrix} N_x \\ N_y \\ N_{xy} \end{Bmatrix} = \int_{-h/2}^{h/2} \begin{Bmatrix} \sigma_x \\ \sigma_y \\ \sigma_{xy} \end{Bmatrix} dz = \int_{-h/2}^{h/2} \mathbf{Q}(z)\ \varepsilon\ dz \\
\mathbf{M} &= \begin{Bmatrix} M_x \\ M_y \\ M_{xy} \end{Bmatrix} = \int_{-h/2}^{h/2} \begin{Bmatrix} \sigma_x \\ \sigma_y \\ \sigma_{xy} \end{Bmatrix} (z)\ z\ dz = \int_{-h/2}^{h/2} \mathbf{Q}\ \varepsilon z\ dz \\
\mathbf{Q} &= \begin{Bmatrix} Q_{xz} \\ Q_{yz} \end{Bmatrix} = \int_{-h/2}^{h/2} \begin{Bmatrix} \tau_{xz} \\ \tau_{yz} \end{Bmatrix} dz = k_s \int_{-h/2}^{h/2} \mathbf{Q}_s(z)\ \gamma\ dz
\end{aligned} \tag{3.9}$$

Note that there is no need for transforming the constitutive matrices $\mathbf{Q}$ and $\mathbf{Q}_s$ as we deal with a isotropic material. However, its properties should be evaluated and integrated through the thickness along which its properties vary. Thus, the **ABDG** matrices are given by:

$$\begin{aligned}
\mathbf{A} &= \int_{-h/2}^{h/2} \mathbf{Q}(z) dz \qquad & \mathbf{B} &= \int_{-h/2}^{h/2} \mathbf{Q}(z)\ z\ dz \\
\mathbf{D} &= \int_{-h/2}^{h/2} \mathbf{Q}(z)\ z^2\ dz \qquad & \mathbf{G} &= k_s \int_{-h/2}^{h/2} \mathbf{Q}_s(z)\ dz
\end{aligned} \tag{3.10}$$

The same remark made for laminates is valid. Symmetrical volume fraction distributions lead to $\mathbf{B} = 0$. If this is not case, the membrane-bending coupling may have significant impact on the stability behaviour of the structure.

3.3 Isogeometric Analysis

The concept of the Isogeometric Analysis (IGA) was first proposed by Hughes *et al.*[66] as a way to match the exact Computer-Aided Design (CAD) geometry by NURBS surfaces. In this framework, the CAD spline functions are also used to approximate unknown fields in FEA. This results in numerous advantages for all kinds of structures, but may particularly benefit the analysis of structures extremely sensitive to geometric imperfections such as thin shells and structures with complex geometries. Also, the IGA provides a much simpler mesh refinement and exact representation even for coarse meshes.

Recently, IGA has been used in association with various plate theories for composite plates analysis, such as Higher-Order Shear Deformation Theory (HSDT) [47, 67, 48], FSDT

[68, 69, 49] and Classical Plate Theory (CPT) [70]. In this work, the IGA framework is used with the FSDT. The initial isogeometric framework implemented on Finite element AnalyiS Tool (FAST) was developed by Barroso[70] using solid elements. Later on, Praciano *et al.*[68] implemented the isoparametric shell element used in this work. Finally, Auad[71] added an isoparametric element focused on the analysis of FG cylindrical shells based on Donnell's nonlinear theory.

3.3.1 B-Splines and NURBS

A B-Spline curve is defined by the linear combination of control points $\mathbf{p}_i$ and basis functions $B_{i,p}$ as in:

$$C(\xi) = \sum_{i=1}^{n} B_{i,p}(\xi)\mathbf{p}_i \tag{3.11}$$

where n is the number of basis functions, p is the degree of the basis functions and ξ is the parametric coordinate. This curve may be completely changed depending on the spatial distribution of the parametric coordinates and on the position of the control points.

A knot span is defined by a vector of non-decreasing and non-negative parametric values called *knot vector*. Based on a knot vector $\Xi = [\xi_1, \xi_2, \ldots, \xi_{n+p+1}]$ considering the parametric interval in the range $[0,1]$, the B-Spline basis functions are defined by the recursive Cox-de Boor formula as [72]:

$$\begin{aligned} B_{i,0}(\xi) &= \begin{cases} 1, \xi_i \leq \xi < \xi_{i+1} \\ 0, \text{otherwise} \end{cases} \\ B_{i,p}(\xi) &= \frac{\xi - \xi_i}{\xi_{i+p} - \xi_i} B_{i,p-1}(\xi) + \frac{\xi_{i+p+1} - \xi}{\xi_{i+n+1} - \xi_{i+1}} B_{i+1,p-1}(\xi) \end{aligned} \tag{3.12}$$

where $p \geq 1$. Each basis function $B_{i,p}$ contributes in the parametric interval $[\xi_i, \xi_{i+p+1}]$, but only $p+1$ basis are non-zero in each knot span. This property is known as compact support.

Moreover, if a knot value is repeated in the knot vector, the number of times that this occurs is known as knot *multiplicity*. This is important due to the effect on the continuity inside the knot span. If a knot has multiplicity m, then the curve is only C^{p-m} continuous at that parametric coordinate and not C^{p-1} continuous as inside the knot span.

If the knots are equally spaced in the parametric space, they are said to be *uniform*. Otherwise, they are *non-uniform*. Conventionally, IGA uses open knot vectors, that is, vectors in which the first and the last parametric values have multiplicity $m = p+1$, which makes these points to be interpolated. The number of control points (n_{cp}) corresponds to the number of

B-Spline basis functions and should be calculated as:

$$n_{cp} = n_k - p - 1 \tag{3.13}$$

where n_k is the size of the knots vector. Several other important properties are observed in B-Splines functions, such as:

1. Partition of unit $\sum_{i=1}^{n} B_{i,p}(\xi) = 1$;
2. As a consequence of the compact support, for a given knot span, $p+1$ basis functions are zero in this interval;
3. All derivatives of $B_{i,p}$ exist inside the knot spans. At the knots, the basis are only $m-p$ differentiable.

B-Splines allow three types of refinement: (1) the order elevation, which corresponds to the p-refinement in FEA, (2) knot insertion, which corresponds to the h-refinement, and (3) the k-refinement, which has no analogue in FEA. When elevating the order of a knot vector Ξ, the geometry curve may remain unchanged by the increase in the multiplicity of unique knots in Ξ. This process is illustrated in Fig. 6 (a) and (b), in which a quadratic curve was elevated to a cubic one.

Figure 6 – B-Spline basis functions

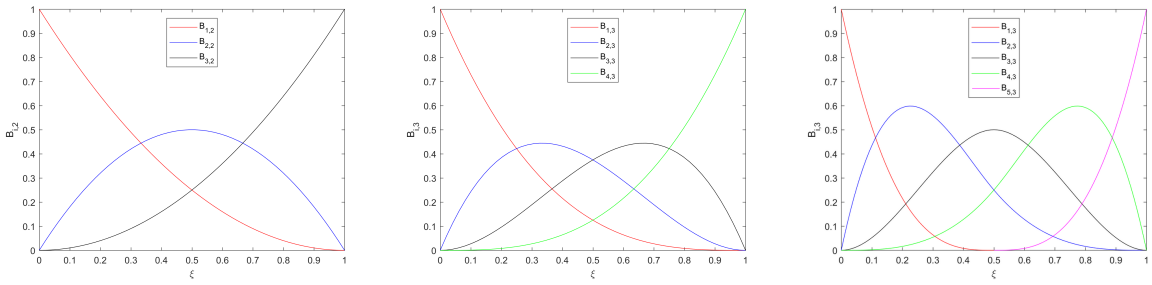

(a) $\Xi = [0,0,0,1,1,1]$ (b) $\Xi = [0,0,0,0,1,1,1,1]$ (c) $\Xi = [0,0,0,0,0.5,1,1,1,1]$

Source: the author.

In the knot insertion, a new knot ξ_i is inserted in the knot vector Ξ creating a new basis function and, as a consequence, a new control point without changing the geometry curve. This process increases the number of knot spans (n_s), as shown in Fig. 6 (a), in which $n_s = 1$, and Fig. 6 (c), where $n_s = 2$, while keeping $p = 2$. Finally, in the k-refinement, both the order elevation and knot insertion are carried out.

In addition to modeling the structure using NURBS, which heavily rely on the B-Splines concepts, this type of curve has also been gaining attention in the FG definition of volume fraction distributions. Fig. 7 illustrates different curves ($p = 3$) with the same open

Figure 7 – Variation on the control point $\mathbf{p}_2$ for $\Xi = [0.0, 0.0, 0.0, 0.0, 0.5, 1.0, 1.0, 1.0, 1.0]$

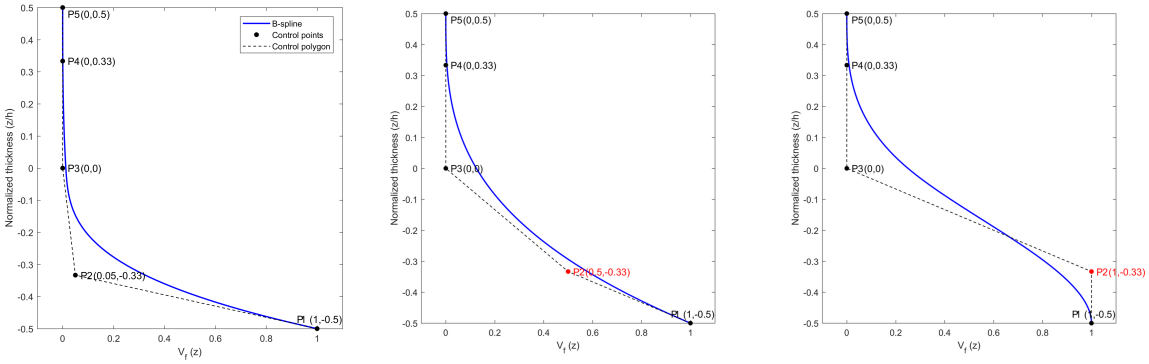

Source: the author.

knot vector by changing the position of one control point. Note how the curve goes from a sharp transition between the materials in (a) to a smooth transition that resembles a Power-Law function in (b), or a Sigmoid function in (c).

Despite its flexibility, B-Splines cannot exactly represent conical sections such as circles and ellipses due to the non-polynomial character of these surfaces. To overcome this shortcoming, NURBS are used. Interested readers on the mathematical background are referred to the work of Piegl and Tiller[72] and Hughes *et al.*[66].

3.3.2 NURBS

NURBS are widely used in geometric modeling since they offer a mathematical description capable to represent both analytic (e.g. circles and ellipses) and free-form curves and surfaces using the same database. A tensor product NURBS surface (S) of degree ($p \times q$) is defined by a linear combination of bivariate rational basis functions (R) and a matrix of control points ($\mathbf{p}$):

$$S(\xi,\eta) = \sum_{i=1}^{n}\sum_{j=1}^{m} R_{ij}(\xi,\eta)\,\mathbf{p}_{ij} \tag{3.14}$$

where ξ and η are the parametric coordinates. The rational basis functions R are evaluated based on a set of weights w_{ij} associated to each control point and B-Spline basis functions B defined for each parametric variable:

$$R_{ij}(\xi,\eta) = \frac{B_{i,p}(\xi)\,B_{j,q}(\eta)\,w_{ij}}{W(\xi,\eta)} \tag{3.15}$$

where W is the bivariate weight function expressed by:

$$W(\xi,\eta) = \sum_{\hat{i}=1}^{n}\sum_{\hat{j}=1}^{m} B_{\hat{i},p}(\xi)\,B_{\hat{j},q}(\eta)\,w_{\hat{i}\hat{j}} \tag{3.16}$$

3.3.2.1 Displacements and Strains

In the isogeometric formulation used in this work, the shell geometry is described by a bivariate NURBS:

$$x = \sum_{k=1}^{n_{cp}} R_k x_k, \quad y = \sum_{k=1}^{n_{cp}} R_k y_k \quad z = \sum_{k=1}^{n_{cp}} R_k z_k \tag{3.17}$$

where R_k are the functions defined by Equation (3.15) and n_{cp} is the number of control points of the surface. The in-plane and transverse displacements and rotations at the plate mid-surface are approximated from the element degrees of freedom at control points as:

$$\begin{aligned} u &= \sum_{k=1}^{n_{cp}} R_k u_k, \quad v = \sum_{k=1}^{n_{cp}} R_k v_k, \quad w = \sum_{k=1}^{n_{cp}} R_k w_k \\ \theta_x &= \sum_{k=1}^{n_{cp}} R_k \theta_{xk}, \quad \theta_y = \sum_{k=1}^{n_{cp}} R_k \theta_{yk} \end{aligned} \tag{3.18}$$

In matrix format, Eq. (3.18) may be written as:

$$\mathbf{u} = \mathbf{R}\,\mathbf{d} \tag{3.19}$$

where $\mathbf{d}$ is the vector of degrees of freedom, corresponding to the displacements at control points, and $\mathbf{R}$ is the matrix of shape functions:

$$\mathbf{R} = \begin{bmatrix} \mathbf{R}_1 & \mathbf{R}_2 & \dots & \mathbf{R}_{n_{cp}} \end{bmatrix} \tag{3.20}$$

where:

$$\mathbf{R}_k = R_k\,\mathbf{I}_{5x5} \tag{3.21}$$

where $\mathbf{I}$ is the identity matrix. The generalized strains are related to the degrees of freedom:

$$\hat{\varepsilon} = \begin{bmatrix} \varepsilon_0^m + \varepsilon_L^m \\ \kappa \\ \gamma \end{bmatrix} = \begin{bmatrix} \mathbf{B}_0^m \\ \mathbf{B}_0^b \\ \mathbf{B}_0^s \end{bmatrix} \mathbf{d} + \frac{1}{2} \begin{bmatrix} \mathbf{B}_L^m \\ 0 \\ 0 \end{bmatrix} \mathbf{d} = \left(\mathbf{B}_0 + \frac{1}{2}\mathbf{B}_L \right) \mathbf{d} \tag{3.22}$$

Using Eq. (3.3)-(3.5) and (3.18)-(3.21), the sub-matrices are defined by:

$$\mathbf{B}_0^m = \begin{bmatrix} R_{k,x} & 0 & Z_x R_{k,x} & 0 & 0 \\ 0 & R_{k,y} & Z_y R_{k,y} & 0 & 0 \\ R_{k,y} & R_{k,x} & Z_x R_{k,y} + Z_y R_{k,x} & 0 & 0 \end{bmatrix}$$

$$\mathbf{B}_0^b = \begin{bmatrix} 0 & 0 & 0 & 0 & R_{k,x} \\ 0 & 0 & 0 & -R_{k,y} & 0 \\ 0 & 0 & 0 & -R_{k,x} & R_{k,y} \end{bmatrix} \tag{3.23}$$

$$\mathbf{B}_0^s = \begin{bmatrix} 0 & 0 & R_{k,x} & 0 & R_k \\ 0 & 0 & R_{k,y} & -R_k & 0 \end{bmatrix}$$

$$\mathbf{B}_L^m = \begin{bmatrix} 0 & 0 & W_x R_{k,x} & 0 & 0 \\ 0 & 0 & W_y R_{k,y} & 0 & 0 \\ 0 & 0 & W_x R_{k,y} + W_y R_{k,x} & 0 & 0 \end{bmatrix}$$

where:

$$\begin{aligned} Z_x &= \sum_{k=1}^{n_{cp}} R_{k,x} z_{0k}, & Z_y &= \sum_{k=1}^{n_{cp}} R_{k,y} z_{0k}, \\ W_x &= \sum_{k=1}^{n_{cp}} R_{k,x} w_k, & W_y &= \sum_{k=1}^{n_{cp}} R_{k,y} w_k \end{aligned} \tag{3.24}$$

3.3.2.2 Equilibrium Equations

The dynamic equilibrium equations of the model can be obtained using the D'Alembert and Virtual Work principles according to:

$$\int_A \delta \mathbf{u}^T \overline{\mathbf{M}} \ddot{\mathbf{u}} \, dA + \int_A \delta \hat{\varepsilon}^T \hat{\sigma} \, dA = \int_A \delta \mathbf{u}^T \mathbf{q} \, dA + \int_S \delta \mathbf{u}^T \mathbf{f}_s \, dS \tag{3.25}$$

where $\mathbf{q}$ is the surface load, $\mathbf{f}_s$ is the boundary load, A and S are the midsurface area and midsurface boundary of the plate, respectively and $\overline{\mathbf{M}}$ is given by:

$$\overline{\mathbf{M}} = \int_{-h/2}^{h/2} \rho \, \mathbf{Z}^T \mathbf{Z} \, dz = \begin{bmatrix} I_0 & 0 & 0 & 0 & I_1 \\ 0 & I_0 & 0 & -I_1 & 0 \\ 0 & 0 & I_0 & 0 & 0 \\ 0 & -I_1 & 0 & I_2 & 0 \\ I_1 & 0 & 0 & 0 & I_2 \end{bmatrix} \tag{3.26}$$

and

$$[I_0, I_1, I_2] = \int_{-h/2}^{h/2} \rho(z)[1, z, z^2] \, dz \tag{3.27}$$

Substituting Equation (3.18) in Equation (3.25) and considering arbitrary virtual displacements, the dynamic equilibrium equation at a time t can be written as:

$$\mathbf{M}\ddot{\mathbf{d}} + \mathbf{g}(\mathbf{d}) = \mathbf{f}(t) \tag{3.28}$$

where:

$$\mathbf{M} = \int_A \mathbf{R}^T \overline{\mathbf{M}} \mathbf{R}\, dA \tag{3.29}$$

$$\mathbf{f} = \int_A \mathbf{R}^T \mathbf{q}\, dA + \int_S \mathbf{R}^T \mathbf{f}_s\, dS \tag{3.30}$$

$$\mathbf{g} = \int_A \overline{\mathbf{B}}^T \hat{\boldsymbol{\sigma}}\, dA \tag{3.31}$$

$\mathbf{M}$ is the mass matrix and $\overline{\mathbf{B}} = \mathbf{B}_0 + \mathbf{B}_L$ is the matrix that relates the variation of the generalized strains with the variation of the control points displacements ($\delta\hat{\boldsymbol{\varepsilon}} = \overline{\mathbf{B}}\,\delta\mathbf{d}$).

In this work, $\overline{\mathbf{M}}$ is evaluated using the Gaussian quadrature to carry-out the through-the-thickness integration just as the constitutive matrix. For each trial design of the optimization process, both matrices are written in the input file used for the analysis and processed on FAST.

Finally, by differentiating the internal force vector ($\mathbf{g}$), the tangent stiffness matrix is obtained:

$$\mathbf{K}_T = \frac{\partial \mathbf{g}}{\partial \mathbf{d}} = \mathbf{K}_L + \mathbf{K}_\sigma \tag{3.32}$$

where the material stiffness matrix $\mathbf{K}_L$ and the geometric stiffness matrix $\mathbf{K}_\sigma$ are given by:

$$\mathbf{K}_L = \int_A \overline{\mathbf{B}}^T \frac{\partial \hat{\boldsymbol{\sigma}}}{\partial \mathbf{d}}\, dA = \int_A \overline{\mathbf{B}}^T \mathbf{C}\, \overline{\mathbf{B}}\, dA \tag{3.33}$$

$$\mathbf{K}_\sigma = \int_A \frac{\partial \overline{\mathbf{B}}^T}{\partial \mathbf{d}}\, \boldsymbol{\sigma}\, dA = \int_A \mathbf{G}^T \mathbf{S}\, \mathbf{G}\, dA \tag{3.34}$$

where $\mathbf{C}$ is the constitutive matrix and $\mathbf{G}$ and $\mathbf{S}$ are given by:

$$\mathbf{G} = \begin{bmatrix} 0 & 0 & R_{k,x} & 0 & 0 \\ 0 & 0 & R_{k,y} & 0 & 0 \end{bmatrix}, \quad \mathbf{S} = \begin{bmatrix} N_x & N_{xy} \\ N_{xy} & N_y \end{bmatrix} \tag{3.35}$$

Despite the simplicity and satisfactory results, the linear analysis is limited by several aspects in structural analysis such as the linearity of the material, by the geometry of the structure and due to contact problems [73]. In this work, only the second type of non-linearity is addressed, allowed by the use of the Marguerre theory for nonlinear membrane strains, as shown in Eq. (3.2). This type of analysis is often required when dealing with structures nearing collapse or when the linear behaviour is not a good predictor. This is the case when structures undergo large deformations or when plasticity and creep are considered, for example.

However, the non-linear analysis is a much more complex and computationally expensive process, which may be a bottleneck to its widespread use in association with population-based algorithms. In this work, the numerical examples explore both problems where the linear analysis is adequate and can be safely employed to the optimization of composite structures and problems where the consideration of the geometric nonlinearity is of paramount importance. In this case, the equilibrium of the system for displacement-independent loads are given by:

$$\mathbf{r}(\mathbf{u},\lambda) = \mathbf{g}(\mathbf{u}) - \lambda\mathbf{q} \tag{3.36}$$

where $\mathbf{r}$ is the residual vector, $\mathbf{u}$ is the vector of degrees of freedom, λ is the load factor which controls the load application on the structure ($\mathbf{f} = \lambda\mathbf{q}$), $\mathbf{q}$ is the vector of external reference loads. This equation is usually solved using a path-following method, such as the Load Control Method, Displacement Control Method and the Arch-Length Method. The detailed methodology implemented on FAST and used in this work is found in Praciano *et al.*[68]. These incremental-iterative algorithms are usually based on Newton-Raphson iterations.

3.3.3 Eigenvalue problems

The free vibration analysis is carried-out solving the generalized eigenproblem :

$$(\mathbf{K} - \omega^2\mathbf{M})\,\phi = \mathbf{0} \tag{3.37}$$

where $\mathbf{K}$ is the stiffness matrix of the unloaded structure ($\mathbf{d} = \mathbf{0}$), ω are the natural frequencies, and ϕ are the vibration modes.

For structures with negligible pre-buckling displacements, stability analysis can be carried out in the same form as a vibration problem, but replacing the mass matrix by the geometric stiffness matrix due to the reference loads ($\mathbf{K}_\sigma$) as in:

$$(\mathbf{K} + \lambda\,\mathbf{K}_\sigma)\,\phi = \mathbf{0} \tag{3.38}$$

where λ are the buckling load factors and ϕ are the buckling modes. It should be emphasized that this procedure is appropriate only if there is little or no coupling between membrane and bending deformations [73]. This is important to understand why the buckling of simply supported plates with non-symmetrical volume fraction distributions cannot be treated as a eigenvalue problem, as discussed by Praciano *et al.*[68] and Auad *et al.*[69].

4 OPTIMIZATION OF COMPOSITE STRUCTURES

Over the past decades, optimization techniques have been extensively used in structural design problems. This way, over-designed structures, and consequent profit loss can be avoided by the adequate formulation of the optimization problem and by the correct choice of the optimization technique. For that matter, it is highly important that when composite materials are employed in the manufacturing of these structures, the mechanical behaviour of the material itself is properly addressed.

Therefore, the fruitful use of composite structures depends not only on geometry constraints but also on the accurate definition of the material properties and its structural behaviour so that their potential can be fully explored. The typical choices of design variables in laminated composite optimization problems are the fibre orientation, material, and thickness of each ply [13]. For example, if one decided to go for hand calculations or simply run an exhaustive search algorithm in a two-dimensional laminated composite problem considering only three possible fibre orientation angles and two possible values for the thickness considering 10 plies, it would take over 60 million evaluations to cover the entire design space. This type of search is computationally prohibitive unless the HF analysis is extremely cheap, which is hardly the case of structural engineering problems. This combinatorial problem belongs to a class of challenging real-world optimization problems known as NP-hard [74].

Thus, due to the impracticality of exhaustive search, many meta-heuristics were developed and are now widely used to solve this kind of problem. These algorithms are also used when the use of gradient-based methods would result in time-consuming sensitivity analyses [75, 76].

On a side note, it is worth mentioning that despite the lack of mathematical guarantee that the best solution found is indeed optimal, this type of algorithm is vastly used to solve laminated composite and FGM problems due to their simplicity and robustness. As a matter of fact, Lagaros *et al.*[77] showed in a comparison between heuristics algorithms such as GAs and Evolutionary Strategies (ES) and classical mathematical programming algorithms such as Sequential Quadratic Programming (SQP) that heuristics algorithms are capable of providing better quality solutions than classic algorithms at a lower computational cost.

The authors also investigate the use of hybrid algorithms, where, at an initial stage, a heuristic is employed to locate the region where the global optimal lies and, then, the SQP is used to faster explore the neighbourhood of this region. Results showed that the proposed hybrid

algorithms managed to find better designs than those obtained by the heuristics or by the SQP alone at a reduced computational effort compared to the SQP procedure.

More recently, Kou *et al.*[78] reported that the PSO outperformed classical algorithms, namely Active Set Algorithm (ASA) and trust-region algorithm regarding the optimization of FGM. The study also found out that, for the same computational effort, the PSO found higher quality designs than the ASA or trust-region algorithm. The authors stress that this is caused by the fact that the PSO neither assumes continuity, nor the existence of the derivative of the objective function, whereas the classical algorithms heavily rely on such assumptions. In addition to that, classical gradient or sensitivity based approaches can be extremely susceptible to be trapped by local minima since they tend to capture the right path to the nearest optimum regardless of its nature (local or global optimum) very fast [78, 77].

Not surprisingly, heuristics algorithms are among the most frequently used methodologies used to optimize FG and laminated structures [12, 13]. In this work, the modified PSO algorithm implemented by Barroso[70] is used to carry out the optimization processes. The algorithm is discussed in details in the following section.

Generally speaking, a constrained optimization problem may be described as:

$$\begin{cases} \text{Find} & \mathbf{x} \\ \text{that minimizes} & f(\mathbf{x}) \\ \text{subjected to} & g_i(\mathbf{x}) \leq 0 \quad i = 1,2,\ldots,N_{ic} \\ \text{with} & \mathbf{x}_{lb} \leq \mathbf{x} \leq \mathbf{x}_{ub} \end{cases} \tag{4.1}$$

where $\mathbf{x}_{lb}$ and $\mathbf{x}_{ub}$ are the lower and upper bounds of the design variables $\mathbf{x}$, respectively, g_i is the i-th constraint and N_{ic} is the number of inequality constraints. The most frequent objectives in laminated composite optimization problems are the buckling load maximization [79, 80, 81, 82], weight minimization [39, 75], maximization of first natural frequency [83, 84], cost minimization [39, 38] or a combination of some of these criteria [85, 86]. To fit the mathematical formulation shown in Eq. (4.1), maximization is simply understood as the minimization of the negative of the objective function. Finally, it is worth mentioning the remarkable interest from researchers in developing and applying methods for multi-objective optimization. To a more complete review, the reader is encouraged to look for the reference Nikbakt *et al.*[13], where a comprehensive survey including over 300 papers on the matter is presented.

As for FGMs, a recent study by Nikbakht *et al.*[12] found that the material distribution pattern is the most common design variable. The authors also found that the stress distribution,

critical buckling load, natural frequency and weight are among the most popular objective functions. Many researchers take advantage of the simplicity of implementation and use the Power-law index as the design variable [87, 34, 10, 57]. It is also quite frequent the use of B-splines [88, 47, 49, 48] and piecewise cubic interpolation [60, 56, 34] to describe the volume fraction distribution of FG structures. Both models allow more design flexibility than simple closed-form expressions.

Of course, the process of designing such complex structures will inevitably involve the need for the consideration of constraints. For laminated structures, these are usually related to maximum displacements and/or strains, minimum values of fibre strength and minimum buckling load factor. For FG structures, the minimum ratio of volume fraction of a given material, minimum natural frequency, and maximum stress are often considered.

4.1 Particle Swarm Optimization

Particle Swarm Optimization was first proposed by Kennedy and Eberhart [89] based on the behaviour of animal packs, such as bird flockings, fish schooling and herds searching for food. PSO was initially designed for unconstrained and continuous problems, but it is nowadays a widely used algorithm for discrete design variables as well. In this work, the implementation carried out by Barroso[70] on the Biologically Inspired Optimization System (BIOS) software is used.

The core idea of this metaheuristic algorithm is that each particle of the swarm searches for food based on its own experience (cognitive aspect) and on the social sharing of the experience of others particles (social aspect). In other words, each particle roams across the design space based on its position ($\mathbf{x}_j$) and velocity ($\mathbf{v}_j$) looking for the position (i.e. design) that provides the lowest objective function. At the beginning, the positions and velocities are randomly generated for all N_p particles, and in the following iterations, they should be updated as follows:

$$\mathbf{x}_j^{i+1} = \mathbf{x}_j^i + \mathbf{v}_j^{i+1} \tag{4.2}$$

where $\mathbf{v}_j^{i+1}$ is defined by:

$$\mathbf{v}_j^{i+1} = w\,\mathbf{v}_j^i + c_1\,r_1(\mathbf{x}_{p,j}^i - \mathbf{x}_j^i) + c_2\,r_2(\mathbf{x}_{g,j}^i - \mathbf{x}_j^i) \tag{4.3}$$

where w is the inertia weight, c_1 is the cognitive factor, c_2 is the social factor, r_1 and r_2 are uniformly distributed random numbers in the range of $[0,1]$, $\mathbf{x}_{p,j}^i$ is the best position the particle

j obtained during the process until present iteration and $\mathbf{x}^i_{g,j}$ is the best position the particles on the neighborhood of particle j found so far.

In Eq. (4.2), $\mathbf{v}^{i+1}_j$ represents the direction and magnitude with which particle j should move in the next iteration. To define it, three vectors are considered, as shown in Eq. 4.3 and illustrated in Fig. 8. The first term (depicted as the continuous blue line) represents the tendency of the particle continue its the current movement (inertia). The second term (depicted as the green continuous line) corresponds to the preference of the particle of searching around the position where it has obtained its best fitness so far. Finally, the third term (depicted as the dark green continuous line) accounts for the collaboration of other particles of the swarm with the best position found until then.

Figure 8 – The $i+1$ movement of particle j

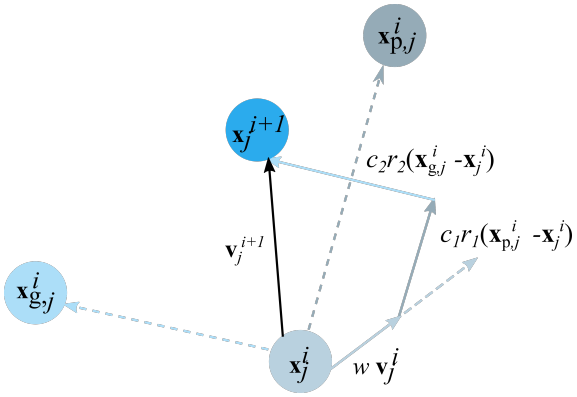

Source: the author.

In the early version of the PSO, the definition of the global best ($\mathbf{x}^i_{g,j}$) was taken as the best position found among all particles since the entire swarm is connected. This type of swarm structure was later named as Global Topology. The Global Topology leads to a fast convergence, but may be highly susceptible to premature convergence to non-optimal solutions [90]. To overcome this issue, other swarm topologies may be used [91, 90]. Two popular choices that present good results in a wide range of problems is the Ring Topology and the Square Topology. For the first choice, each particle is influenced by (and has influence on) two others. In the Square Topology, the swarm is arranged in matrix format and each particle may share information with the particles above, below, on the right and on the left of its index position. Fig. 9 illustrates the three mentioned topologies. The so-called standard PSO[92] uses the Ring topology.

On the optimization of laminated composites, Barroso[70] suggests that the Global Topology with the mutation operator and the Square Topology (with or without the mutation) are

the configurations that led to the best performances.

Figure 9 – Swarm Topologies

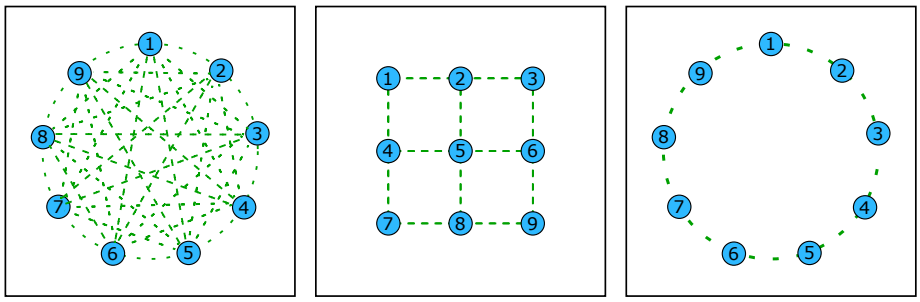

(a) Global (b) Square (c) Ring

Source: Ribeiro *et al.*[50].

Figure 10 – Boundary constraints handling

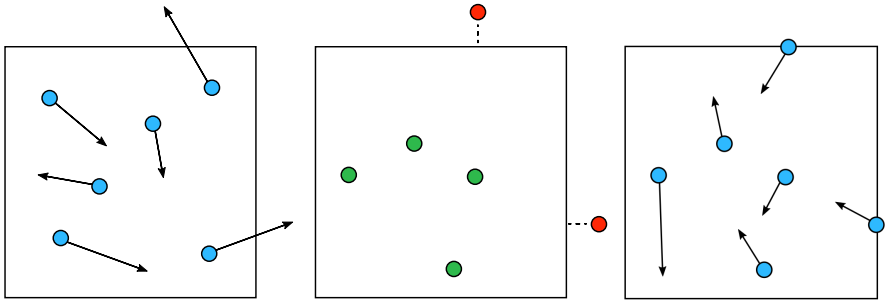

(a) Define the velocity (b) Handle violations (c) New positions

Source: Ribeiro *et al.*[50].

To deal with the side constraints violations, a simple procedure presented by Clerc[93] is adopted: the variable that had its bounds violated is set to the bound and its velocity is modified by setting it to the opposite direction with half of its magnitude. This will affect the following iterations due to the inertia factor in Eq. (4.3). Fig. 10 illustrates this procedure.

The other constraints are handled using the penalty function approach briefly described in Section 4.1.2. This process continues until a stopping criterion is met. In this work, two stopping criteria are considered: the maximum number of iterations (It_{max}) and the maximum number of iterations without improvement ($StallGen$). The algorithm is terminated when at least one of them is satisfied. The flowchart of the PSO used in this work is shown in Fig. 11. Note that the operator with the dashed green border is only triggered for laminated composite problems. Also, the term "fit", commonly found in GAs, is used to refer to the evaluation of the objective function, constraints and the penalty function.

Figure 11 – Flowchart of PSO

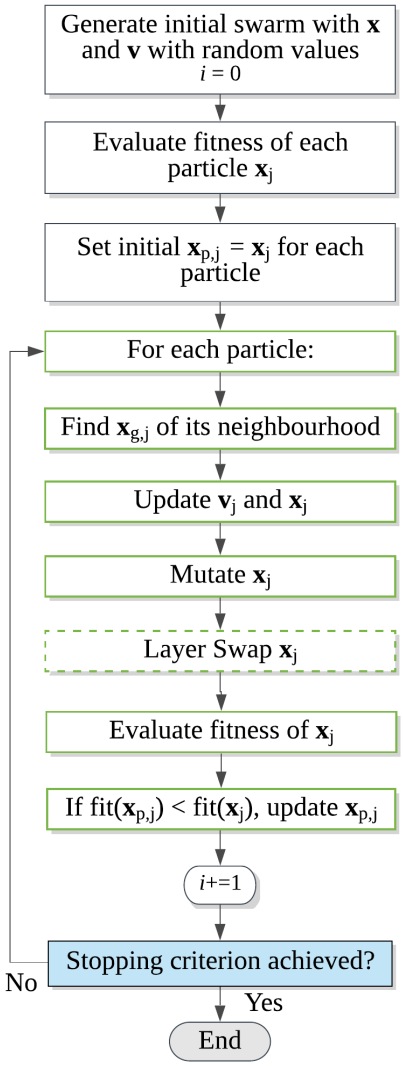

Source: the author.

4.1.1 Mutation

Despite the ability to improve the exploratory capacity of the algorithm [92, 70], the Square and the Ring topologies may also suffer from premature convergence for multimodal problems as the particles are attracted to the current best solution found by neighboring particles. To avoid this problem, a Mutation operator inspired by GAs is introduced to maintain the swarm diversity.

This operator is applied to the particle position and acts in each design variable by generating a random number between 0 and 1. If this number is less than or equal to the probability of mutation (p_{mut}), an integer number between the lower and upper bounds is

generated. When dealing with continuous design variables, the mutation is applied to the particle velocity and a real-coded number between the lower and upper bounds is generated. In all cases, this procedure is followed by the side constraints verification.

4.1.2 Constraint Handling

In this work, the approach used to deal with constrained problems was proposed by Deb[94]. The method aims to eliminate the need for a penalty parameter. This is done by comparing solutions in terms of the constraints violations. Therefore, unfeasible designs are not entirely removed from the search, but are automatically surpassed by feasible designs as the penalized objective function (i.e. the particle fitness) is evaluated as:

$$f_p(\mathbf{x}) = \begin{cases} f(\mathbf{x}) & \text{if } \mathbf{x} \text{ is feasible.} \\ f_{max} + \sum_{i=1}^{n_c} \max(c_i(\mathbf{x}), 0), & \text{otherwise.} \end{cases} \tag{4.4}$$

where f_{max} is the objective function of the worst feasible solution in the neighbourhood, c_i is the i-th constraint and n_c is the number of constraints.

It is worth mentioning that the constraint handling described in this section is only used for the conventional optimization using HFM. When the objective function and/or constraints are approximated by a surrogate model, other approaches that consider the uncertainty of the surrogate model are employed. These will be explored in Section 6.

4.1.3 Optimization of Laminated Composites

In the hybrid PSO proposed by Barroso[70], an important aspect for the optimization of laminated composite problems relies on the special encoding scheme adopted for the consideration of discrete variables. The encoding and decoding process are briefly discussed in the following section. To take advantage of it and aiming at the improvement of the algorithm performance, a laminate operator named Layer Swap is considered. The use of special laminate operators is a longstanding feature explored in the literature and were successfully explored in the works of Riche and Haftka[79], Almeida and Awruch[95], Rocha *et al.*[28], among many others.

4.1.3.1 Encoding

In this work, the design variables of laminated structures go through a encoding process, implemented on BIOS by Rocha[96] and Barroso[70]. In this process, each particle position is represented by a matrix of integers formed by three lines and *m* columns, as shown in Fig. 12 (a), where *m* depends on the maximum number of plies of the laminate.

In this matrix, each column represents a ply, and each row stores information regarding the thickness, fibre orientation, and material. In this work, only laminates with fixed ply thickness are investigated. However, it is worth mentioning that this process allows the variation of the laminate thickness (since the ply thickness may be 0). Also, the last row, which corresponds to the material properties of each ply, allows the optimization of hybrid laminates, for example. This scheme also makes it easier to deal with special layups such as symmetric and balanced types. The encoding and decoding process are illustrated in Fig. 12 (a).

Figure 12 – Encoding and decoding process

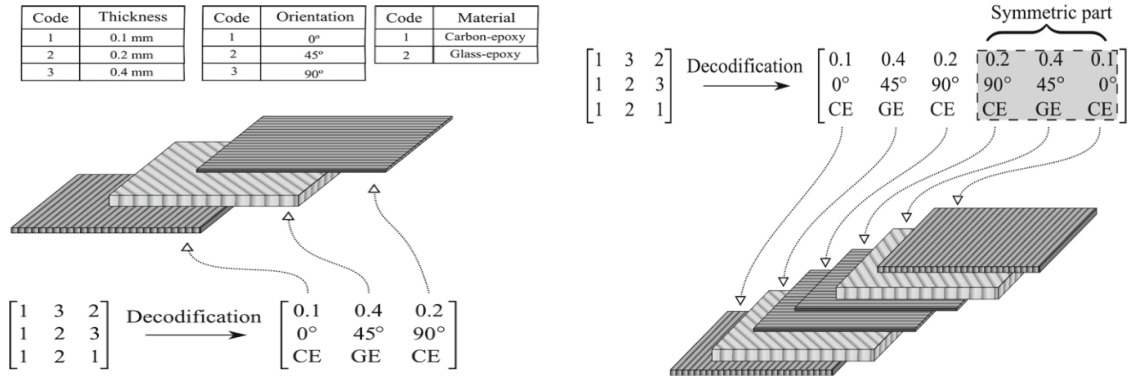

(a) General layup (b) Symmetrical layup

Source: Barroso *et al.*[27]

For example, in case of a symmetric layup, each column represents two plies symmetric about the laminate midplane. Thus, the number of design variables is only half the maximum number of layers in the actual structure, as shown in Fig. 12. It is worth mentioning that if a ply has thickness equal to 0, that ply is represented in the matrix of $3 \times m$, but should be ignored when decoding for the evaluation of the objective function and constraints.

The particle velocity is represented by a matrix with the same dimensions, but with real numbers. Therefore, after updating the particle position according to Eq. (4.3), the resulting values are rounded to the closest integer.

4.1.3.2 Layer Swap

This operator works by swapping two plies (represented by one column each) of positions in a laminate without modifying any of its original characteristics. The Layer Swap has greater importance in problems of buckling, deflection and natural frequency as this modification is capable of modifying the bending stiffness matrix of the laminate **D** without changing its membrane stiffness matrix **A**.

The Layer Swap checks whether the laminate has at least two non-zero thickness plies. If so, a random value between 0 and 1 is generated and compared to the probability of occurrence of the operator (p_{swap}). If this value is less than or equal to p_{swap}, the algorithm seeks two random plies with non-zero thickness and swap their columns in the matrix, as illustrated in Fig. 13.

Figure 13 – Layer Swap

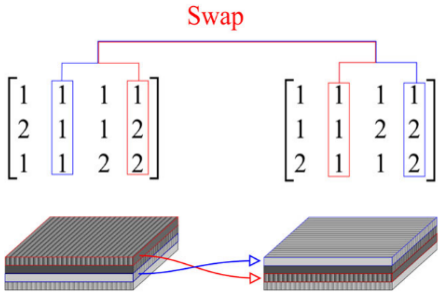

Source: Barroso *et al.*[27].

5 SURROGATE MODELLING

Surrogate models have been widely used in engineering as a way to achieve safe and reliable designs at a lower computational cost compared to the use of high fidelity models. These approximate models are an attempt of emulating the behaviour of a given function of m variables $y = f(\mathbf{x})$, which is treated as a black box, that converts the design variables vector $\mathbf{x}$ into a scalar y. This black-box function may represent experimental results or deterministic outputs provided by complex numerical simulations such as FEA or IGA.

Forrester *et al.*[18] describe the surrogate modeling procedure in three basic stages: (i) preparation of the data and choice of the modelling approach, which includes the screening of the design variables and the sampling plan definition, (ii) parameter estimation and training and (iii) model testing.

In the first stage, designers must identify which variables are relevant to the problem formulation. That is because the optimization problem complexity increases with the number of design variables, as well as the need for more robust optimization techniques. Hence the importance of selecting points in the design space that will provide a reasonable level of accuracy in the prediction made by the surrogate model ($\hat{f}(\mathbf{x})$).

A feature known as *space-fillingness* represents the capacity of sampling plans to cover the entire design space with a certain level of uniformity. This type of sampling plan is the most popular choice for computer experiments [97]. The most common sampling plan techniques are the LHS, as well as its improved version Optimized Latin Hypercube Sampling (OLHS), and pseudo-random sequences as the Hammersley Sequence Sampling (HSS). Both OLHS and HSS are said to be space-filling plans. Once the initial sampling plan is defined, the model parameters are determined to best fit the data using either estimation criteria such as the Maximum Likelihood Estimation (MLE), Cross-Validation (CV) techniques, or applying closed-form equations depending on the surrogate model choice. A broad classification used by Song *et al.*[98] distinguishes four types of surrogate models: single-fidelity, multi-fidelity, hybrid and adaptive sampling-based. Popular single-fidelity models include the classical Polynomial Regression, the Artifical Neural Networks, the Support Vector Regression, RBF and Kriging, also referred to as Design and Analysis of Computer Experiments (DACE).

Of particular interest to this work are the single-fidelity surrogate models and the adaptive sampling-based approaches, also referred to as SAO. The SAO approaches use the so-called *infill strategies* to choose new sample point(s) in the design space with high potential

to improve the model accuracy, providing a better generalization to the surrogate model.

Recently, Nikbakht *et al.*[12] and Nikbakt *et al.*[13] outlined the ANN as the most common surrogate technique in combination with meta-heuristic algorithms for the optimization of composite structures. Regarding the accuracy and robustness, Nik *et al.*[99] investigated four different techniques, namely Polynomial Regression (PR), RBF, Kriging, and SVR, to optimize a FRC plate and a cylinder with curvilinear fibres. At each generation, the training dataset was updated with the best non-repeated individual. Results showed the best performance of Kriging and RBF. Similar conclusions were reached by Simpson *et al.*[100]. The authors found that these two surrogate models tend to offer more accurate approximations over a wide range of DoE types and sampling sizes.

Kriging was used to aid the optimization of laminated structures in the works of Wenguo *et al.*[20], Passos and Luersen[22] and Keshtegar *et al.*[24]. The first two studies used the GA to maximize the infill criterion, while the latter used a PSO algorithm to sample regions of interest. As for FGM, Jaiswal *et al.*[101] proposed the use of a SAO framework based on the RBF surrogate model to minimize both geometrical and material composition errors on the additive manufacturing process of different FG structures such as cylinders, dental implants and propellers. For more applications of surrogate-based optimization in engineering design, Simpson *et al.*[100], Wang and Shan[102] and Zhao and Xue[103] present comprehensive reviews on the matter.

Furthermore, the benefits of surrogate models are not limited to computational cost reduction. The surrogate modeling itself allows an enhanced understanding of the design optimization problem (i.e. screening study).

The following section describes the main aspects involved in the definition of the initial sampling plan and a brief definition of the techniques adopted in this work. Section 5.3 and Section 5.2 present the mathematical formulation of the two surrogate models used: Kriging and Radial Basis Function, respectively.

5.1 Sampling Plan

As previously discussed, the first stage of building a surrogate model consists of data preparation. More specifically, one must identify through a small number of observations, the inputs that have a significant impact on f, as well as their search range. This may be done through engineering judgment or through systematic screening study. As a result, the design

variables vector may be shortened, reducing the so-called *Curse of Dimensionality* [18].

These observations are usually expensive to obtain, either by experiments or by numerical simulations. To give the reader a sense of time, Cardozo *et al.*[104] reported that it took 112.74 hours to generate a sampling plan with 2347 designs of a composite laminated plate subjected to an in-plane load using FEA, for example. In Forsberg and Nilsson[105], it is reported that a single analysis of a car crash takes between 4 and 6 hours to be completed as the problem requires the consideration of a large number of degrees of freedom and includes several nonlinear phenomena. The authors built a surrogate model based on 25 HF responses, which results in approximately 125 hours.

In conclusion, the longer the processing time to perform the structural analysis, the more pronounced are the benefits of using surrogate models. Thus, the spatial distribution of the sampling plan must be in such a way that the capability of generalization of the surrogate model is optimized with limited resources. If the sampling points are placed on the extremes of the design domain, it is very likely that a prediction in the centre of it is going to be of poorer quality since the model needs to make far-reaching extrapolations. As a result, the algorithm may be lead to false conclusions on the optimum design [18].

Therefore, space-filling sampling plans are of high importance [100]. The full-factorial sampling technique is the most straightforward approach, although it is easily affected by the Curse of Dimensionality as the number of variables increases. A vast literature is available on screening strategies and sampling plans. Simpson *et al.*[100] compare five different sampling plans (LHS, HSS, Orthogonal Arrays, Uniform Design and Random Set of Points) and four approximation models (Polynomial Response Surface, Kriging Models, Radial Basis Functions and Multivariate Adaptive Regression) in terms of accuracy considering two engineering problem including nonlinear behaviour. On the DoE type, the authors suggest the use of the Uniform Design and HSS, since these techniques have consistently presented low Root Mean Squared Error (RMSE) values associated. A similar conclusion is presented by Mullur and Messac [97].

No formal guidelines exist to define the minimum number of sampling points to build a surrogate model, which also motivates the use of the SAO. However, there are a few recommendations in the literature. Jin and Jung[106] use as a rule of thumb $n \approx 10\ m$, where n is the number of sampling points, and Amouzgar and Strömberg[107] use the number of required points to interpolate a quadratic polynomial as a reference to estimate the sample size of the RBF surrogate model, whilst De Ath *et al.*[108] bet on a much smaller sample: $n = 2\ m$.

Another aspect to be considered is the scaling of the design variables to $[0,1]^m$. This is a standard procedure to eliminate the effect of scale discrepancy on the surrogate model performance, particularly when defining the widths of the RBF. Forrester *et al.*[18] state that the scaling of the observed data does not affect the values of the Kriging hyperparameters, but the scaling of the design space does. Thus, the normalized design variables can be described by:

$$x_{i_{sc}} = \frac{x_i - x_{lb}}{x_{ub} - x_{lb}} \qquad i = 1, 2, \ldots, m \tag{5.1}$$

where x_{lb} and x_{ub} are the lower and the upper bounds of the design variable x_i.

Despite overall guidelines suggested by comparative studies, it is important to keep in mind that the relationship between the sampling plan and the surrogate model is too complex for the researchers to be too assertive on recommendations about "the best set of choices", given that the surrogate modelling is largely problem-dependent.

5.1.1 Hammersley Sequence Sampling

The Hammersley Sequence Sampling (HSS) is a low-discrepancy experimental design proposed by Kalangnanam and Diwekar[109] for placing n points in a m-dimensional hypercube based on the Hammersley's points [110]. Discrepancy is defined as a quantitative measure for the deviation of the sequence from the uniform distribution.

It consists of a deterministic method and as such cannot provide a different sampling plan with the same input parameters. The HSS provides better uniformity properties over the m-dimensional space than LHS in low-dimension [107], but it may be significantly affected as the dimensionality increases [107, 111], particularly when $m > 6$ [112].

5.1.2 Latin Hypercube Sampling

The Latin Hypercube Sampling (LHS) can be obtained by splitting the design space into equally sized hypercubes (also called *bins*), placing one point in each and ensuring that from each occupied bin it is possible to exit the design space along any direction parallel with any of the axes without encountering any other occupied bin. However, this procedure can lead to a poor sampling plan in terms of "space-fillingness" [18].

To overcome this issue, a metric known as *maximin* can be used to quantify the uniformity of a LHS. Based on it, Morris and Mitchell[113] proposed a criterion to find the best

LHS arrangement, also known as the OLHS, by minimizing the following scalar:

$$\Phi_q(\mathbf{X}) = \left(\sum_{i=1}^{dn} J_i d_i^{-q} \right)^{1/q} \tag{5.2}$$

where dn is the number of unique values of distances between all possible pairs of points in the sampling plan $\mathbf{X}$, J_i is the number of pairs of points separated by the same distance d_i and q is a scalar value, which is suggested to be $q = 1,\ 2,\ 5,\ 10,\ 20,\ 50$ and 100 [18]. This way, the smaller the value of Φ_q the better the space-filling properties of the sampling plan $\mathbf{X}$. This could be solved by a GA, for example.

To save computational effort, a much simpler approach can be used: simply run N_{sp} sampling plans and select the one with highest *maximin*. In this work, this approach will be referred to as $\text{LHS}_{N_{sp}}$. Fig. 14 illustrates the discussed sampling plan techniques for $n = 10$ and $m = 2$ in the scaled design space [0, 1].

Figure 14 – Sampling plans for $n = 10$ and $m = 2$

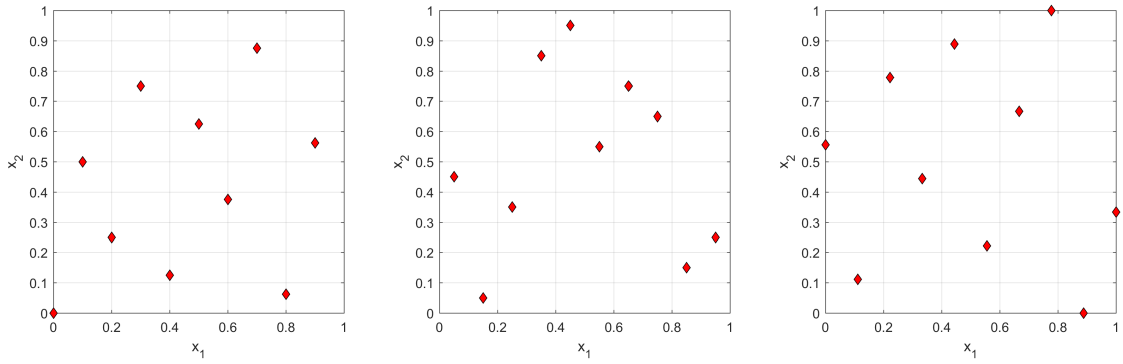

(a) Hammersley Sequence (b) Latin Hypercube (c) LHS_{50}

Source: the author.

For laminated composite problems, where discrete variables are considered, this work employed the following methodology:

1. Each dimension is divided into k spaces, where k is the number of possible values of the design variable m_j;
2. Round the sampling points between the intervals to the respective integer;
3. Remove repeated points before evaluating the HFM responses.

For example, if x_1 and x_2 represent the allowable values of fibre orientation $[0°/45°/90°]$ of a laminated plate, the sampling plan shown in Fig. 14 would be adapted to the distribution presented in Fig. 15. Note that the light blue box on the right corner has 2 sampling points placed in the same interval, as well as the one in the middle of the sampling plan, resulting in

the superposition and consequent removal of one of the sampling point so that the algorithm will not evaluate twice the same area. To be fair, the adapted sampling plan is no longer a Latin Hypercube (LH) since there is more than one point in each bin. A similar approach is presented in Maschio and Schiozer[114].

Figure 15 – LHS_{50} for $n = 10$ and $m = 2$ adapted for discrete design variables

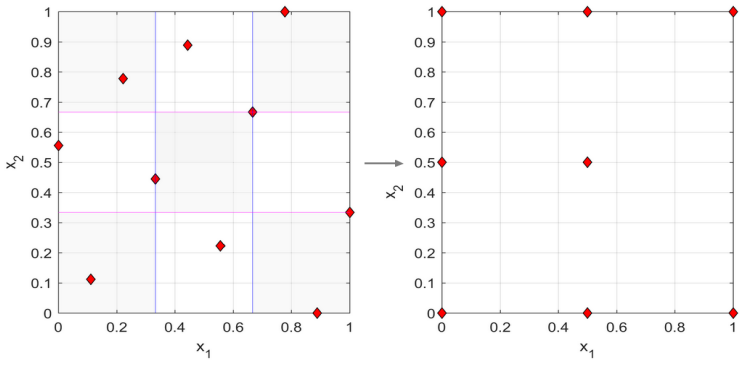

Source: the author.

5.2 Kriging

Kriging is a surrogate model developed by the mining engineer Daniel Krige and made its way into engineering design through the work of Sacks *et al.*[115] when the technique was applied to the approximation of computer experiments. Kriging is a nonparametric interpolating model, which means that the training points are involved in the determination of the unknown parameters and that the model exactly interpolates the responses at the sampling points. Kriging has multiple variants and its general form may be described as:

$$\hat{f}(\mathbf{x}) = g(\mathbf{x}) + Z(\mathbf{x}) \tag{5.3}$$

where the first term concerns the global trend of the model and the second term refers to the localized deviations (or *departures*) that are autocorrelated. In this work, boldface indicates a vector or a matrix.

In Universal Kriging, also known as Regression Kriging, the first term is given by a set of regression functions (e.g. linear, quadratic or any other order of polynomial) to shape the global trend, which varies with the sampling point location, as shown in Fig. 16 (b). However, it is very common the assumption of a unknown and constant global trend (μ), which results in

Figure 16 – Types of Kriging

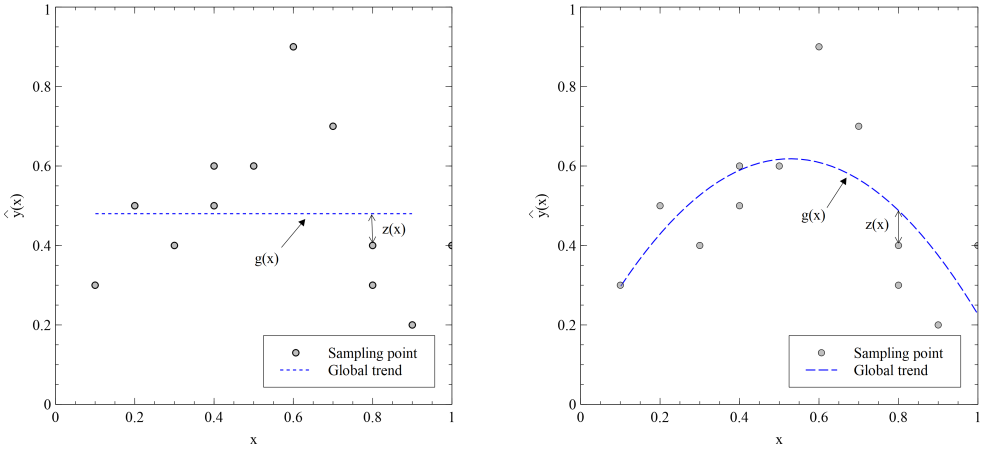

(a) Ordinary Kriging (b) Regression Kriging

Source: the author.

the definition of the Ordinary Kriging, the version used in this work and depicted in Fig. 16 (a). Finally, when μ is a known stationary mean we arrive at the Simple Kriging.

In Kriging, the responses (targets) are interpreted as the result of a stochastic process, even when dealing with a deterministic computer code (e.g., FEA or IGA). More specifically, in Eq. (5.3), $Z(\mathbf{x})$ is assumed to be a realization of a Gaussian process with mean zero and covariance given by [116]:

$$\text{cov}[\mathbf{Y},\mathbf{Y}] = \sigma^2\,\Psi \tag{5.4}$$

here σ^2 is the process variance and Ψ is the correlation matrix of all sampling points. To build this matrix, the observed responses $\mathbf{y} = \{y^{(1)}\ y^{(2)}\ \ldots\ y^{(n)}\}^T$ from the sample data $\mathbf{X} = \{\mathbf{x}^{(1)}\ \mathbf{x}^{(2)}\ \ldots\ \mathbf{x}^{(n)}\}^T$ are represented by a set of normally distributed random variables $\mathbf{Y} = \{Y^{(1)}\ Y^{(2)}\ \ldots\ Y^{(n)}\}^T$ with mean $\mathbf{1}\,\mu$, where $\mathbf{1}$ is an n x 1 vector of ones. These random variables are spatially correlated with each other using a correlation function. In this work, two types are investigated: a Gaussian function, given by:

$$\text{cor}[Y(\mathbf{x}^{(i)}), Y(\mathbf{x}^{(l)})] = \exp(-\sum_{j=1}^{m} \theta_j\, d^{p_j}) \tag{5.5}$$

and the Matérn 5/2 function, given by:

$$\text{cor}[Y(\mathbf{x}^{(i)}), Y(\mathbf{x}^{(l)})] = \prod_{j=1}^{m} \exp\Big(-\frac{\sqrt{5}d}{\theta_j}\Big)\Big(1+\frac{\sqrt{5}d}{\theta_j}+\frac{5d^2}{3\theta_j^2}\Big) \tag{5.6}$$

where $d = |x_j^{(i)} - x_j^{(l)}|$. These kernels were chosen due to their good performance in a wide range of surrogate model applications [117, 118].

Thus, the correlation matrix (Ψ) of all sampling points can be evaluated as:

$$\Psi = \begin{bmatrix} \text{cor}[Y(\mathbf{x}^{(1)}), Y(\mathbf{x}^{(1)})] & \text{cor}[Y(\mathbf{x}^{(1)}), Y(\mathbf{x}^{(2)})] & \text{cor}[Y(\mathbf{x}^{(1)}), Y(\mathbf{x}^{(n)})] \\ \text{cor}[Y(\mathbf{x}^{(2)}), Y(\mathbf{x}^{(1)})] & \text{cor}[Y(\mathbf{x}^{(2)}), Y(\mathbf{x}^{(2)})] & \text{cor}[Y(\mathbf{x}^{(2)}), Y(\mathbf{x}^{(n)})] \\ \vdots & \ddots & \vdots \\ \text{cor}[Y(\mathbf{x}^{(n)}), Y(\mathbf{x}^{(1)})] & \dots & \text{cor}[Y(\mathbf{x}^{(n)}), Y(\mathbf{x}^{(n)})] \end{bmatrix} \tag{5.7}$$

This matrix is positive semi-definite and symmetric with diagonals of ones as a result of the correlation function given by Eq. (5.5) and Eq. (5.6). To compute Ψ, the hyperparameters $\mathbf{p}$ and θ must be determined. This is a vital step to the model fitting since these parameters have a huge influence on the response surface and on the model accuracy. To illustrate this idea, Fig. 17 (a) presents the behaviour of a Gaussian function with $\theta_j = 1.0$ fixed and varying p_j. It can be observed that the increase of this parameter leads to a smoother variation of the spatial correlation. In particular, for the lowest value considered, a near discontinuity occurs between near points.

In Fig. 17 (b), p_j is fixed at 2.0 and θ_j varies from 0.1 to 4.0. A low value of θ_j means that all sample points are highly correlated. In other words, $Y(x_j)$ is similar across the sample, while a high value indicates that the values of $Y(x_j)$ are significantly different. Therefore, θ_j may be understood as a measure for how "active" is the approximated function regarding the design variable x_j. This process is also known as Automatic Relevance Determination and is a valuable metric to understand the relevance of each variable to the problem formulation [119, 120]. One must be cautious when extending the above-mentioned considerations to the Matérn 5/2 correlation function, in which the hyperparameter θ_j is on the denominator of the fraction. Therefore, in this case, lower values of θ_j indicate a more active design variable, as illustrated in Fig. 17 (c).

Several techniques to obtain the hyperparameters were proposed in the literature, being MLE and CV the most popular ones. In this work, the first approach is used to estimate the hyperparameters of Kriging. The Likelihood Function (LF) may be described as:

$$L(\mathbf{Y}|\ \mu, \sigma) = \frac{1}{(2\pi\sigma^2)^{n/2}}\ \exp(-\frac{\sum(\mathbf{Y}^{(i)} - \mu)^2}{2\sigma^2}) \tag{5.8}$$

Expressing this equation in terms of the sample data, we have:

$$L = -\frac{1}{(2\pi\sigma^2)^{n/2}|\Psi|^{1/2}}\exp(\frac{(\mathbf{y} - \mathbf{1}\mu)^T\Psi^{-1}(\mathbf{y} - \mathbf{1}\mu)}{2\sigma^2}) \tag{5.9}$$

Figure 17 – Variation on the hyperparameter of the correlation functions

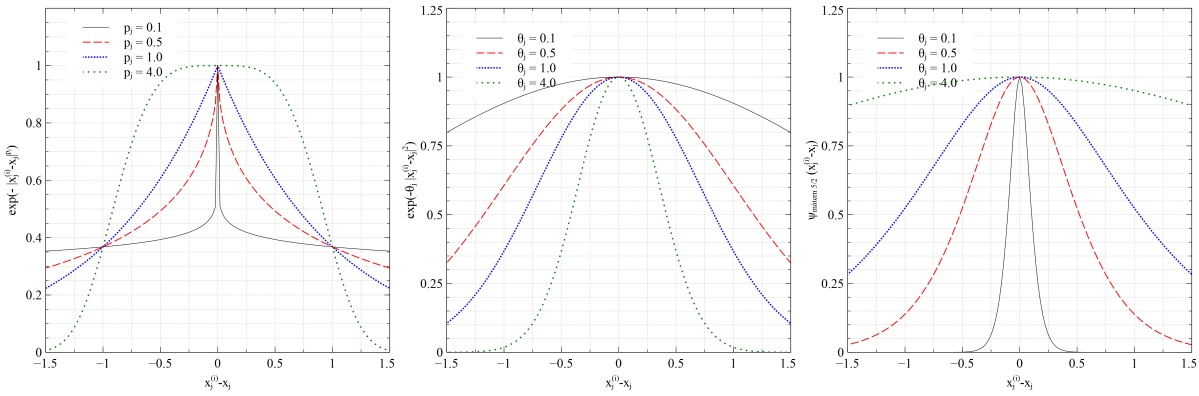

(a) Varying p_j and θ_j = 1.0 (b) Varying θ_j and $p_j = 2$ (c) Matérn 5/2 with varying θ_j

Source: the author.

Taking the natural logarithm to simplify the maximization:

$$\ln(L) = -\frac{n}{2}\ln(2\pi) - \frac{n}{2}\ln(\sigma^2) - \frac{1}{2}\ln(\Psi) - \frac{(\mathbf{y}-\mathbf{1}\mu)^T\Psi^{-1}(\mathbf{y}-\mathbf{1}\mu)}{2\pi\sigma^2} \tag{5.10}$$

To obtain the estimates for μ and σ^2, one must differentiate $\ln(L)$ with respect to each of the variables and equate them to 0, which gives:

$$\hat{\mu} = \frac{\mathbf{1^T}\Psi^{-1}\mathbf{y}}{\mathbf{1^T}\Psi\mathbf{1}} \qquad \hat{\sigma}^2 = \frac{1}{n}(\mathbf{y}-\mathbf{1}\hat{\mu})^T\Psi^{-1}(\mathbf{y}-\mathbf{1}\hat{\mu}) \tag{5.11}$$

where $\hat{\mu}$ and $\hat{\sigma}^2$ are the estimates for the mean and variance, respectively. Replacing these estimates in Eq. (5.10) and removing constant terms, we obtain what is known as *concentrated ln-likelihood function*:

$$\ln(L) \approx -\frac{n}{2}\ln(\hat{\sigma}^2) - \frac{1}{2}\ln|\Psi| \tag{5.12}$$

Unfortunately, this function cannot be differentiated in order to obtain an analytic expression to describe the hyperparameters, as done to the mean and the variance of the process. Thus, a numerical optimization technique must be used to find the hyperparameters that maximize this function. For a given value of $\mathbf{p}$ and θ, the estimates $\hat{\mu}$ and $\hat{\sigma}^2$ can be computed and used to evaluate Ψ, thus, enabling the calculation of the ln-likelihood function.

Typically, $\mathbf{p}$ is not treated as variable and only θ need to trained, reducing the complexity and size of the Kriging optimization problem. Normally, this exponent assumes 3 values: $p_j = 1$, characterizing a exponential correlation function, $p_j = 2$, characterizing a Gaussian function or $0 < p_j < 2$, which corresponds to a general exponential [121]. The most commonly used value is $p = 2.0$ [19, 121, 122], which is also adopted in this work.

Therefore, the MLE may be described as an unconstrained optimization problem in the form of:

$$\begin{cases} \text{Find} & \mathbf{x} = \{\theta_i\} \text{ for } i = 1,2,\ldots,m \\ \text{that maximizes} & \ln(\mathrm{L})(\mathbf{x}) \\ \text{with} & \theta_{lb} \leq \theta_i \leq \theta_{ub} \end{cases} \tag{5.13}$$

where θ_{lb} and θ_{ub} refer to the lower and upper bounds of the hyper-parameter θ_i, respectively. Note that the design variables of the MLE are different than the ones considered to the optimization of the problem itself. In this case, all variables are continuous and their search ranges are user-defined. In this work, the PSO algorithm is used to solve this problem. The search bounds are often considered to be in logarithmic scale [18, 123] as there is significant change between $\theta = 0.1$ and $\theta = 1.0$, as shown in Fig. 17 (b). Therefore, θ is always positive and greater than 0. Alternatively, if n and m are not too large, direct search through the search space may be used.

In general, two types of problem may arise when using the MLE. The first type concerns the multi-modality of the ln-likelihood landscape, as well as the long ridges of nearly constant and optimal values that may lead to numerical difficulties for gradient-based problems [124, 19, 121]. The second type of problem is related to the ill-conditioned correlation matrices. On this matter, Davis and Morris[125] provided an insightful investigation on the determination of the Kriging parameters and the factors that could affect the model performance using the condition number[1] of the correlation matrix Ψ. A large condition number will result in a matrix that may have significant numerical inaccuracies when inverted. This may be caused by large correlation ranges and closely located observations [125]. The same remarks were made by Martin and Simpson[19].

A common approach to improve the conditioning of the correlation matrix Ψ is to add a small constant value to its diagonal elements, also known as *nugget effect*, *jitter* or *diagonal inflating*. This is the approach adopted by Forrester *et al.*[18], Roustant *et al.*[126] and Bachoc[123]. Roustant *et al.*[126] and Bachoc[123] recommend $\tau = 1 \times 10^{-8}$, but highlight that this value should be adjusted in a way that it's not too large that causes significant departures, but not too small to prevent numerical issues. This is also the approach adopted in this work. It is worth mentioning that the interpolating properties of the Ordinary Kriging are not affected.

For illustrating the multi-modality of the ln-likelihood function, the Branin function

[1] The condition number of a matrix is defined as the ratio of the absolute values of the largest and smallest eigenvalues of the correlation matrix Ψ[125].

is studied in the following. This function is given by:

$$f(\mathbf{x}) = (x_2 - \frac{5.1}{4\pi^2}\, x_1^2 + \frac{5}{\pi}\, x_1 - 6)^2 + 10(1 - \frac{1}{8\pi})\cos(x_1) + 10 \tag{5.14}$$

Fig. 18 presents three iterations of the SAO approach (to be discussed in Chapter 6) employed in this work. The red diamonds are the sampling points, the white ones are the location of the optimal solutions and the green ones are the infill points. On the right side, the approximated surface using the best hyperparameters (their locations are marked by the magenta points) is shown. Note how the ln-likelihood surface presents multiple peaks and valleys and how it shifts its peak to a new θ as new points are added to the sampling plan.

Finally, to predict the target response at a new point $\mathbf{x}^*$, we need to look back at Eq. (5.3). The first term is the estimated mean of the Gaussian process and is obtained by the MLE, as shown in Eq. (5.11), that would be the result of simply plugging $\mathbf{x}^*$ in $\hat{y}(\mathbf{x}^*)$ if no correlation was considered between the unseen point and the sampling points. Therefore, the second part of Eq. (5.15) must be obtained by correlating the errors of the unseen point to the sampling points used to train the surrogate model. The farther is the unseen point, the lower is this correlation and the mean behaviour of the approximate response surface ($\hat{\mu}$) is in fact the best prediction.

To do so, one must acknowledge that the prediction must be the most consistent with the estimated behaviour modelled by MLE hyperparameters. That being said, a intuitive way of understanding its derivation is discussed by Jones *et al.*[127] and Forrester *et al.*[18]. Suppose the guessed value of the function at $\mathbf{x}^*$ is, say, y^*, allowing the evaluation of the likelihood of the augmented data. This value aims to quantify how much the pseudo observation 'fits' with the original data. As a result, for each guess, we would get a different likelihood value. It turns out that the value of y^* that maximizes this augmented likelihood, and in this sense is most consistent with the function's typical behavior, is precisely the predictor described by:

$$\hat{y}(\mathbf{x}) = \hat{\mu} + \psi^T\, \Psi^{-1}(\mathbf{y} - \mathbf{1}\hat{\mu}) \tag{5.15}$$

where ψ is the correlation vector between $\mathbf{x}$ and all sampling points. The full derivation of the predictor is found in Sacks *et al.*[115].

Finally, an interesting feature of the Gaussian process is the ability to provide a measure of the uncertainty of the prediction $\hat{y}(\mathbf{x})$, given by the prediction variance, which is also known as Mean Squared Error (MSE):

$$\hat{s}^2(\mathbf{x}) = \hat{\sigma}^2\left[1 - \psi^T\Psi^{-1}\psi + \frac{(1 - \mathbf{1}^\mathbf{T}\Psi^{-1}\psi)^2}{\mathbf{1}^\mathbf{T}\Psi^{-1}\mathbf{1}}\right] \tag{5.16}$$

Figure 18 – Likelihood and prediction for Branin function

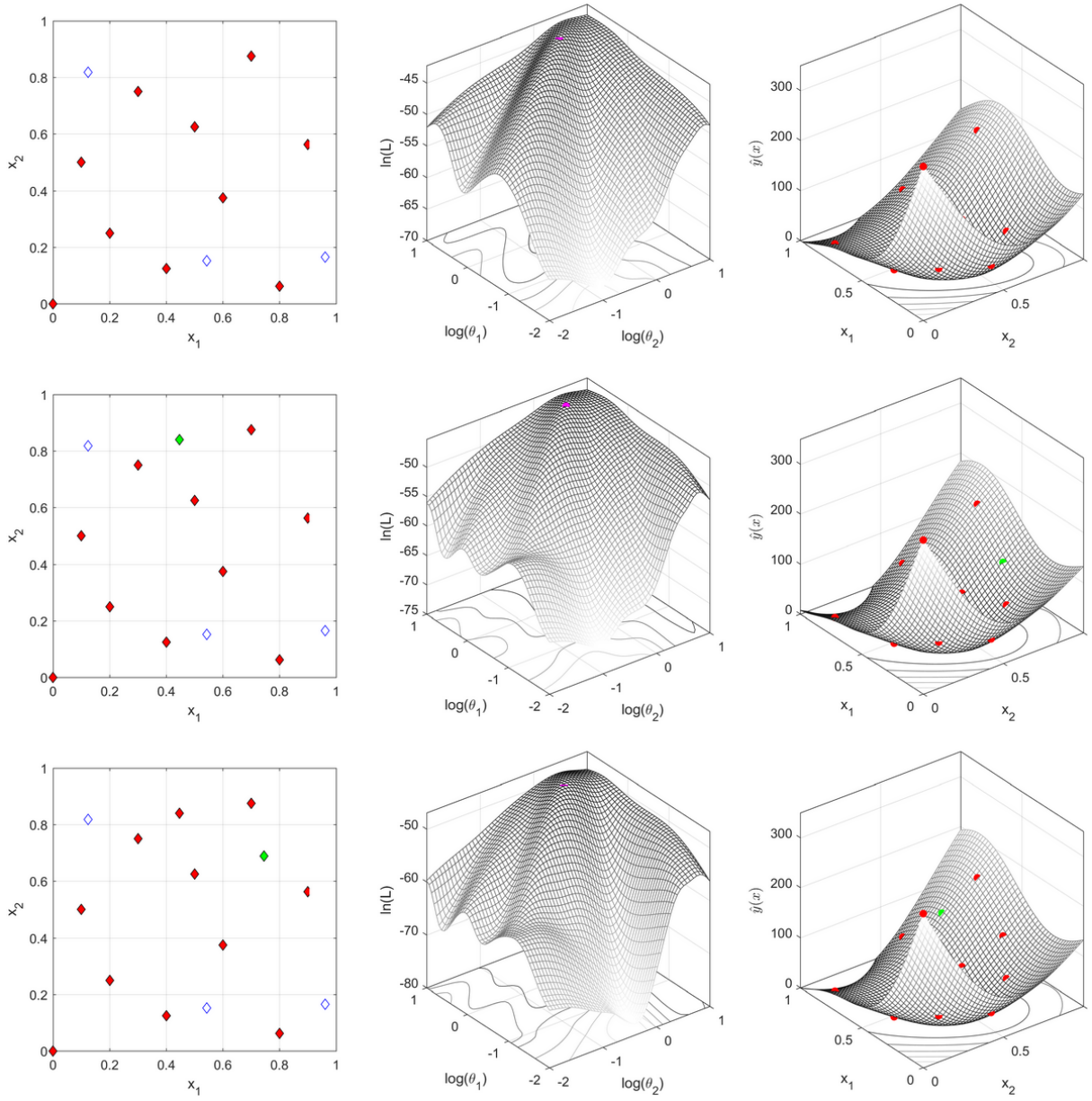

Source: the author.

The MSE provides a measure of the quality of the prediction and is always non-negative. The correlation between errors also affects the prediction accuracy in a sense that the farther we get from the sampling points, the less confidence in the prediction we get. Thus, the MSE is higher in less sampled areas and reduces to 0 in sampling points, as expected since there is no doubt about the accuracy of that point as it was evaluated using the HFM. One may also observe that, if we are calculating $\hat{s}(\mathbf{x})$ at a sampling point $\mathbf{x}$, there is a column in Ψ that correlates this point with the remaining ones, then $\Psi^{-1}\psi$ is a vector of zeros with 1 in the i-th

position, so that:

$$\psi^T \Psi^{-1} \psi = \psi^T \psi^{(i)} = \text{cor}(\mathbf{x}^{(i)},\, \mathbf{x}^{(i)}) = 1 \tag{5.17}$$

and

$$\mathbf{1}^T \Psi^{-1} \psi = \mathbf{1}^T \psi^{(i)} = 1 \tag{5.18}$$

Substituting Eq. (5.17) and Eq. (5.18) into Eq. (5.16), we obtain exactly the uncertainty we expect at sampled locations:

$$\hat{s}^2(\mathbf{x}) = \sigma^2 \Big[1 - \underbrace{\psi^T \Psi^{-1} \psi}_{1} + \frac{(1 - \overbrace{\mathbf{1}^T \Psi^{-1} \psi}^{1})^2}{\mathbf{1^T} \Psi^{-1} \mathbf{1}} \Big] = 0 \tag{5.19}$$

In Eq. (5.16), the third term accounts for the uncertainty in the estimate of μ (i.e. $\hat{\mu}$) and provides very small values. In fact, this term is often omitted [18, 128]. However, the present work will follow the Efficient Global Optimization (EGO) implementation by Jones *et al.*[127], which does consider the third term.

5.3 Radial Basis Functions

Radial Basis Functions (RBF) use a linear combination of radially symmetric functions centered around a set of points, the basis function centres, scattered around the design space according to the sampling plan [18]. This type of surrogate model was first proposed by Hardy[17] aiming at the interpolation of geographical scattered data and has since then been developed and applied in several other branches of science due to its simplicity of implementation.

Considering a scalar function $f(\mathbf{x})$ and the vector of samples containing the design variables $\mathbf{X} = \{\mathbf{x}^{(1)}, \mathbf{x}^{(2)}, \ldots, \mathbf{x}^{(n)}\}^T$ which provides the following vector of responses (or *targets*) $\mathbf{y} = \{y^{(1)}, y^{(2)}, \ldots, y^{(n)}\}^T$, a typical form of RBF can be expressed as:

$$\hat{f}(\mathbf{x}) = \mathbf{w}^T \psi = \sum_{i=1}^{N_c} w_i \; \psi \left(||\mathbf{x} - \mathbf{c}^{(i)}|| \right) \tag{5.20}$$

where N_c is the number of basis functions centres, $\hat{f}(\mathbf{x})$ is the prediction of the true response function, $\mathbf{c}^{(i)}$ refers to the ith-centre among the N_c basis function centres and ψ is the vector of size N_c containing the values of the basis functions ψ themselves, evaluated at the Euclidean distances between the testing point $\mathbf{x}$ and the centres of the basis functions $\mathbf{c}^{(i)}$.

Basis functions include linear and cubic polynomials, thin plate splines, inverse multiquadric and more popularly, Gaussian functions, as shown in Tab. 1, where r is the radial distance between the point to be estimated $\mathbf{x}$ and the sampling points, while σ is known as *spread*, *width* or *shape parameter*. The Gaussian function provides more freedom to improve the generalization at the cost of a more complex parameter estimation process. One of the reasons for its popularity is the fact that under certain assumptions, this type of function and the inverse multiquadric basis always lead to symmetric positive definite Gram Matrices [18].

Table 1 – Common basis functions

Nomenclature	$\psi(r)$
Linear	r
Cubic	r^3
Thin-plate splines	$r^2 \ln(r)$
Inverse Multiquadric	$(r^2+\sigma^2)^{1/2}$
Gaussian	e^{-r^2/σ^2}

Source: the author.

Then, enforcing the interpolation condition on the sampling points, $\hat{f}(\mathbf{x}^{(i)}) = f(\mathbf{x}^{(i)}) = y_i$, Eq. (5.20) becomes:

$$\hat{f}(\mathbf{x}^{(i)}) = \mathbf{w}^T \boldsymbol{\psi} = \sum_{j=1}^{N_c} w_j \; \psi_j \left(||\mathbf{x}^{(i)} - \mathbf{c}^{(j)}||\right) = f(\mathbf{x}^{(i)}) = y_i \tag{5.21}$$

This system is linear in terms of the basis functions weights $\mathbf{w}$ despite any possible non-linearity of the $f(\mathbf{x})$ response, which is an important characteristic of this surrogate model [98]. Additionally, one of the conditions for the system in Eq. (5.21) to have one single solution is that it must be square (i.e. $N_c = n$) and that the sampling points must be sufficiently distant from each other [18]. This is because very closely spaced points in $\mathbf{X}$ can cause ill-conditioning. As consequence, failure of the Cholesky factorization may occur. Usually, this is not a problem in space-filling sampling plans but may become an issue in the SAO approach if infill points are added subsequently in a small area of interest in the design domain. If the number of basis functions is lower than the sample size, the Method of Least Squares must be used.

In addition to that, calculations are simplified if the centres coincide with the data points, that is $\boldsymbol{c}^{(i)} = \mathbf{x}^{(i)}$ for any $i = 1 \ldots n$, which leads to:

$$\boldsymbol{\Psi}\, \mathbf{w} = \mathbf{y} \implies \mathbf{w} = \boldsymbol{\Psi}^{-1}\, \mathbf{y} \tag{5.22}$$

where Ψ is the so-called *Gram matrix* defined as:

$$\Psi = \begin{bmatrix} \psi_{11} & \psi_{12} & \cdots & \psi_{1n} \\ \psi_{21} & \psi_{22} & \cdots & \psi_{2n} \\ \vdots & \vdots & \ddots & \vdots \\ \psi_{n1} & \psi_{n2} & \cdots & \psi_{nn} \end{bmatrix} \tag{5.23}$$

whose components are given by:

$$\psi_{ij} = \exp\Big(-\frac{||\mathbf{x}^{(i)} - \mathbf{x}^{(j)}||}{\sigma_j^2}\Big) \tag{5.24}$$

Another important concern is how to avoid overfitting. This phenomenon occurs when the built model closely explain the training dataset but fails to generalize well when applied to unseen data. To address this issue, one may split the initial data set into two different subsets, one for *training* and another for *testing*. If the model performs much better on the training subset than on the testing subset, that is an indicator of overfitting. A model with high variance and low bias may also be an indicator of it. These indicators are actually tools for diagnosing overfitting and not for effectively mitigating the issue. However, being capable of acknowledging the matter is the first step towards selecting a better model, either by rebuilding it, improving it or by adding new training points.

Note that although the correct choice of the weights alone does ensure that the approximation can replicate the training data, it is not enough to guarantee a model with good generalization properties. That role is played by the choice of the model parameters (e.g. σ in the Gaussian function), which is run prior to the weights' evaluation. The determination of these parameters is discussed in the following section.

5.3.1 Width of the basis functions

Several approaches were proposed to evaluate the shape parameter σ in Gaussian, multriquadric and inverse multiquadric functions. Fig. 19 illustrates the behaviour of different types of basis function for the same σ value, and varying σ's for the same Gaussian function. It can be seen that lower values of σ may lead to non-smooth response surfaces. Moreover, too large values of spread may cause to a Runge's phenomenon in interpolation [129].

Therefore, the estimation of this parameter is a key-stage to achieving a good surrogate model. Many researchers have proposed equations that simplify its calculation, skipping an arduous task that could be itself another topic for optimization, as proposed by Wu

Figure 19 – Variation on the basis function and on spread parameter σ

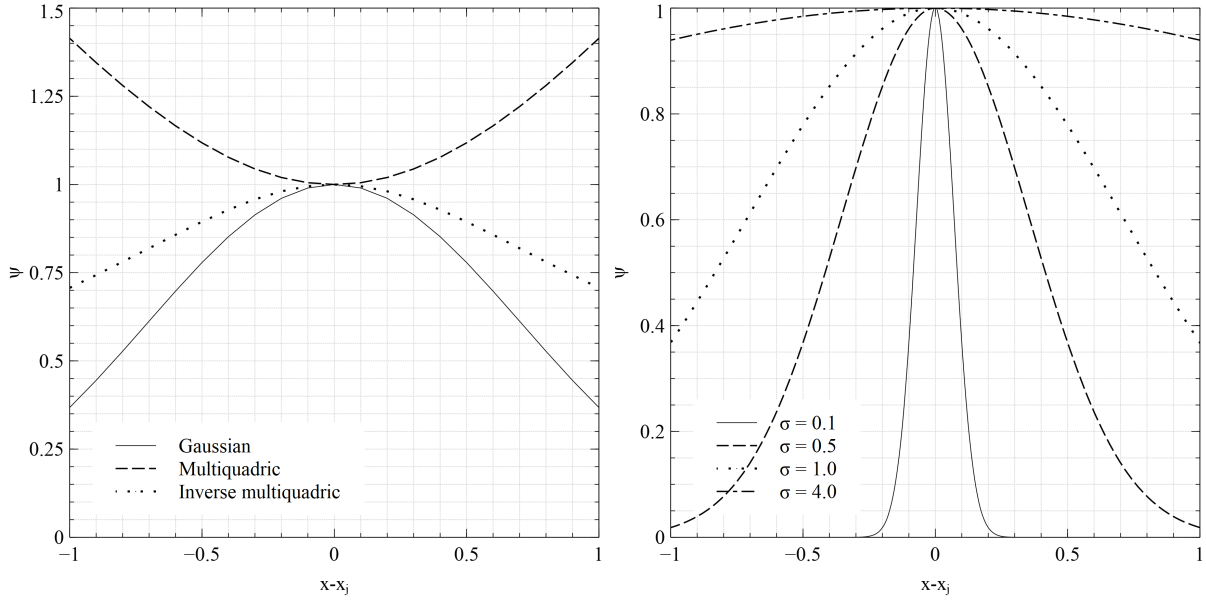

(a) Different basis functions for $\sigma = 1.0$ (b) Gaussian function with varying σ

Source: the author.

et al.[129]. Usually, the proposed closed-form expressions depend on the maximum distance between the sampling points (d_{max}). For example, Nakayama *et al.*[130] and Song *et al.*[98] used one single value of width given by Eqs. (5.25) and (5.26) for all sampling points, respectively:

$$\sigma = \frac{d_{max}}{\sqrt{2n}} \tag{5.25}$$

$$\sigma = \frac{d_{max}}{\sqrt[m]{nm}} \tag{5.26}$$

On the other hand, Kitayama *et al.*[131] and Kitayama and Yamazaki[132] considered the sparseness and density of the sampling points to propose a different spread value for each sampling point based on an adaptive scaling technique, given by:

$$\sigma_i = \frac{d_{i,max}}{\sqrt{m}\,\sqrt[m]{n-1}} \tag{5.27}$$

where $d_{i,max}$ is the maximum distance between the sampling point i and any other sampling point in the design space. In brief, the adaptive scaling technique was proposed by Kitayama *et al.*[131] and aims to make all spreads to be bigger than unity. This approach uses the following equation to scale the design variables space:

$$x_{i_{as}} = x_{i_{sc}} \times s \tag{5.28}$$

where $x_{i_{sc}}$ is the scaled design variable given by Eq. (5.1) and s is the scaling coefficient. The algorithm of this technique begins by scaling all design variables by Eq. (5.28) taking $s = 1.0$. After that, the main loop can be summarized as follows:

1. The widths of all basis functions are calculated according to Eq. (5.27);
2. Find $\sigma_{min} = \min(\sigma_i)$;
3. If $\sigma_{min} \leq 1.0$, the scaling coefficient is updated as follows: $s = \alpha \times s$. Otherwise, the algorithm is terminated and the widths found in step 2 are stored. In this work, $\alpha = 1.1$.

At a higher computational cost, one may obtain a better estimate for the basis widths using cross-validation techniques, as suggested by Ferreira *et al.*[133] and Forrester *et al.*[18]. On this matter, the Leave-One-Out Cross-Validation (LOOCV) and the k-Fold CV are the most popular ones [134]. The LOOCV's basic approach is to choose a given σ vector and build the surrogate model with all training points but one and use the one sampling point omitted from the model training to evaluate an error measure:

$$RMSE_{CV} = \sum_{i=1}^{n_v} \sqrt{\frac{(y_i - \hat{y}_i)^2}{n_v}} \tag{5.29}$$

where n_v is the number of validation points (equal to 1 for the LOOCV). After that, the process is resumed with the building of a new surrogate model using all training points except one (different from the ones already taken in previous iterations) and the error is again evaluated and added to the total cross-validation error. This process is repeated until all sampling points have been omitted for the same σ vector. Thereafter, other width vectors are tested. In the end, the σ that provided the lowest sum of $RMSE_{CV}$ is chosen as the widths vector.

In this approach, n_w surrogate models are generated for each basis j, where n_w is the number of widths tested. Thus, to define the width vector, a total of $n_w \cdot n$ surrogate models are built. This procedure is adopted by Sóbester *et al.*[135], for example. The authors test all widths of a vector with 20 values between $[10^{-2},\ 10^{1}]$ in logarithmic scale. In this work, this range is multiplied by $\sqrt{2}$ due to the difference between the Gaussian functions used.

In k-Fold CV, the initial data set is split into k different subsets, each time leaving out one of the subsets from the training and using it to measure the error between the model prediction and the HFM values of the points set aside. In this case, only $n_w \cdot k$ surrogate models are built at each iteration and n_v is equal to the subset size. Note that if the group size is 1, the k-Fold becomes the LOOCV. In this work, the k-FOLD CV is employed using the width vector suggested by Sóbester *et al.*[135], where $n_w = 20$. Fig. 20 depicts the procedure discussed.

Figure 20 – k-Fold CV

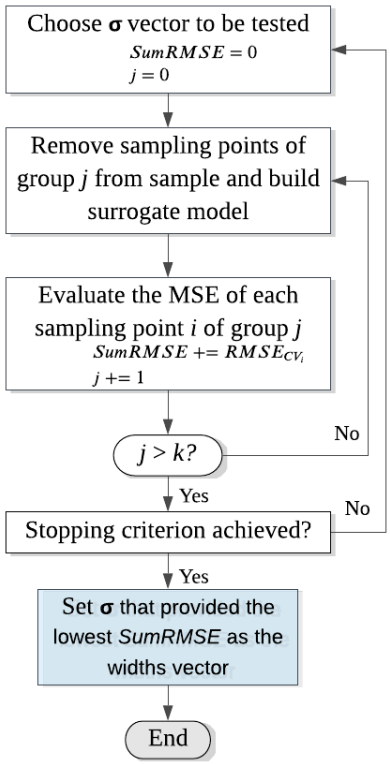

Source: the author.

On the other hand, one may use optimization techniques to select the widths, as done by Mehmani *et al.*[136]. All considered, the present work will use the two approaches that provided more accurate and reliable results in past studies [137, 50] involving composite structures: k-FOLD CV ($k = 5$) and the closed-form expression proposed by Kitayama *et al.*[131].

It is worth emphasizing that although the formulation of the MSE had been presented in the Kriging section, this metric can also be applied to RBF models with the proper assumptions about the stochastic process, allowing the computation of the EI and WEI, as discussed by Sóbester *et al.*[135]. In this case, the last term in Eq. (5.16) regarding the uncertainty of estimating μ is not considered and only the term that represents the reduction in the prediction error due to the fact that the unseen point is correlated with the sampling points is computed, which gives:

$$\hat{s}^2(\mathbf{x}) = \hat{\sigma}^2 \left[1 - \psi^T \Psi^{-1} \psi \right] \tag{5.30}$$

where Ψ is the Gram matrix, ψ is the vector containing the values of the basis functions considering the Euclidean distances between the testing point and the centres of the basis functions and $\hat{\sigma}$ is the variance of the process calculated according to Eq. (5.12). Considering $\hat{\mu} = 0$ and $\hat{\sigma} = 1$, this version is conceptually equal to Kriging.

6 SEQUENTIAL APPROXIMATE OPTIMIZATION

The concept of Sequential Approximate Optimization was first discussed by Schmidt and Farshi[138]. The authors used mathematical programming methods and approximation concepts to improve structural synthesis efficiency by alleviating excesses such as the consideration of all constraints rather than working on critical or "near" critical constraints at each stage of a iterative design process. In other words, the method generates a sequence of non-critical designs of steadily decreasing weight, funneling down the trajectory of the designs to a limited space of the *acceptable region* (or feasible region).

Perhaps the most popular SAO algorithm is the one proposed by Jones *et al.*[127]: EGO. This algorithm is used to single-objective optimization based on the Ordinary Kriging. Throughout the years, many variants of it have been proposed in the literature, including multi-objective version (e.g., ParEGO, HEGO, MEGO, etc.).

The core of any SAO algorithm is on the criterion used to choose the infill points. These points can improve locally or globally the surrogate model accuracy depending on its purpose. For example, one may wish to improve the surrogate model accuracy only locally in the region near the best solution found so far (*exploitation*), since other points in the design space are not of interest. Conversely, one may wish to use the surrogate model to better understand the design space by working on a cheap-to-evaluate function and to that end, the global accuracy (*exploration*) is an important feature.

For optimization purposes, using solely exploration-based strategies may reduce the convergence efficiency as many non-profitable areas are investigated, whilst using solely exploitation-based strategies may lead to convergence towards a deceptive optimum if the initial sampling plan does not provide good coverage of the design space, compromising the global accuracy [18, 108]. This trade-off motivates the creation of a third type of infill strategy: the *hybrid criteria*. These infill strategies strive a balance between exploitation and exploration.

Popular hybrid infill strategies include the Probability of Improvement (PI) [139], the Expected Improvement (EI) [140] and the Weighted Expected Improvement (WEI)[135]. These criteria will be discussed in the following sections, as well as the SAO algorithms and the metrics used to assess their performances.

Finally, another powerful infill strategy is the Goal Seeking (GS)[141], a one-stage approach commonly used in problems where the aim of the search if to find a specific objective value.

6.1 Probability of Improvement

The Probability of Improvement is one of earliest infill criteria and dates back in 1964 in the work of Kushner[139]. This criterion searches the point where the probability of sampling a lower value (in case of minimization) than the current best y_{min} is maximum. Realizing that $Y(\mathbf{x})$ comes from a normally distributed random variable with estimated mean $\hat{y}(\mathbf{x})$ and estimated variance $\hat{s}^2(\mathbf{x})$, then the probability of improvement upon y_{min}, denoted by $I = y_{min} - Y(\mathbf{x})$, is given by:

$$P[I(\mathbf{x})] = \begin{cases} \Phi\left(\dfrac{y_{min} - \hat{y}(\mathbf{x})}{\hat{s}(\mathbf{x})}\right) = \dfrac{1}{2}\left[1 + \text{erf}\left(\dfrac{y_{min} - \hat{y}(\mathbf{x})}{\hat{s}(\mathbf{x})\sqrt{2}}\right)\right], & \text{if } \hat{s}(\mathbf{x}) > 0 \\ 0, & \text{if } \hat{s}(\mathbf{x}) = 0 \end{cases} \tag{6.1}$$

where $\Phi(\cdot)$ is the normal cumulative distribution function. The error function (erf) is a special function widely used in statistics worth twice the integral of the Gaussian distribution with 0 mean and variance of 1/2 [142]:

$$\text{erf}(x) = \frac{2}{\sqrt{\pi}} \int_0^x \exp^{-t^2} dt \tag{6.2}$$

To illustrate this criterion, a one-dimensional unconstrained problem is used:

$$f(x) = (6x-2)^2 \sin(12x-40) \tag{6.3}$$

This is a non-linear function with one global optimum and one local minimum. A small and non-uniform sample was chosen to make clearer how the PI works.

Figure 21 – Graphical interpretation of PI for a 1D problem

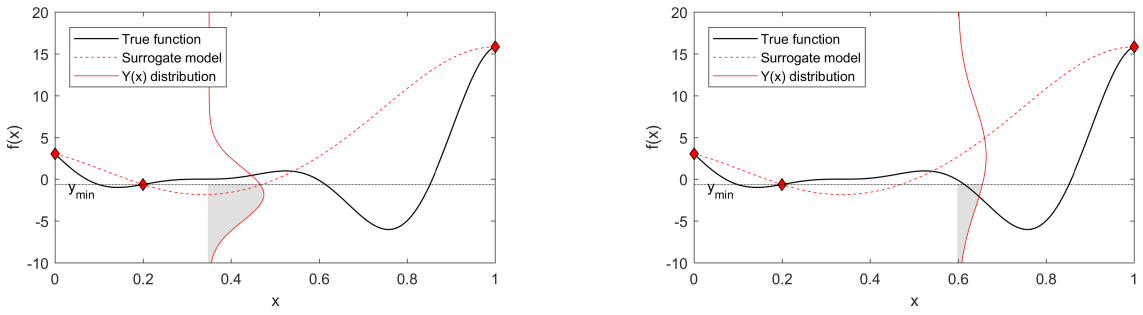

(a) $P[I(x = 0.35)]$ (b) $P[I(x = 0.60)]$

Source: the author.

In Fig. 21 (a), the $P[I(x = 0.35)]$ may be obtained by calculating the area below the horizontal line (gray) (y_{min}) enclosed by the Gaussian distribution of $Y(x = 0.35)$, which

corresponds to the value obtained by Eq. (6.1). Note that in less explored areas, the Gaussian distribution is flattened since the estimated standard deviation is, as expected, higher. The problem is that this approach may lead to an overly exploitative behaviour, in which only designs close the local optimal are preferred to those in areas less explored, which may slow down convergence in multimodal landscapes [18, 108]. This occurs because although the criterion indicates where the improvement is higher, it does not estimate how big that improvement could be.

This is even more clear in Fig. 22 (b), in which four iterations in a row suggest the addition of points very close to the current best value. Only when the region between 0.5 and 1.0 predicts lower values of $\hat{y}(x)$, the algorithm ceases the exploitation in the region between 0.4 and 0.5. Note that in the second row, the $P[I(x)]$ is the same (or very close to it) for multiple points in the design space. In this case, the choice was made at random. In any case, the algorithm continues to show a preference for the local exploration in regions of small uncertainties.

To tackle this issue, a lower y_{min} may be set [139, 116]. In practice, estimating y_{min} with confidence is not so easy and the algorithm efficiency may be compromised. If a y_{min} too small is chosen, the search will provide an excessively local search and may result in the premature stop of the SAO algorithm. On the other hand, if a y_{min} too big is considered, the algorithm will be dominated by less explored areas. Thus, the present work will deal with another alternative involving the estimation of how much improvement there would be with the addition of a given point, namely the Expected Improvement.

6.2 Expected Improvement

The Expected Improvement (EI) was proposed by Mockus *et al.*[143] and takes into account the magnitude of possible improvement on the current best value aiming at a balance between the desire to search at locations with good predicted values (exploitation) with the desire to check where the uncertainty of prediction is large (exploration). The EI concept gained popularity when Jones *et al.*[127] applied it as the infill criterion to the EGO algorithm.

Thus, instead of searching for points that will likely be better than our best solution so far as shown in the previous subsection, the EI aims to quantify how much a given point may

Figure 22 – PI search for one-dimensional problem

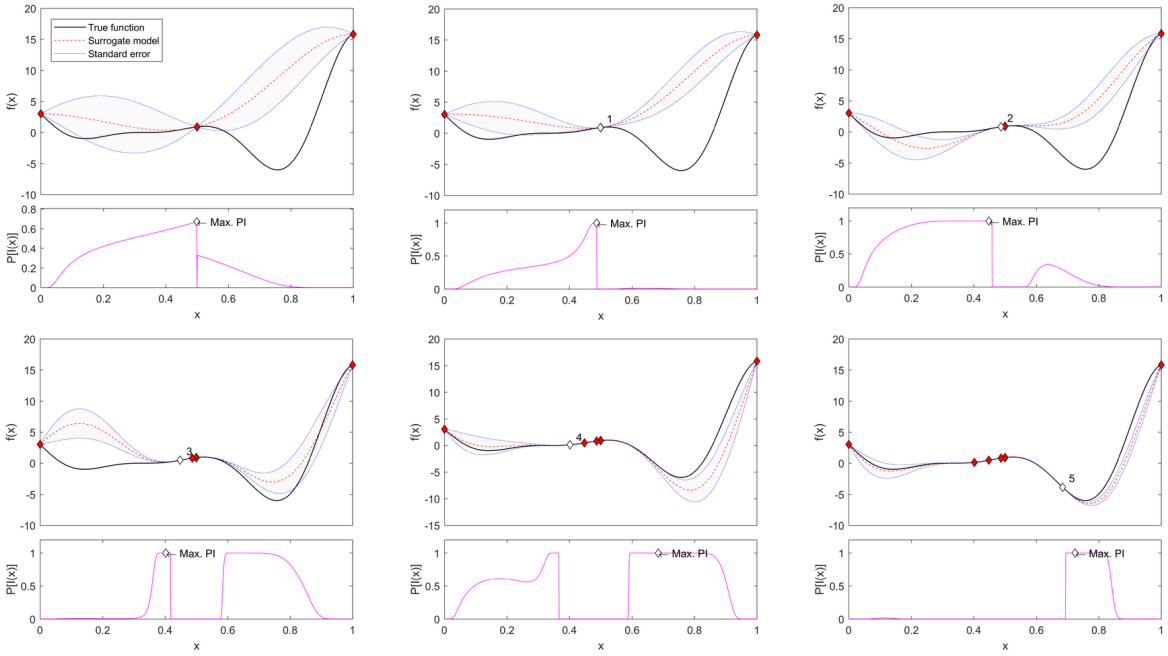

Source: the author.

improve upon y_{min} using:

$$E[I(\mathbf{x})] = \begin{cases} (y_{min} - \hat{y}(\mathbf{x}))\ \Phi\left(\dfrac{y_{min} - \hat{y}(\mathbf{x})}{\hat{s}(\mathbf{x})}\right) + \hat{s}(\mathbf{x})\ \phi\left(\dfrac{y_{min} - \hat{y}(\mathbf{x})}{\hat{s}(\mathbf{x})}\right), & \text{if } \hat{s}(\mathbf{x}) > 0. \\ 0, & \text{if } \hat{s}(\mathbf{x}) = 0. \end{cases} \tag{6.4}$$

where $\phi(\cdot)$ is the probability density function. Evaluating Eq. (6.4) using the error function (erf), we arrive at:

$$E[I(\mathbf{x})] = \begin{cases} (y_{min} - \hat{y}(\mathbf{x}))\ \left[\dfrac{1}{2} + \dfrac{1}{2}\,\mathrm{erf}\left(\dfrac{y_{min} - \hat{y}(\mathbf{x})}{\hat{s}(\mathbf{x})\sqrt{2}}\right)\right] + \hat{s}(\mathbf{x})\ \dfrac{1}{\sqrt{2\pi}}\exp\left[\dfrac{-(y_{min} - \hat{y}(\mathbf{x}))^2}{2\hat{s}(\mathbf{x})^2}\right], & \text{if } \hat{s}(\mathbf{x}) > 0 \\ 0, & \text{if} \hat{s}(\mathbf{x}) = 0 \end{cases} \tag{6.5}$$

The first term in the first equation of Eq. (6.5) corresponds to the *exploitation* contribution, where the predicted difference between the current minimum and the prediction $\hat{y}$ in $\mathbf{x}$, penalized by the probability of improvement, is computed. On the other hand, the second term corresponds to the *exploration* contribution, which provides larger values in areas where uncertainties are high (i.e., unsampled areas). Typically, y_{min} is taken as the minimum target found in previous observations [127, 116, 144], but it may also be set as a minimum value of expected value of the target [145]. In constrained problems (discussed in Section 6.14), y_{min} is the

best *feasible* solution. For further details on the development of the EI expression, the reader is encouraged to look for the reference [116].

Note that Eq. (6.5) is a differentiable function and quick to evaluate, and can, therefore, be maximized with a simple algorithm. However, care should be taken as this is often the case of a multimodal function [135]. In this work, the PSO is used to maximize the EI due to its good performance in previous works at the Laboratório de Mecânica Computacional e Visualização (LMCV) in problems with many local minima.

The EI criterion has been proved to find the global optimum [146]. However, Sóbester *et al.*[135] stress that, although the criterion offers a simple and combined form of fusing exploration and exploitation, if the problem in hand is likely to yield a simple, unimodal surface, searching the predictor will probably work better. Conversely, if the target landscape is extremely multimodal, biasing the search towards sampling in thus far unexplored areas could lead to faster convergence than the expected improvement criterion.

Figure 23 – EI search for a one-dimensional problem

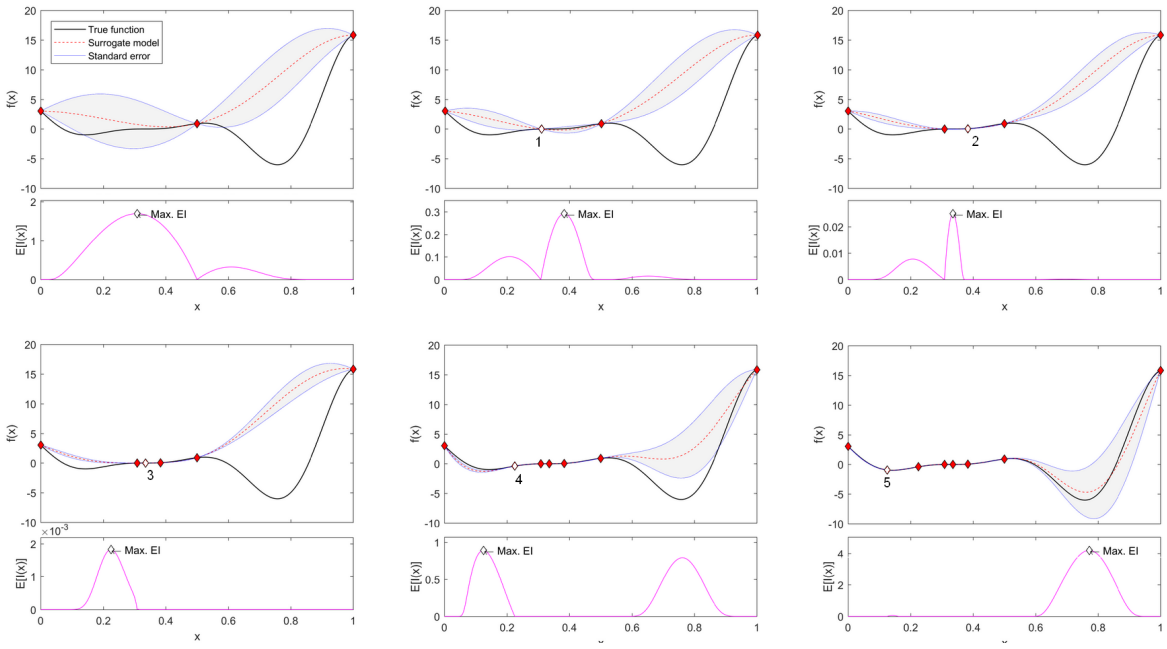

Source: the author.

To illustrate the working of this criterion, consider the same 1D problem discussed in the previous section. Note that despite the uncertainty between 0.5 and 1.0, the EI search is significantly local-driven, as shown in the first row of Fig. 23. When the third point is sampled, the EI is significantly reduced and the region not yet explored starts to show a higher variance, which results in two peaks (second figure from lower row) of almost the same magnitude. After

two deceptive "global" optimum are sampled, the high uncertainty of the area not explored starts to dominate and the algorithm finally shifts the search for a more global approach.

Thus, the following shortcomings may be associated with the EI criterion: (i) it does not allow the user to control the balance between local and global exploration and (ii) it may be heavily biased if the target is poorly estimated by the approximation (e.g., inadequate initial samples that lead to very small estimates of the standard error), with consequent poor accuracy of the EI. As a result of these issues, only points close to the current best point have high expected improvement. This will result in a fairly exhaustive search around the initial best point before the algorithm begins to search more globally [135].

To alleviate these shortcomings, several approaches have been proposed. For instance, Schonlau *et al.*[147] propose the *Generalized Expected Improvement* criterion, which introduces the parameter g ($g \geq 0$) to the basic expression $I(\mathbf{x}) = y_{min} - y(\mathbf{x})$:

$$I^g(\mathbf{x}) = \max \begin{cases} [y_{min} - y(\mathbf{x})]^g, & \text{if } y(\mathbf{x}) < y_{min} \\ 0, & \text{otherwise} \end{cases} \tag{6.6}$$

For notational simplicity, the dependence on $\mathbf{x}$ is omitted in the following derivation. Rewriting Eq. (6.6) in terms of the predicted values using $z = (y - \hat{y})/\hat{s}$ and $y^*_{min} = (y_{min} - \hat{y})/\hat{s}$:

$$I^g = \max \begin{cases} s^g [y^*_{min} - z]^g, & \text{if } z < y^*_{min} \text{ and } s > 0 \\ 0, & \text{otherwise} \end{cases} \tag{6.7}$$

Taking the expectation (for $s > 0$), we obtain:

$$E[I^g] = \hat{s}^g \sum_{k=0}^{g} (-1)^k \binom{g}{k} {y^*_{min}}^{g-k} \, T_k \tag{6.8}$$

where

$$T_k = \int_{-\infty}^{y^*_{min}} z^k \phi(z) \, dz \tag{6.9}$$

Eq. (6.9) is solved using the partial integration technique. The full derivation can be found in Schonlau *et al.*[147]. For the particular case where $g = 0$, Eq. (6.8) yields the Probability of Improvement criterion, since all terms except T_0 are equal to 0, and T_0 is defined as[147]:

$$T_0 = \int_{-\infty}^{y^*_{min}} \phi(z) \, dz = \Phi(y^*_{min}) = \Phi\left(\frac{y_{min} - \hat{y}}{\hat{s}}\right) \tag{6.10}$$

For higher values of g, the criterion shifts towards a global search. Another alternative is to use weights to bias the search for local or global searches. This approach is discussed

by Sóbester *et al.*[135] and is also investigated in this work. Other alternatives based on the EI criterion are discussed in the work of Zhan and Xing[148]. The authors provide a comprehensive review on the use of EI-based infill criteria for a wide range of expensive optimization problems.

6.3 Weighted Expected Improvement

The Weighted Expected Improvement is given by [135]:

$$WE[I(\mathbf{x})] = \begin{cases} w\ (y_{min} - \hat{y}(\mathbf{x}))\ \Phi\ \left(\dfrac{y_{min} - \hat{y}(\mathbf{x})}{\hat{s}(\mathbf{x})}\right) + (1-w)\ \hat{s}(\mathbf{x})\ \phi\ \left(\dfrac{y_{min} - \hat{y}(\mathbf{x})}{\hat{s}(\mathbf{x})}\right), & \text{if } \hat{s}(\mathbf{x}) > 0 \\ 0, & \text{if } \hat{s}(\mathbf{x}) = 0 \end{cases} \tag{6.11}$$

where w is the weighting factor between [0, 1]. The lower bound leads to a global extreme of the search scope range, while the upper bound will exploit the current best value. Sóbester *et al.*[135] suggest a cycle with 5 values of weights ($\mathbf{w} = \{0.1, 0.3, 0.5, 0.7, 0.9\}$), but warned that values of w exceeding 0.5 should only be used when one is confident that the function landscape is of low modality. In addition to that, a recent study carried out by De Ath *et al.*[108] pointed out that this procedure may lead to dominated solutions if the exploitation and exploration terms are considered the objective functions of a multiobjective optimization problem. The authors showed that for $w \in [0.185\ 0.50]$, the maximization of $WEI(\mathbf{x})$ results in solutions of the Pareto set. Thus, assuming that we do not know the true behaviour of the problem before-hand, the present work will adopt the following scheme: $\mathbf{w} = \{0.2, 0.35, 0.50\}$.

Again, the test problem discussed in Section 6.2 is used to show how the weights can affect the location of the infill point. In the first three cycles, the WEI searches provide points very close to the ones obtained by the EI due to the deceptive behaviour of the initial surrogate model. In the first search, as the sampling points are equally spaced, the variance is the same, thus, the bias inserted to lead to a more global scope is not effective and the term accounting for the local improvement dominates. In the following two iterations, when $w = 0.35$ and $w = 0.50$, respectively, the algorithm dwells in the region incorrectly predicted as a smooth function.

In the first iteration of the new cycle, the global search ($w = 0.20$) still leads to the area near sampled points, but in the following iteration ($w = 0.35$), the algorithm shifts to the unexplored area. This time, one of the two peaks with similar magnitude by the EI search (see Fig. 23) is magnified by the higher variance in the unexplored area, reaching a point only 1.5% far from the global optimum of the true function.

Figure 24 – WEI search for a one-dimensional problem

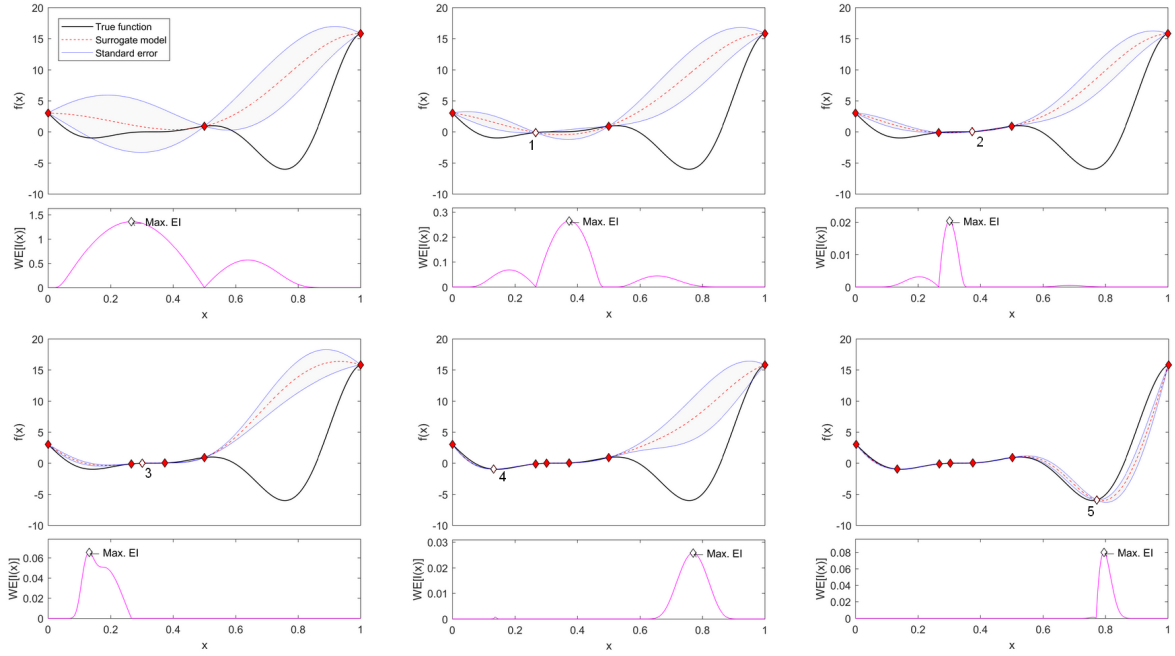

Source: the author.

It is worth noting that the performance of WEI is very sensitive to the initial surrogate model (initial sampling plan, hyperparameters, etc.) and the superior performance of this approach is not a rule.

6.4 Constraint handling

When dealing with constraints, the designer must seek for feasible solutions to improve the optimal search. This is a simple task if the constraints are evaluated exactly, but a much complex problem if they are also calculated using surrogate models. In the first scenario, the algorithm simply sets the expected improvement of points that violate the constraint to 0, preventing the exploration of unfeasible areas, otherwise, the expected improvement value is kept as discussed in previous sections.

On the other hand, if a constraint is evaluated using a surrogate model, a level of uncertainty is added to the problem. This derives from the fact that if the constraint violation is a prediction, there is a possibility that an unfeasible design predicted by the surrogate model is, in fact, a feasible design. To somehow take into account this uncertainty into the EI calculation, especially critical near the constraint threshold, Forrester *et al.*[18] discuss two approaches: the Expected Improvement with Simple Penalty Function and the Constrained

Expected Improvement.

The first is a simple and straightforward way to prevent further exploration of regions predicted to be unfeasible without removing these points from the construction of the expectation. This is done by adding a penalty factor (P) to the EI evaluation as in $E[I(\mathbf{x})] = E[I(\mathbf{x})] - P$. However, despite the simplicity of implementation, this approach falls into the pitfalls discussed before.

The Constrained Expected Improvement is a fully probabilistic approach where the uncertainty (variance) is taken into account to penalize the expected improvement of a given point. This is done by considering the Probability of Feasibility (PF) of that point, which may be described by:

$$P[F(\mathbf{x})] = \begin{cases} \frac{1}{2} + \frac{1}{2}\,\mathrm{erf}(\frac{g_{min} - \hat{g}(\mathbf{x})}{\hat{s}(\mathbf{x})}), & \text{if } \hat{s}(\mathbf{x}) > 0 \\ 0, & \text{if } \hat{s}(\mathbf{x}) = 0 \text{ and } \hat{g}(\mathbf{x}) > 0 \\ 1, & \text{if } \hat{s}(\mathbf{x}) = 0 \text{ and } \hat{g}(\mathbf{x}) < 0 \end{cases} \tag{6.12}$$

where g_{min} refers to the constraint limit, taken as 0 since all constraints are normalized as $g_j(\mathbf{x}) \leq 0$. Note that g_{min} is the maximum value that the constraint may assume. This way, a tolerance may be considered in order not to discard designs near the feasibility threshold.

More recently, Tutum *et al.*[128] proposed a modification to this approach as follows:

$$P[F(\mathbf{x})] = \begin{cases} \frac{1}{2} + \frac{1}{2}\,\mathrm{erf}(\frac{g_{min} - \hat{g}(\mathbf{x})}{\hat{s}(\mathbf{x})}), & \text{if } \mathrm{erf}(\frac{g_{min} - \hat{g}(\mathbf{x})}{\hat{s}(\mathbf{x})}) \geq 1 \\ 2 - \mathrm{erf}(\frac{g_{min} - \hat{g}(\mathbf{x})}{\hat{s}(\mathbf{x})}), & \text{if } 0 \leq \mathrm{erf}(\frac{g_{min} - \hat{g}(\mathbf{x})}{\hat{s}(\mathbf{x})}) < 1 \\ 0, & \text{otherwise} \end{cases} \tag{6.13}$$

Note that if all constraints are satisfied and $\hat{s}(\mathbf{x})$ is relatively low, it results in $PF = 1$. For the specific case where at least one of the constraint values is close to the threshold, the 2^{nd} condition results in a value greater than one, emphasizing near-boundary solutions. Finally, when the constraint prediction is violated, its PF is set to 0.

As these are uncorrelated processes, we multiply the EI by the PF to obtain the Constrained Expected Improvement (CEI)[18]:

$$E[I_c(\mathbf{x})] = E[I(\mathbf{x}) \cap F(\mathbf{x})] = E[I(\mathbf{x})] \cdot P[F(\mathbf{x})] \tag{6.14}$$

In this work, the modification proposed by Tutum *et al.*[128] is adopted. In addition to that, when the objective function is a cheap-to-run function and the constraints are approximated

by surrogate models, the following script is used: 1) for each trial **x**, evaluate the objective function and compare it to y_{min}, 2) if the new point is better than the current best feasible solution, the CEI is the difference between them multiplied by the PF of that point or 3) else, the improvement is set to 0 regardless of its feasibility.

6.5 Sequential Approximate Optimization Algorithms

In this work, four frameworks are investigated. Each framework is either named after the combination of the surrogate model used plus the correlation function employed to the definition of the model hyperparameters or simply by the width-defining method. In addition to that, to better understand the effect of the weights on the EI search, all frameworks will be tested and compared considering both infill criteria (EI and WEI).

The frameworks will be discussed in detail in the following sections, but can be briefly summarized as follows:

1. **KRG-G**: This method is based on the implementation of the EGO algorithm proposed by Jones *et al.*[127] and also uses a Gaussian function as the correlation function. However, the present work differs from it on the constraint handling, the optimization algorithm used to maximize the infill criterion and the MLE, and the stopping criteria;
2. **KRG-M**: This method is the same as KRG-G, but the correlation function is the Matérn 5/2.
3. **5-FCV**: This method is based on the work of Sóbester *et al.*[135] and uses the k-Fold CV (with $k = 5$) to define the RBF widths;
4. **ASKIT**: This method is the same as the 5-FCV, but instead of evaluating the widths using a CV technique, the expression and the adaptive scaling technique proposed by Kitayama *et al.*[131] is applied.

In all four approaches, two stopping criteria are considered: maximum number of HF evaluations or maximum number of iterations without improvement ($StallGen$). Both criteria are also considered to the traditional optimization using the HFM.

In principle, the EGO algorithm uses the EI both as infill and stopping criteria, the latter being triggered when the highest EI found at a given iteration is less than 1% of the current best solution [127]. However, for constrained problems, this is an insufficient criterion since the EI of unfeasible designs is often set to 0. This way, the more the design space (or design criterion) is cut out by complex or multiple constraints, the higher is the probability of the EI search results

in unfeasible designs, terminating the algorithm and preventing further exploration of feasible areas in the following iterations. In addition to that, a deceptive approximate surface may lead to unrealistic values of EI and premature "convergence".

The SAO-RBFs were originally implemented by Balreira[149] on BIOS. Later on, the EI criterion, as well as other width-defining methods, were implemented by Ribeiro *et al.*[50] for the RBF-based algorithms. In short, BIOS is an open-source program written in C++ language developed by the LMCV collaborators [96]. Several optimization algorithms are available in this software, including PSO and its modified version for laminated composite problems (see Section 4.1). Likewise, an in-house software named FAST, also developed by LMCV, is used to carry-out the HF analyses. Both softwares use the Object-Oriented Programming (OOP) paradigm and are connected through input and output text files.

6.5.1 SAO using Kriging

As mentioned, a variation of the EGO algorithm is employed. Fig. 25 depicts the working of it. The algorithm starts with the generation of the initial sampling plan using DoE and the evaluation of sampling points by the HFM. Next, PSO is used to maximize the MLE considering all sampling points according to the mathematical formulation in Eq. (5.13). Then, the LOOCV is applied to validate the fitted Kriging model. The CV procedure is done a bit differently than the usual procedure of re-estimating hyperparameters for each reduced sample due to the optimization process involved in the maximization of the MLE.

Re-estimating the hyperparameters n times for very similar samples (if no major outliers or very few data is used) would be time-consuming, especially for large samples. According to Jones *et al.*[127], dropping a single observation has a negligible effect on the maximum likelihood estimates and the hyperparameters found considering all sampling points may be used, simplifying the process.

In practice, only the correlation matrix Ψ and the $\mathbf{Y}$ vector must be re-computed from one sampling point removal to another. To assess the accuracy of the prediction made without the sampling point $\mathbf{x}^{(i)}$, say $\hat{y}(\mathbf{x}^{(i)})$, a metric named “standardized cross-validated residual” is calculated:

$$STD_{CVerror} = \frac{y(\mathbf{x}^{(i)}) - \hat{y}(\mathbf{x}^{(i)})}{\hat{s}(\mathbf{x}^{(i)})} \tag{6.15}$$

where $\hat{s}(\mathbf{x}^{(i)})$ is calculated as shown in Eq. (5.16). This value represents the number of standard

Figure 25 – SAO using Kriging

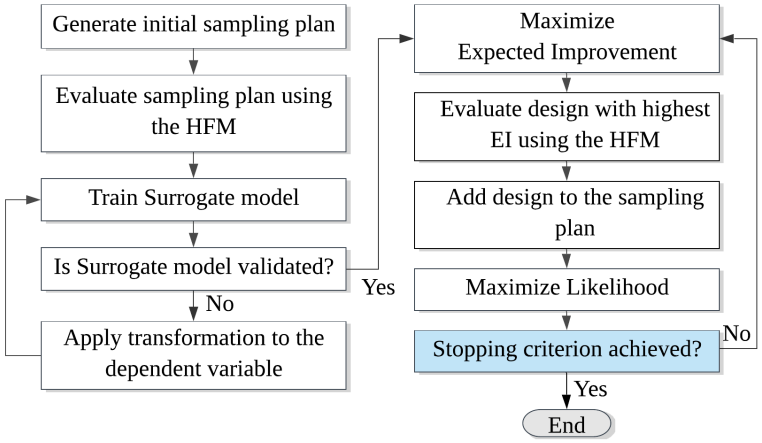

Source: the author.

deviations that the actual value of $y(\mathbf{x}^{(i)})$ is from the surrogate model prediction. This procedure is repeated for all n sampling points and in all times, the error should be roughly in the interval [-3, 3] to validate the Kriging model. In case of failure of model validation, Jones *et al.*[127] suggest a transformation of the dependent variable. Typically, the log transformation ($\log(y)$ or $\ln(y)$) or the inverse transformation ($-1/y$) are used. This approach is also adopted in this work when there is failure in the model fitting. If model validation still fails, one may reconsider the kernel used or increase the sampling plan size.

After model validation, the algorithm proceeds to its main loop, which consists of the maximization of the infill criterion using the PSO. The design with the highest EI (or WEI) is evaluated using the HFM and added to the sample. Next, the Kriging hyperparameters are re-estimated by the maximization of the MLE. This process is repeated until at least one stopping criterion is achieved.

6.5.2 SAO using RBF

The SAO algorithms using RBF are a simplified version of the one discussed in Section 6.5.1, as depicted in Fig. 26. The basic difference consists in the training of the initial surrogate model. The RBF widths are defined using either the closed-form expression shown in Eq. (5.27) or the k-Fold CV, as illustrated in Fig. 20.

After that, the algorithms initiate the main loop, where the PSO is used to maximize the infill criterion and find the new infill point, which should be added to the sample with its respective HF response. Then, the surrogate model must be updated with the new widths. Note

Figure 26 – SAO using RBF

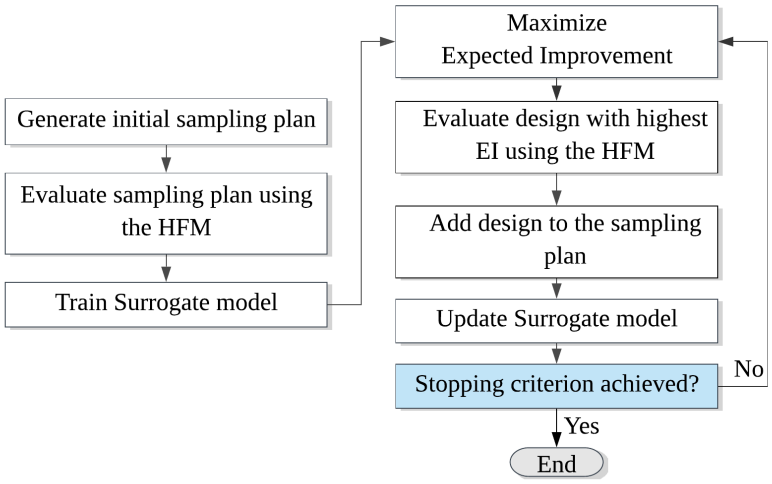

Source: the author.

that the validation step in Fig. 25 is skipped and only one optimization loop is needed since the hyperparameter estimation is no longer an optimization problem.

6.6 Fitness assessment

For the assessment of the performance of the SAO algorithms, the following aspects and metrics are considered:

a) accuracy: measures how close the surrogate model optimum is to the true function optimum. In this work, the average Normalized Root Mean Squared Error (NRMSE) is used;

b) efficiency: measures the extent to which time is employed to produce reasonable results at the lowest amount of resource possible. Two metrics are considered: the speed-up and number of HF evaluations required to achieve at least one of the stopping criteria, including the initial sampling plan observations;

c) robustness: measures the ability of the model to consistently present good results in different runs. To that end, the standard deviation of NRMSE is calculated.

The NRMSE is given by:

$$NRMSE = \sqrt{\frac{\sum_{i=1}^{n_v}(y_{OPT} - y_{SAO})^2}{\sum_{i=1}^{n_v}(y_{OPT})^2}} \tag{6.16}$$

where n_v is the number of validation points, y_{OPT} is the HF response of the reference solution (i.e., optimal solution) and y_{SAO} is the best response obtained by the SAO evaluated by the HFM. This metric is evaluated for each optimization and averaged by the number of runs, which gives

$\overline{NRMSE}$. Lower values of $\overline{NRMSE}$ indicate better performances.

To assess the efficiency, two metrics are evaluated: the speed-up and the number of HF evaluations needed to reach at least one stopping criterion. The speed-up is given by:

$$\text{Speed-up} = \frac{1}{n_r} \sum_{i=1}^{n_r} \frac{T_{HFM}}{T_{SAO,i}} \tag{6.17}$$

where n_r is the number of runs, T_{HFM} is the average time spent in the conventional optimization using the HFM and $T_{SAO,i}$ is the time spent using a SAO algorithm on the i-th run. Both measured by the wall-clock time.

Finally, the standard deviation of the NRMSE (STD_{NRMSE}) is given by:

$$STD_{NRMSE} = \sqrt{\frac{\sum_{i=1}^{n_r} NRMSE_i - \overline{NRMSE}}{n_r - 1}} \tag{6.18}$$

Again, smaller STD_{NRMSE} values suggest a more robust SAO or to put it another way, the less variable the results are. Of course, this metric should be read in context with the SAO accuracy.

7 NUMERICAL EXAMPLES AND DISCUSSION

This chapter presents the results for applications of the SAO algorithms in two topics: 1) FGM problems and 2) laminated composite problems. In all cases, the hyperparameter p_j in Kriging is fixed and equal to 2.0 so that the optimization problem involving the maximization of the MLE is simplified to the search of θ.

A comparative study is carried out considering 8 combinations of surrogate models, basis functions and infill criteria (EI and WEI). These methods are identified as shown in Table 2 in the remainder of this work.

Table 2 – Description of SAO algorithms

Acronym	Surrogate model	Basis/correlation function
KRG-G	Kriging	Gaussian (MLE)
KRG-M	Kriging	Matérn (MLE)
5-FCV	RBF	Gaussian (k-Fold (with k = 5))
ASKIT	RBF	Gaussian (Closed-form expression by Kitayama *et al.*[131])

Source: the author.

The stopping criteria are the maximum number of iterations, which should be specified for each problem, and the maximum number of SAO iterations without improvement on the best solution (*StallGen*).

Unless stated otherwise, $n_r = 10$ runs will be carried out for each problem and the initial surrogate model is built using only $n = 5m$ sampling points. The performance of the SAO algorithms is assessed using the metrics discussed in Section 6.6: the average number of points evaluated until the algorithm is stopped ($\overline{n}_p$), the $\overline{NRMSE}$, the standard deviation of the $\overline{NRMSE}$ and the speed-up.

All simulations are carried out on a computer running on an Intel i9-9820 X @ 3.30 GHz, 10 cores and 120 GB RAM. If not specified, no parallelization procedure is adopted.

7.1 FGM problems

In this section, for each optimization, a new distribution of the sampling plan is created using the LHS_{20} approach. If not specified, the values of the optimization parameters considered in the following examples are the ones shown in Table 3. It is worth emphasizing that the *StallGen* values of the maximization of the EI, WEI, or MLE are higher because these are cheap functions. The SAO algorithm itself stops when the best solution is not improved for 10

iterations, which is also adopted for the HF optimization.

Table 3 – FGM problems: optimization parameters

Parameter	Conventional Opt.	Max. of EI or WEI	Max. of MLE
Topology	Global	Global	Global
Swarm size (N_p)	50	250	100
Maximum Iterations (It_{max})	100	100	100
$StallGen$	10	25	25
p_{mut}	0.02	0.02	0.05
w	0.7	0.7	0.7
c_1	1.5	1.5	1.5
c_2	1.5	1.5	1.5

Source: the author.

Before proceeding to the optimization examples, a study is carried out to assess the accuracy of the isogeometric meshes used in the following problems.

7.1.1 Validation

The first verification regards the free-vibration analysis. For the validation of the structural analysis of the FG plates, a mesh of 16x16 cubic NURBS elements for the full representation of the plate was used. The stiffness, constitutive and mass matrices were integrated using the Gauss quadrature. Full integration was used in the element mid-surface and 10 Gauss points were used for the through-thickness integration. This integration scheme provides a natural frequency closer to the reference values than using the reduced integration scheme. The boundary conditions of the simply supported square plate are depicted in Fig. 27.

Figure 27 – Boundary conditions of simply supported plate

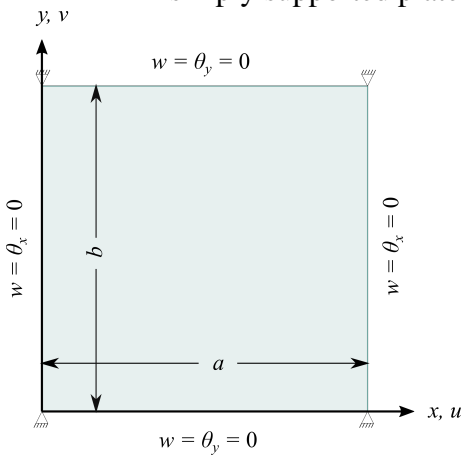

Source: the author.

The non-dimensional natural frequency is calculated as follows:

$$\overline{\omega} = \omega\, h\sqrt{\rho_c/G_c} \tag{7.1}$$

where $G_c = E_c/[2\,(1+\nu_c)]$. For validating the Mori-Tanaka method, a plate of SUS304/Si_3N_4 with $a/h = 10$ is considered. The material properties are shown in Table 4.

Table 4 – Material properties of FG SUS304/Si_3N_4

Material	E (Pa)	ν	ρ (kg/m^3)
SUS3O4	201.04×10^9	0.30	8166
Si_3O_4	348.43×10^9	0.30	2370

Source: Adapted from Do *et al.*[48].

The volume fraction is given by the Power-law function and the results are compared to those found by Do *et al.*[48], as shown in Table 5. The maximum difference found is below 1%, which suggests that the present mesh is sufficiently accurate to model the structural responses even of thick plates.

Table 5 – Non-dimensional natural frequency of simply supported SUS3O4/Si_3N_4 FG square plate

p	1	2	5	10
Do *et al.*[48]	0.0542	0.0485	0.0440	0.0419
Present work	0.0546	0.0488	0.0440	0.0417
Difference (%)	0.71	0.63	0.02	0.57

Source: the author.

For validating the Voigt model, the HF responses for different combinations of Power-law index and thickness found in Franco *et al.*[150] are reproduced. The plate is also made of Stainless Steel (SUS3O4) and Silicon Nitride (Si_3N_4), but this time the temperature effect is considered using the Toulokian equation. The temperature is said to be constant (T = 300 K) from the bottom to the top of the plate. The temperature-dependent coefficients are shown in Table 6. The normalization of the natural frequency was not applied in this case. Again, the results presented in Table 7 show excellent agreement between the present work and the reference values.

Next, a clamped square plate with a circular hole in its centre is modelled using a mesh with 8 patches, each of them with a 8x8 mesh of cubic elements, adding up to a total of 512 elements, as shown in Fig. 28 (a). The boundary and loading conditions are depicted

Table 6 – Temperature-dependent coefficients for $SS3O_4/Si_3N_4$ FGM

Material	Property	P_0	P_{-1}	P_1	P_2	P_3
Silicon Nitride (Si_3N_4)	E (Pa)	348.43×10^9	0	-3.070×10^{-4}	2.160×10^{-7}	-8.946×10^{-11}
	ν	0.24	0	0	0	0
	ρ (kg/m^3)	2370	0	0	0	0
Stainless Steel (SUS3O4)	E (Pa)	201.04×10^9	0	3.079×10^{-4}	-6.534×10^{-7}	0
	ν	0.3262	0	-2.002×10^{-4}	3.797×10^{-7}	0
	ρ (kg/m^3)	8166	0	0	0	0

Source: the author.

Table 7 – Natural frequency of simply supported $SUS3O4/Si_3N_4$ FG square plate

p	0.20	1.00	4.0	10.0
h (mm)	36.4	35.0	34.3	60.0
a/h	13.74	14.29	14.49	8.33
Franco *et al.*[150]	7982.20	5760.81	4718.51	7478.13
Present work	7976.49	5769.94	4726.05	7477.69
Difference (%)	0.07	0.12	0.16	0.01

Source: the author.

in Fig. 28 (b). The geometry of the plate is given by $a = b = 0.72$ m, $h = a/100$, $r = a/10$ and $N_x = 1$ kN/m. The critical buckling load is normalized using $\overline{\lambda}_{cr} = \dfrac{\lambda_{cr}\, a^2}{E_c\, h^3}$. The material properties are taken from Auad *et al.*[69]: $E_c = 380 \times 10^9$ Pa (ceramic), $E_m = 70 \times 10^9$ Pa (metal) and $\nu_c = \nu_m = 0.30$.

Figure 28 – Mesh and boundary conditions for square plate with circular hole

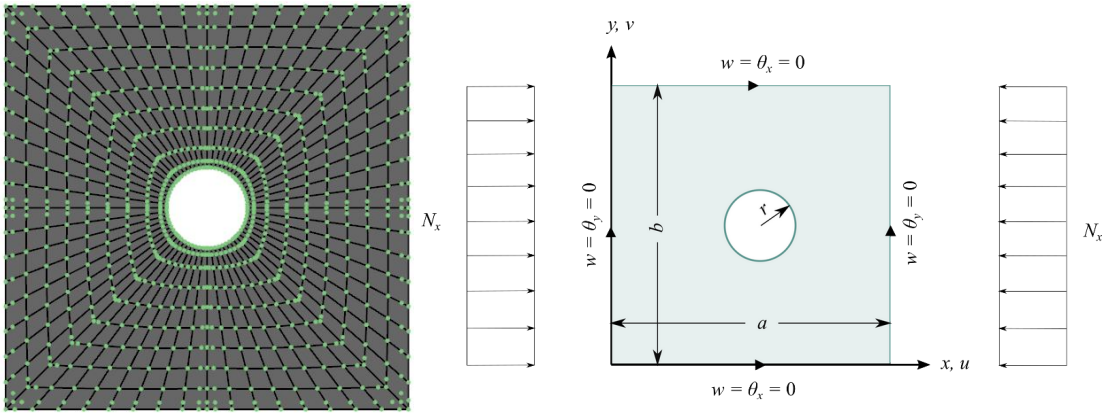

(a) Isogeometric mesh

(b) Loading and boundary conditions

Source: the author.

The volume fraction is described by a Power-law function and the effective properties are evaluated using the Voigt's model. The results obtained in the present work are compared to those obtained by the FEA software Abaqus[151] considering the same mesh refinement, but with quadractic elements with reduced integration, known as S8R. In Fig. 29, these results are

referred as FEM and the ones obtained by FAST are referred as IGA. It can be observed that the critical buckling load obtained by solving the buckling eigenvalue problem decreases as the power-law exponent increases and the amount of ceramic is reduced. It is also noticeable that the agreement between IGA and FEM is affected. This can be partially explained by the pre-buckling displacements caused by the coupling of membrane-bending. In symmetric or isotropic distributions this difference is close to 0.

Figure 29 – Normalized buckling load factor for different exponents

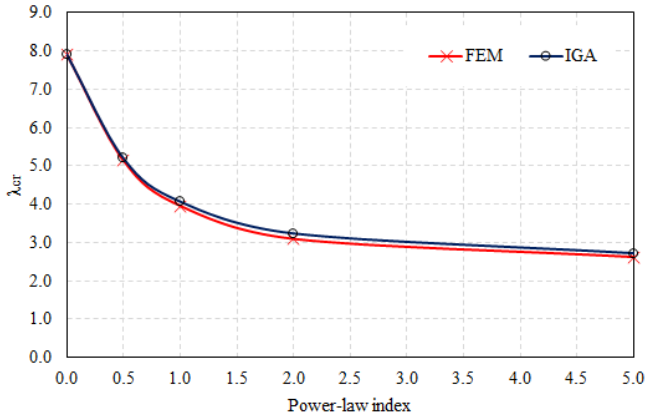

Source: the author.

Finally, to validate the mesh used to model the hinged shallow shell, the results of the non-linear analysis carried out by Kim *et al.*[152] are considered. The boundary conditions are depicted in Fig. 30 and the material properties are presented in Table 8. The volume fraction distribution is described by the Sigmoid function and the effective properties are given by the Voigt model. The displacement x load curve for two values of p and for the isotropic case are shown in Fig 31. Good agreement is observed between the reference results and the displacements obtained by FAST.

Table 8 – Material properties for validation of shallow shell mesh

Material	E (Pa)	ν	ρ (kg/m^3)
Zr	151×10^9	0.30	3000
Al	70×10^9	0.30	2707
Isotropic	3103×10^6	0.30	3000

Source: the author.

Figure 30 – Boundary conditions of hinged cylindrical shell

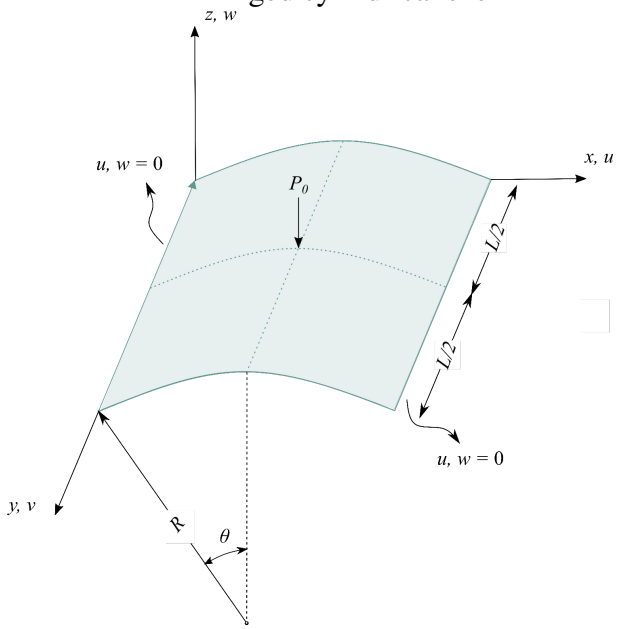

Source: the author.

Figure 31 – Deflection vs Point Load for different types of materials

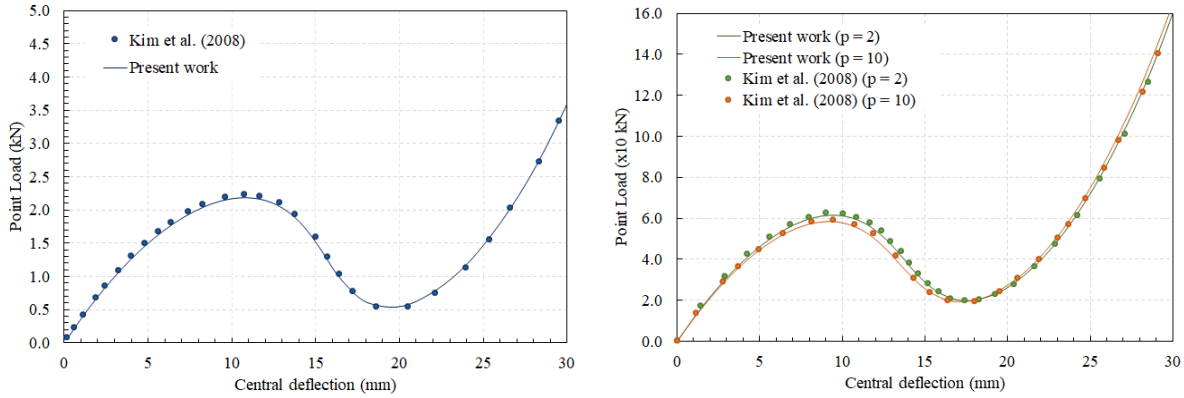

(a) Isotropic (b) FGM

Source: the author.

7.1.2 Simply Supported Plate - Vibration with frequency constraint

The first optimization problem deals with the maximization of the first natural frequency (ω) of a simply supported square plate studied by Franco *et al.*[150]. The problem has two constraints on the natural frequency range. Therefore, an additional stopping criterion is considered: the algorithm is stopped whenever the best solution found so far is higher than 7999 rad/s, which is only 0.01% smaller than the maximum natural frequency allowed. This is done because the value of the maximum objective function is known and further exploration of solutions within this tolerance may be a waste of computational effort. The mathematical

formulation may be expressed by:

$$\begin{array}{ll} \text{Find} & \mathbf{x} = \{h,\ p\} \\ \text{that maximizes} & \omega(\mathbf{x}) \\ \text{subjected to} & 3000 \leq \omega \leq 8000 \text{ (rad/s)} \\ \text{with} & 0.005 \leq h \leq 0.060 \text{ (m)} \\ & 0.20 \leq p \leq 10.0 \end{array} \tag{7.2}$$

The constituents are Silicon Nitride (Si_3N_4) as the ceramic and Stainless Steel as metal (SUS3O4) in constant temperature at 300 K for both sides of the plate (see Table 6 for the material properties). The geometry of the plate is given by $a = b = 0.5$ m and $It_{max} = 50$.

In this problem, both objective function and the constraints are approximated by surrogate models. Therefore, the feasibility of a trial design is assessed using the Probability of Feasibility approach. Since the constraints are actually imposed on the response surface of the objective function, the hyperparameters are calculated only once for the objective function approximation and repeated to the constraints. The performance of the SAO algorithms is described in Table 9.

Table 9 – Metrics for SUS3O4/Si_3N_4 FG plate

Infill criterion	Surrogate model	$\overline{n}_p$	$\overline{NRMSE}$	STD_{NRMSE}	Speed-up
EI	KRG-G	27	**0.02**%	**0.03**%	32
	KRG-M	**26**	0.15%	0.36%	28
	5-FCV	28	0.21%	0.24%	38
	ASKIT	26	2.27%	1.22%	**42**
WEI	KRG-G	**25**	0.35%	0.65%	37
	KRG-M	28	**0.19**%	**0.33**%	19
	5-FCV	30	0.79%	1.11%	34
	ASKIT	26	2.12%	1.86 %	**41**

Source: the author.

Note that in all cases, the Kriging-based SAOs provided the highest robustness and accuracy, and the lowest number of points until convergence. This helps these algorithms to be as competitive as the ones based on RBF in terms of computational efficiency. In general, the EI criterion led to the best performances, with the 5-FCV being the most accurate between the RBFs. Despite the significant differences in the computational cost of the Matérn 5/2 compared to the Gaussian function, both correlation functions provided accurate results regarding both infill criteria.

The best design found using both the HFM and the SAO algorithms are compared to those obtained by Franco *et al.*[150] and Moita *et al.*[57], as shown in Table 10. It is understood

that the best SAO performance is the one with the highest accuracy (i.e., lowest $\overline{NRMSE}$). In this particular case, the best optimization was obtained using KRG-G and EI as the infill criterion. If the algorithms had the same accuracy, then we would use the following sequence to define the best performance: highest robustness (i.e., lowest STD_{NRMSE}), lowest number of HF evaluations and highest speed-up.

Table 10 – Optimal designs for SUS3O4/Si_3N_4 FG plate

	Moita *et al.*[57]	Franco *et al.*[150]	HF	SAO
p	3.80	3.40	3.37	4.01
h (mm)	59.5	59.1	58.9	60.0
ω (rad/s)	8000	8000	8000	8000
$\overline{N}_{iter}$	-	-	16	17
$\overline{N}_p$	-	-	825	27
Average time	-	-	1909 s	66 s

Source: the author.

Note that different combinations of p and h provide the highest natural frequency allowed of 8000 rad/s. This can be observed when the constraints are plotted on the response surface, as shown in Fig. 32 (d). Any response lying on the boundary between the approximate surface and the upper hyperplane is optimal. In addition to that, the initial ln-likelihood landscape of one of the optimizations using KRG-G WEI is shown in Fig. 32 (a). The landscape of this function is multimodal and the optimum hyperparameters indicate that the power-law index is more active than the plate thickness regarding the natural frequency. After 9 updates, the KRG-WEI finds an optimal design. The approximate surface is more accurate in the region of interest, as shown in Fig. 32 (c).

Fig. 33 illustrates the WEI surface for the initial surrogate model shown in Fig. 32 (b). Note that the Probability of Feasibility amplifies the EI of points near the constraint threshold and drives it to 0 where there is low likelihood of feasibility. As more points are added to the sample, the shape of the intersection between the response surface and the constraint imposed by the maximum frequency gets closer to the one observed on the HF surface.

7.1.3 Simply Supported Plate - Vibration with volume constraint

In this subsection, a free-vibration problem found in Do *et al.*[48] is discussed. The problem consists of the maximization of the normalized first natural frequency of a FG square plate ($\overline{\omega}$) subjected to a constraint on the maximum volume of ceramic material. The volume fraction is described by 13 control points symmetric about the midplane, which results in 7

Figure 32 – Surrogate model surface for SUS3O4/Si_3N_4 FG plate problem

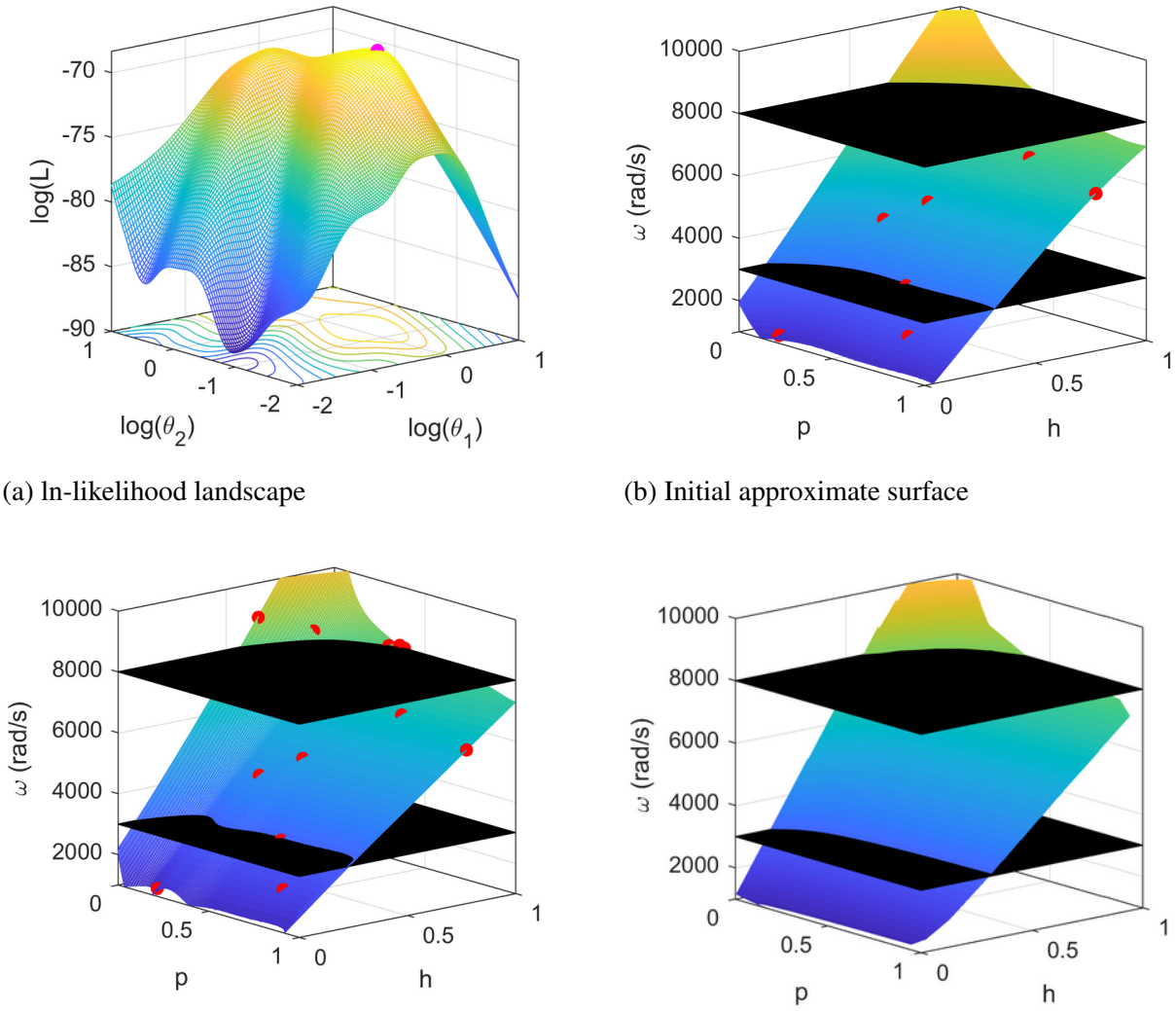

(a) ln-likelihood landscape

(b) Initial approximate surface

(c) After 9 iterations

(d) HF response surface

Source: the author.

design variables. The problem may be expressed by:

$$\begin{array}{ll} \text{Find} & \mathbf{x} = \{V_{c_i}\} \text{ for i = 1, 2, ..., 7} \\ \text{that maximizes} & \overline{\omega}(\mathbf{x}) \\ \text{subjected to} & \overline{V}_c(\mathbf{x}) \leq \overline{V}_{c,max} \\ \text{with} & 0.0 \leq V_{c_i} \leq 1.0 \end{array} \tag{7.3}$$

where V_{c_i} is the volume fraction at the i-th control point, $\overline{V}_c$ is the percentage of ceramic material and $\overline{V}_{c,max}$ is the maximum ceramic volume fraction. Three values of $\overline{V}_{c,max}$ were considered: 35%, 50% and 65%. The ceramic volume fraction of a design is given by:

$$\overline{V}_c(\mathbf{x}) = \frac{1}{h}\int_{-h/2}^{h/2} V_c \, dz \tag{7.4}$$

Figure 33 – Iterations of WEI search on constrained FG plate problem using KRG-G

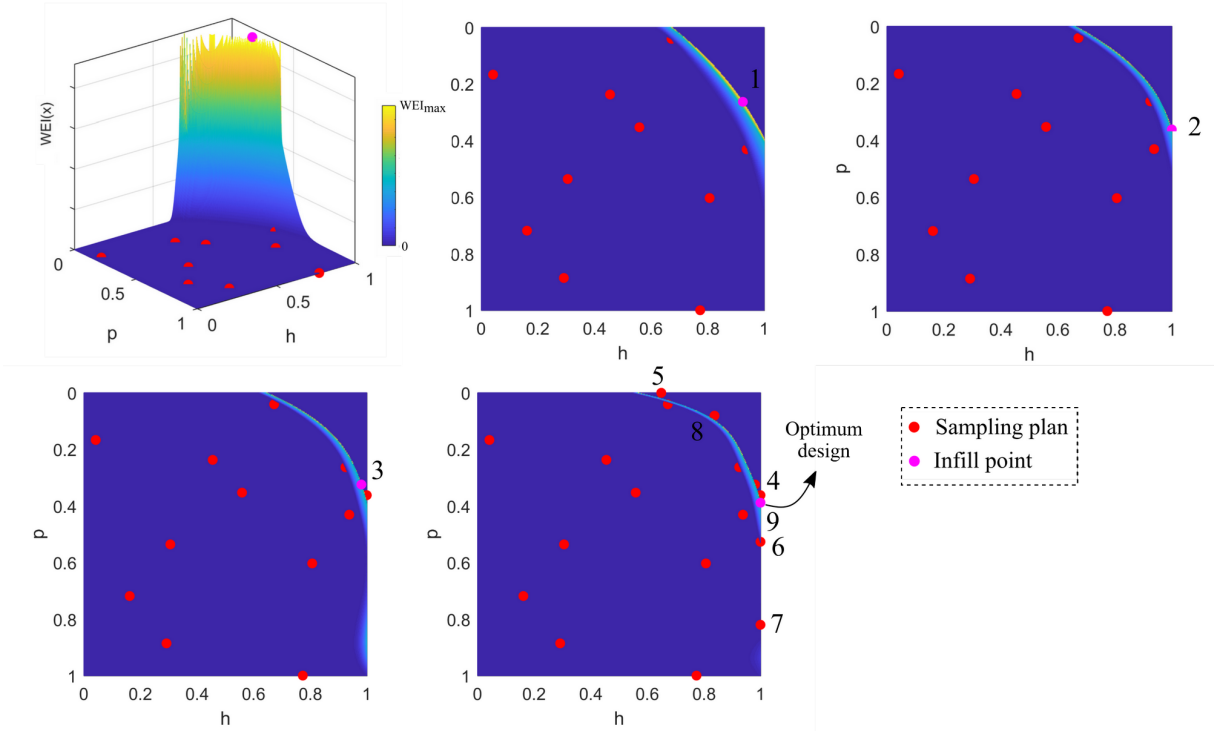

Source: the author.

This integral is evaluated using Gaussian quadrature with 10 points and is exactly calculated for all designs explored by the EI (or WEI) maximization. Therefore, only the objective function is approximated. The constituents are the SUS3O4 as the metal and $Si3N_4$ as the ceramic (see Table 4). The geometry and the boundary conditions are the same as shown in Fig. 27 for $a/h = 10$. The performance of the SAO algorithms are described in Table 11.

In all cases, the Kriging-based algorithms found the optimum solution in the first or second iteration using either EI or WEI criteria. It is also noticeable the higher cost of evaluating the Matérn correlation function with respect to the use of a Gaussian function. For example, when $V_{c,max} = 35\%$, for the same average number of HF evaluations ($\overline{n}_p$ = 47), the Gaussian function provided a much faster optimization process. While the Gaussian correlation function reached the speed-up of 34, the Matérn 5/2 function was only 23 times faster than the conventional optimization.

Overall, when it comes to the computational cost, RBF is by far the most recommended model. In this example, the 5-FCV was the most accurate and fastest width-defining method. However, it is worth mentioning that despite the excellent performance of the RBF-based SAOs, the Kriging-based algorithms managed to find the optimum design with a lower number of HF evaluations.

Table 11 – Metrics for SUS3O4/Si_3N_4 FG plate with volume constraint

$\overline{V}_{c,max}$	Infill criterion	Surrogate model	$\overline{n}_p$	$\overline{NRMSE}$	STD_{NRMSE}	Speed-up
35%	EI	KRG-G	**47**	**0.00**%	**0.00**%	34
		KRG-M	**47**	**0.00**%	**0.00**%	23
		5-FCV	49	0.12%	0.38%	**50**
		ASKIT	70	1.80%	1.17%	28
	WEI	KRG-G	**46**	**0.00**%	**0.00**%	34
		KRG-M	47	**0.00**%	**0.00**%	24
		5-FCV	50	**0.00** %	**0.00**%	**49**
		ASKIT	67	2.46%	1.65%	30
50%	EI	KRG-G	**46**	**0.00**%	**0.00**%	28
		KRG-M	47	**0.00**%	**0.00**%	18
		5-FCV	49	**0.00**%	**0.00**%	**41**
		ASKIT	72	1.51%	1.46%	22
	WEI	KRG-G	**46**	**0.00**%	**0.00**%	28
		KRG-M	**46**	**0.00**%	**0.00**%	19
		5-FCV	52	0.92%	2.92%	**37**
		ASKIT	75	1.07%	1.43%	21
65%	EI	KRG-G	**46**	0.04%	0.12%	28
		KRG-M	48	**0.00**%	**0.00**%	18
		5-FCV	50	1.17%	3.24%	**39**
		ASKIT	79	0.38%	0.45%	20
	WEI	KRG-G	**47**	**0.00**%	0.01%	28
		KRG-M	**47**	**0.00**%	**0.00**%	20
		5-FCV	50	**0.00**%	**0.00**%	**40**
		ASKIT	76	0.65%	1.37%	21

Source: the author.

Finally, the best designs for each $\overline{V}_{c,max}$ are shown in Table 12 along with the designs found by Do *et al.*[48] using a Deep Neural Network (DNN). The authors considered 10000 sampling points for the training and testing of the DNN. This large number of sampling points emphasizes the importance of SAO techniques in reducing the number of HF evaluations. Instead of working on an accurate and fixed surrogate model throughout the entire design space, the SAO algorithm improves the accuracy only in regions of interest.

The SAO results in Table 12 refer to the KRG-G WEI, KRG-G EI and KRG-M WEI approaches for the $\overline{V}_{c,max} = 35\%,\ 50\%$ and 65%, respectively. The optimal volume fraction distributions are depicted in Fig. 34. As the maximum ceramic volume fraction is reduced, the distribution goes from a smooth transition to a sandwich-like composite structure with metal in its core and ceramic on the outside.

7.1.4 Clamped Plate with Cutout

This problem was proposed by Ribeiro *et al.*[50] and deals with the maximization of the buckling load factor of a simply supported square plate. The side length measures 0.720 m

Table 12 – Optimal designs for SUS3O4/Si_3N_4 FG plate with volume constraint

Design var.	$\overline{V}_{c,max}$ = 35%			$\overline{V}_{c,max}$ = 50%			$\overline{V}_{c,max}$ = 65%		
	HF	DNN [48]	SAO	HF	DNN [48]	SAO	HF	DNN [48]	SAO
1	1.0	1.0	1.0	1.0	1.0	1.0	1.0	1.0	1.0
2	1.0	1.0	1.0	1.0	1.0	1.0	1.0	1.0	1.0
3	1.0	1.0	1.0	1.0	1.0	1.0	1.0	1.0	1.0
4	0.2501	0.2480	0.2501	0.9999	1.0	0.9999	1.0	1.0	1.0
5	0.0	0.0	0.0	0.0	0.0070	0.0	0.7497	0.7530	0.7497
6	0.0	0.0	0.0	0.0	0.0	0.0	0.0	0.0	0.0
7	0.0	0.0	0.0	0.0	0.0	0.0	0.0	0.0	0.0
$\overline{\omega}$	0.0534	0.0531	0.0534	0.0601	0.0600	0.0601	0.0671	0.0669	0.0671
Difference		-0.56%	0.00%		-0.17%	0.00%		-0.30%	0.00%
$\overline{N}_{iter}$	64		11	52		11	53		12
$\overline{n}_p$	3220		46	2650		46	2695		47
Av. time	3949 s		116 s	3228 s		115 s	3294 s		176 s

Source: the author.

Figure 34 – Volume fraction distributions for optimal designs

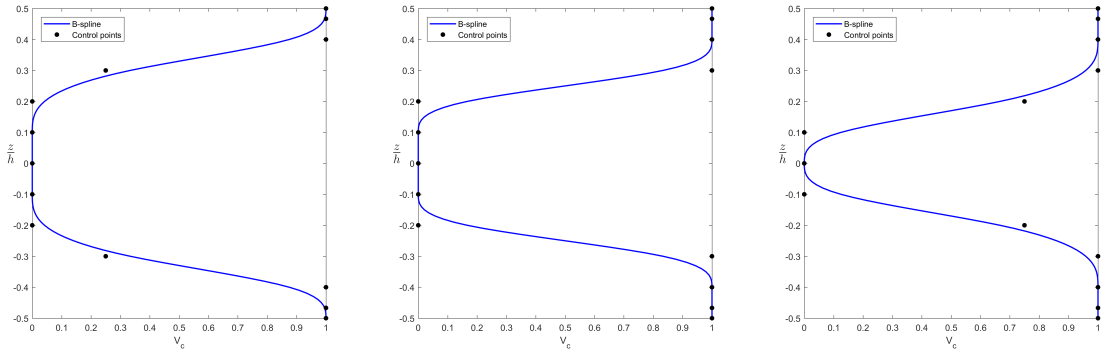

(a) $\overline{V}_{c,max} = 35\%$ (b) $\overline{V}_{c,max} = 50\%$ (c) $\overline{V}_{c,max} = 65\%$

Source: the author.

and the circular hole of radius $r = a/10$ is placed in its centre, as shown in Fig. 28. The volume fraction distribution of the FG plate is described by 9 control points symmetrically distributed, which results in 5 design variables. The effective properties are given by the Mori-Tanaka model and the material properties are described in Table 4. In addition to that, the plate thickness is also taken as variable, which increases the dimensionality of the problem. Two constraints are considered regarding the total mass of the plate and its maximum ceramic volume fraction. In

short, the optimization problem may be described as:

$$\begin{array}{ll} \text{Find} & \mathbf{x} = \{h, V_{c_i}\} \text{ for i = 1, 2, ..., 5} \\ \text{that maximizes} & \lambda_{cr}(\mathbf{x}) \\ \text{subjected to} & \overline{V}_c(\mathbf{x}) \leq \overline{V}_{c,max} \\ & M \leq M_{max} \\ \text{with} & 0.0 \leq V_{c_i} \leq 1.0 \\ & 0.01 \leq h \leq 0.05 \text{ (m)} \end{array} \tag{7.5}$$

where λ_{cr} and M_{max} are the critical buckling load factor and the maximum mass of the plate, respectively. Here, $\overline{V}_{c,max} = 50\%$ and $M_{max} = 100$ kg. Again, only the objective function is approximated since both constraints can be exactly evaluated without compromising the optimization. The performance of the SAO algorithms are described in Table 13.

Table 13 – Metrics for square plate with circular hole and $\overline{V}_{c,max} = 50\%$

Infill criterion	Surrogate model	$\overline{n}_p$	$\overline{NRMSE}$	STD_{NRMSE}	Speed-up
EI	KRG-G	42	0.75%	2.17%	43
	KRG-M	**41**	**0.33%**	**0.48%**	38
	5-FCV	45	1.01%	2.62%	**46**
	ASKIT	49	3.67%	4.18%	42
WEI	KRG-G	**41**	**0.10%**	**0.17%**	**45**
	KRG-M	**41**	0.37%	0.73%	39
	5-FCV	46	0.79%	1.70%	**45**
	ASKIT	48	3.47%	4.21%	42

Source: the author.

In this case, the results are not directly compared to the reference due to the different stopping criteria and optimization parameters considered. Ribeiro *et al.*[50] used $StallGen = 25$, while the present work allows only 10 iterations with no improvement. The conventional optimization carried out by the authors reached convergence after 107 iterations with $\lambda_{cr} = 2.469 \times 10^5$.

Again, the results obtained by the Kriging-based algorithms were less variable and more accurate than the SAOs based on RBF. In this problem, the cost of one structural analysis is much higher than the ones in the previous examples. As a consequence, the reduced number of HF evaluations needed for convergence caused KRG-G and KRG-M to reach higher speed-ups than the frameworks based on RBF, where the definition of the hyperparameters is much simpler (especially using the ASKIT). The structural analysis of this problem is on average 3.3x more expensive (≈ 4.01 s) than the analyses carried-out in previous examples (≈ 1.20 s).

In most cases, the performance of the SAO was better when considering the WEI criterion. Again, after only 1 iteration, KRG-G and KRG-M find solutions less than 1% (on average) far from the reference optimal solution by Ribeiro *et al.*[50]. Table 14 presents the best results for the conventional optimization and the KRG-G WEI, while Fig. 35 depicts the convergence history of both methods. Note that the SAO was capable of finding a solution slightly better than the conventional optimization at a much lower cost since each iteration of the SAO only evaluates the HFM once, while the conventional optimization evaluates the HFM for each particle (in this case, 50).

Table 14 – Optimal designs for FG plate with circular hole

	HF	SAO
$V_{c,1}$	0.9983	1.0
$V_{c,2}$	0.9997	0.9999
$V_{c,3}$	1.0	1.0
$V_{c,4}$	0.0	0.0
$V_{c,5}$	0.0007	0.0
h (m)	0.0378	0.0378
λ_{cr}	2.469×10^5	2.470×10^5
Difference	-	0.05%
$\overline{N}_{iter}$	39	11
$\overline{N}_p$	1970	41
Average time (s)	9947	230

Source: the author.

7.1.5 Hinged Cylindrical Panel - Nonlinear analysis

In this subsection, a modified version of a problem proposed by Moita *et al.*[57] is studied. The cylindrical panel has the straight sides hinged and the curved sides free. The structure is subjected to a point load that increases in 6 increments until $F = 51.0$ kN. The authors suggest a two-level optimization. In the first level, the centre displacement is minimized considering the power-law exponent as the design variable. In the second level, the total mass of the panel is minimized considering the thickness as the design variable. In both cases, a constraint related to the maximum centre displacement is considered. In the second level of optimization, another constraint on the maximum effective stress at the metal surface is also considered. This is the type of problem that is perhaps more adequate for a multiobjective optimization rather than for two-stage optimization with a single design variable.

Figure 35 – Convergence history for FG clamped plate problem

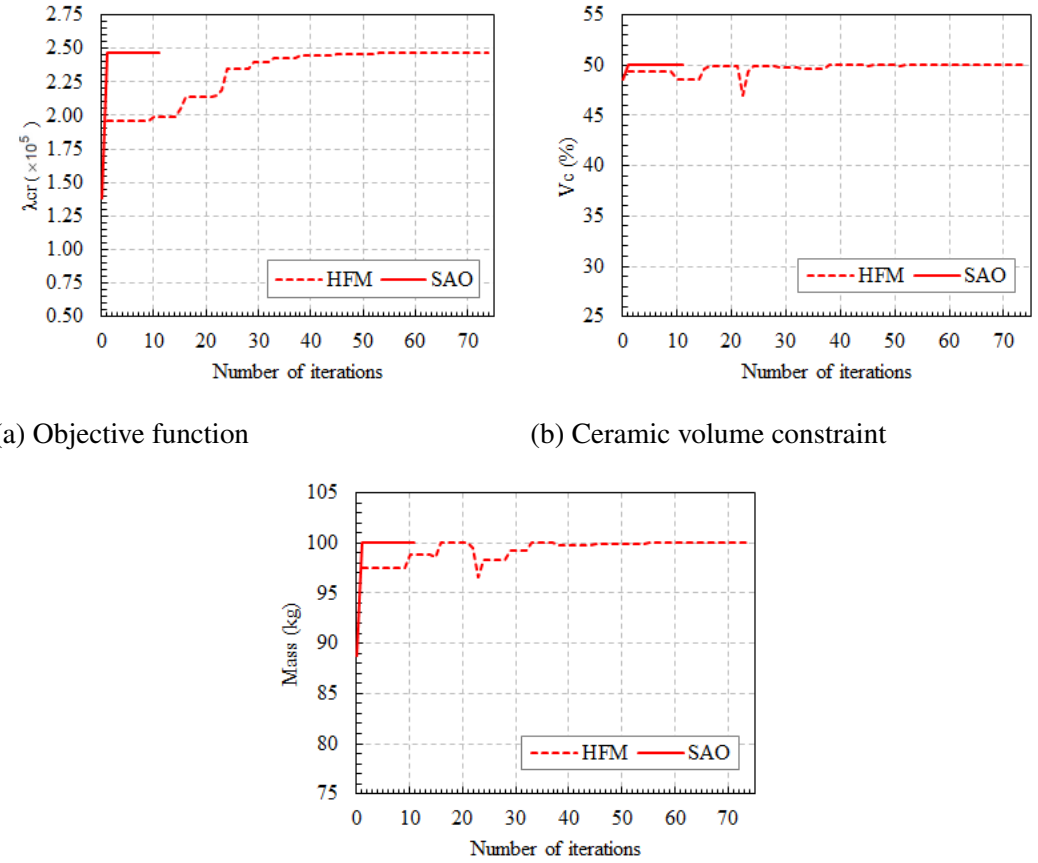

(a) Objective function

(b) Ceramic volume constraint

(c) Mass constraint

Source: the author.

The present work will adopt the following formulation:

$$\begin{array}{ll} \text{Find} & \mathbf{x} = \{h,\ p\} \\ \text{that minimizes} & M(\mathbf{x}) \\ \text{subjected to} & w_c \leq w_{max}\ \text{(mm)} \\ \text{with} & 0.008 \leq h \leq 0.035\ \text{(m)} \\ & 0.2 \leq p \leq 10.0 \end{array} \tag{7.6}$$

where w_c and w_{max} correspond to the displacement at the centre of the shell and its maximum value, respectively, and M is the total mass of the shell, given by:

$$M(\mathbf{x}) = \frac{0.2}{2\pi}\,\pi\,(r_{ext}^2 - r_{int}^2)\,L\int_{-h/2}^{h/2}\rho(z)\,dz \tag{7.7}$$

where $\rho(z)$ is the effective density at the coordinate z estimated using the Voigt model and r_{ext} and r_{int} are the external and internal radii of the shell. The material properties are found in Table 8 and $w_{max} = 4$ mm. In this study, $n_r = 3$ for the conventional optimization using the HFM. In

addition to that, $N_p = 20$, $Max_{it} = 50$ and $p_{mut} = 0.03$. The number of HF runs is reduced due to the time-consuming optimizations (5 to 6 hours on average each). For the SAOs, the number of runs is kept at $n_r = 10$ and $p_{mut} = 0.03$. The remaining optimization parameters are the same as the ones presented in Table 3.

In this particular problem, another information is reported for each SAO algorithm: the average number of iterations ($\overline{n}_{it}$), which should not be misunderstood with the number of points (although until this point, $\overline{n}_{it} = \overline{n}_p$). This occurs because it is observed that the incremental analysis of a few designs do not reach convergence. Naturally, the associated design is not added to the sampling plan and the surrogate model is not updated (since there is no value for the HF response). Hence, to prevent the algorithm to continue exploring an unfeasible point in the next iteration (recall that the hyperparameters are not updated and the approximate surface is the same), a simple function to verify if a given trial design was already visited by the SAO is incorporated. Then, in this verification, the points with no structural response are included.

Also as a result of that, the same sampling plan is used in all optimizations. This way, there is no chance of creating a sampling plan which may end up with an analysis with no convergence and thus affecting the number of initial points of the surrogate model. In this particular case, the Hammersley Sequence was used. It should also be noted that the expensive-to-evaluate function is the constraint and not the objective function. The performance of the SAO algorithms is shown in Table 15.

Table 15 – Metrics for hinged-free shallow shell problem

Infill criterion	Surrogate model	$\overline{n}_{it}$	$\overline{n}_p$	$\overline{NRMSE}$	STD_{NRMSE}	Speed-up
EI	KRG-G	39	38	0.02%	0.01%	22
	KRG-M	43	42	**0.01**%	0.01%	20
	5-FCV	32	31	19.60%	17.38%	28
	ASKIT	**21**	**21**	46.20%	**0.00**%	**37**

Source: the author.

Despite the poor performance of RBF, the 5-FCV is capable of finding the optimum solution in 3 out 10 runs. As for the ASKIT, there is no improvement on the best design of the initial sampling plan, which explains its low standard deviation of the $\overline{NRMSE}$. Finally, the best designs found by the conventional optimization and by the KRG-M are described in Table 16.

Due to the significant differences found between the present work analysis and the results presented by Moita *et al.*[57], especially on the initial design provided by the researchers, their optimal solution is not used as the reference. Instead, the present structural analysis is

Table 16 – Optimal designs for hinged-free shallow shell problem

	HF	SAO
p	0.20	0.20
h (m)	0.0123	0.0123
Mass (kg)	9.3843	9.3842
Difference	-	0.00%
$\overline{N}_{iter}$	41	33
$\overline{N}_{p}$	847	42
Average time (s)	18568	944

Source: the author.

validated using ABAQUS and other works that explored the same structure, as shown in Section 7.1.1. Nevertheless, the optimal design found in the present work is still very close to the one found by Moita *et al.*[57] after the two-stage optimization using HSDT. The authors found that the thickness should be $h = 0.012$ and $p = 0.20$, which is unfeasible considering the present analysis where FSDT is used, while this work finds $h = 0.0123$ and $p = 0.20$.

Another interesting aspect is that albeit the number of infill points is considerably higher than the ones obtained in the first numerical example (a 2-dimensional problem with both objective and constraints approximated), the speed-up of the Kriging-based algorithms are actually higher in this problem. This is also a result of the effect of the computational cost of the nonlinear analyses ($\approx$ 19 s). Fig. 36 presents the convergence history for the optimizations shown in Table 16. Again, the SAO finds the optimum design faster and at a lower cost than the optimization using the HFM.

Figure 36 – Convergence history of hinged-free shell problem

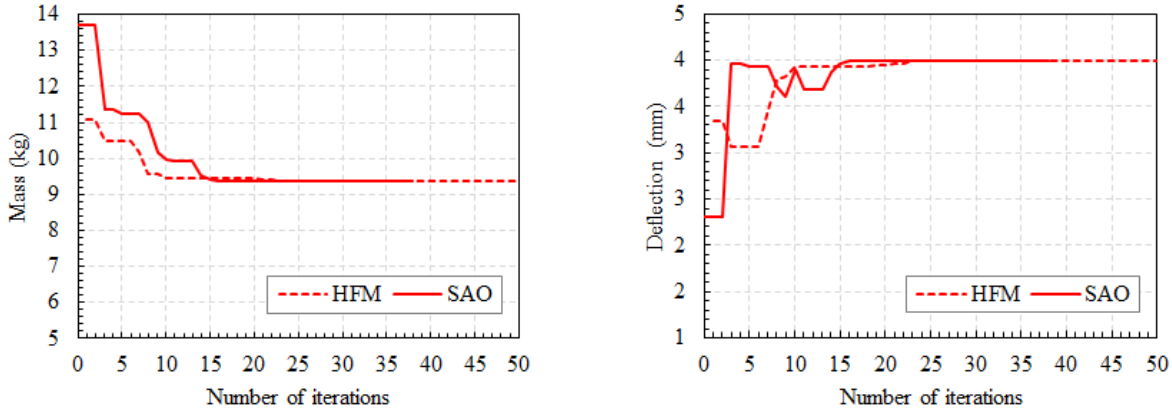

(a) Objective function

(b) Constraint

Source: the author.

Finally, Fig. 37 (a) presents the HF landscape of the objective function, a smooth and well-behaved function, while Fig. 37 (b) presents the initial surrogate model of the deflection at the centre of the shallow shell. In this case, the optimization of the Kriging hyperparameters resulted in a value of θ_1 much higher than θ_2, which means that the displacement is more sensitive to the thickness than to the power-law index.

In Fig. 37 (c), the coloured area represents the feasible design space, while the shaded area corresponds to the unfeasible design space. The first infill point is seen by the surrogate model as a feasible point with $w_c = 4$ mm. In reality, that is an unfeasible design with $w_c = 5.5$ mm. After 4 or 5 iterations, the algorithm begins to cluster around the optimum design and then starts to explore other areas (misunderstood as feasible) before returning to the exploitation of the region near the optimal solution. This process is repeated 18x until the algorithm samples the optimum solution and stalls for 10 iterations.

Figure 37 – Response surfaces of hinged-free shell problem using KRG-G

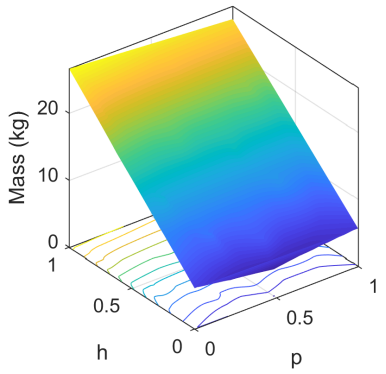

(a) HF surface

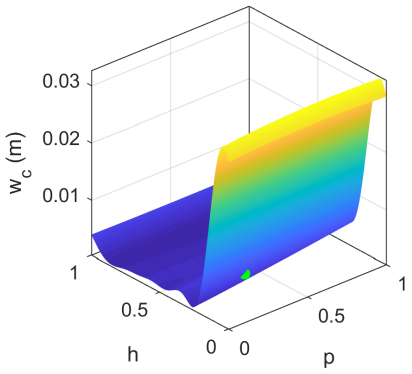

(b) Deflection surrogate model

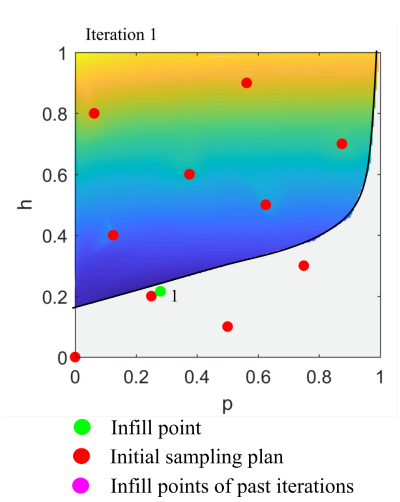

(c) First update point

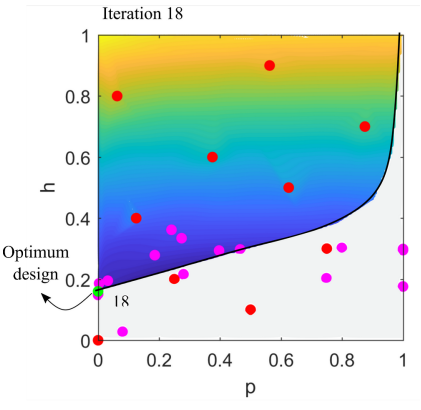

(d) 18th update point

Source: the author.

7.2 Laminated composite problems

In this section, the sampling plan is fixed for each problem. This is done due to the rounding process of bringing the continuous distribution of points to discrete points on the design space, which may lead to identical sampling points, as discussed and depicted in Fig 15. Of course, this becomes less likely as the dimension of the problem increases and with more allowed values of design variables. However, to simplify this verification, a single optimized sampling plan is considered for each problem.

This time, the OLHS was employed instead of the LHS_{sp} for better distribution of the points since the randomness of the initial sampling plan is no longer considered. The sampling plan is generated using a Matlab code provided by Forrester *et al.*[18]. The authors use a GA to solve the maximization of the *maximin*. In this case, 50 individuals and 5 generations were employed. The processing time is below 3 s. After that, BIOS is used to read and evaluate the HF response of the initial sample. This is done only once, but the time of creating and evaluating the initial sampling plan is added up to all SAO runs. If not specified, the values of the optimization parameters considered in the following examples are shown in Table 17.

Table 17 – Laminated composite problems: optimization parameters

Parameter	Conventional Opt.	Max. of EI or WEI	Max. of Likelihood Estimation
Topology	Global	Global	Global
Swarm size (N_p)	50	250	100
Maximum Iterations (It_{max})	100	100	100
$StallGen$	10	25	25
p_{mut}	0.03	0.03	0.05
p_{swap}	0.03	0.03	-
w	0.7	0.7	0.7
c_1	1.5	1.5	1.5
c_2	1.5	1.5	1.5

Source: the author.

7.2.1 Validation

The first verification regards the buckling load of a square laminated plate subjected to uniaxial load on the x-axis. A 20x20 mesh of cubic NURBS elements is considered with reduced integration. The plate length to thickness ratio is given by $a/h = 50$. Two types of boundary conditions are considered: simply supported and clamped, depicted in Fig. 38 (a) and (b), respectively.

Figure 38 – Laminated plate boundary conditions

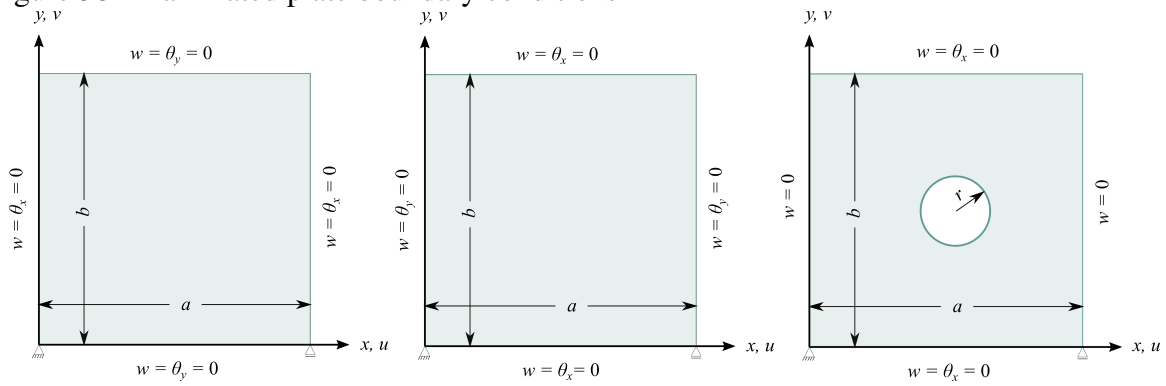

(a) Simply Supported (SSSS) (b) Clamped (CCCC) (c) SCSC plate w/ circular hole

Source: the author.

The material properties are taken from Nguyen *et al.*[153] and are presented in Table 18. To validate the SSSS and CCCC plates, the buckling load is normalized using:

$$\overline{\lambda} = \frac{N_{x,cr}\, a^2}{E_2\, h^3} \tag{7.8}$$

where $N_{x,cr}$, a and h are the buckling load factor, the edge length and the plate thickness, respectively.

The first two columns of Table 19 present the results for a simply supported laminated plate considering cross-ply and angle-ply layups. Good agreement is observed between the present work analysis and the one by Nguyen *et al.*[153]. The authors used a quadrilateral flat shell element based on the FSDT. For the CCCC plate, ABAQUS is used to carry out the analysis of the laminates shown in the last two columns of Table 19. The S8R element is used and the same mesh refinement is considered. Again, results show good agreement with the FEAs.

Table 18 – Material properties for validation of laminated plate

Material ID	E_1 (Pa)	E_2 (Pa)	G_{12} (Pa)	G_{13} (Pa)	G_{23} (Pa)	ν_{12}
I	120.0×10^9	3.0×10^9	1.8×10^9	1.8×10^9	1.5×10^9	0.25
II	120.0×10^9	4.8×10^9	2.4×10^9	2.4×10^9	0.96×10^9	0.25

Source: Adapted from Nguyen *et al.*[153].

Finally, the last example regards a square plate with circular hole. The mesh, loading and element are the same as discussed in Setion 7.1.1. However, the boundary conditions are different, as depicted in Fig. 38 (c). The length to thickness of the plate is given by $a/h = 60$ and the material properties are given in Table 20. This time, the buckling load is not normalized and the results are, again, compared to those obtained on ABAQUS using the S8R element for the layup $[\pm 45^\circ_{10}]_s$.

Table 19 – Normalized buckling loads for different layups and boundary conditions

Layup	$[0°/90°]$	$[\pm 45°]$	$[(0°/90°)_2/0°]_s$	$[\pm 45°_2/45°]_s$
Boundary condition	SSSS	SSSS	CCCC	CCCC
Material ID	I	II	I	I
Reference	12.906[153]	15.374[153]	125.49[151]	109.88[151]
Present work	12.896	15.373	125.58	110.19
Difference (%)	-0.08	0.00	0.07	0.29

Source: the author.

Table 20 – Material properties for laminated plate with circular hole

E_1 (Pa)	E_2 (Pa)	G_{12} (Pa)	G_{13} (Pa)	G_{23} (Pa)	ν_{12}
127.59×10^9	13.03×10^9	6.41×10^9	7.10×10^9	6.20×10^9	0.30

Source: Adapted from Balreira[149].

The strain failure load is evaluated using the Maximum Strain Criterion with a minimum safety factor (S_f) of 1.50. The failure load factor of the laminate may be calculated as:

$$\lambda_s = \min_k(\min(\frac{\varepsilon_1^u}{S_f\varepsilon_1^k}, \frac{\varepsilon_2^u}{S_f\varepsilon_2^k}, \frac{\gamma_{12}^u}{S_f\gamma_{12}^k})) \tag{7.9}$$

where k refers to the strains of the k-th ply and the superscript u refers to the ultimate strains (i.e., maximum allowable strain) of ε_1, ε_2 and γ_{12}. In this case, $\varepsilon_1^u = 0.008$, $\varepsilon_2^u = 0.025$ and $\gamma_{12}^u = 0.015$. Therefore, 2 types of analysis were carried-out, one for the assessment of the buckling load (λ_b) and another to find the strains of the laminated plate, allowing the calculation of λ_s. Table 21 presents a comparison for both load factors, where, once again, no significant difference is observed.

Table 21 – Load factors of laminated plate w/ circular hole

	λ_s	λ_b
ABAQUS[151]	644.97	1221.90
Present work	645.16	1224.81
Difference (%)	0.03	0.24

Source: the author.

7.2.2 Laminated Plate with Various Boundary Conditions

In this subsection, the effects of different boundary conditions are investigated for a dispersed laminated plate under uniaxial compression. The objective function is the normalized

buckling load factor ($\overline{\lambda}$) and the design variables are the fibre orientations. The number of plies is fixed at 20 and only symmetric balanced layups are allowed, which reduces the number of design variables to 5. The mathematical formulation may be described as follows:

$$\begin{array}{ll} \text{Find} & \mathbf{x} = \{\theta_i\} \text{ for } i = 1,2,\ldots,5 \\ \text{that maximizes} & \overline{\lambda}(\mathbf{x}) \\ \text{subjected to} & \text{Max contiguous plies} \leq 4 \\ \text{with} & \theta_i \in [0^\circ\ 15^\circ\ 30^\circ\ 45^\circ\ 60^\circ\ 75^\circ\ 90^\circ] \end{array} \tag{7.10}$$

The geometry properties are given by: $a = b = 1$ m and $a/h = 50$. Thus, the thickness of each ply is $h_i = 0.001$ m. The material properties are given in Table 18. The laminate is optimized considering two boundary conditions: SSSS and CCCC. The performance of the SAO algorithms are shown in Table 22.

Table 22 – Metrics for laminated plate with different boundary conditions

Boundary condition	Infill criterion	Surrogate model	$\overline{n}_p$	$\overline{NRMSE}$	STD_{NRMSE}	Speed-up
SSSS	EI	KRG-G	41	**0.00**%	**0.00**%	19
		KRG-M	44	**0.00**%	**0.00**%	14
		5-FCV	**37**	0.08%	**0.00**%	**26**
		ASKIT	43	**0.00**%	0.70%	21
	WEI	KRG-G	41	**0.00**%	**0.00**%	18
		KRG-M	47	**0.00**%	**0.00**%	12
		5-FCV	**36**	0.08%	**0.00**%	**27**
		ASKIT	**36**	**0.00**%	**0.00**%	**27**
CCCC	EI	KRG-G	46	0.06%	0.03%	15
		KRG-M	**37**	**0.00**%	**0.00**%	18
		5-FCV	41	0.18%	**0.00**%	**21**
		ASKIT	38	1.16%	**0.00**%	23
	WEI	KRG-G	**36**	**0.00**%	**0.00**%	21
		KRG-M	**36**	**0.00**%	**0.00**%	19
		5-FCV	38	0.07 %	0.08%	**24**
		ASKIT	42	0.34%	0.27%	21

Source: the author.

For the simply supported plate, virtually all methods are capable of finding the optimal layup. Due to its fast convergence and quick model updating, the RBF-based algorithms are particularly effective. Both methods used to define the widths reached accuracy and robustness metrics very close to those obtained by Kriging with higher speed-up and fewer HF evaluations.

Regarding the clamped plate, the best performance is obtained by the Kriging-based algorithms, particularly in association with the WEI criterion. The SAOs based on RBF also provide consistent and accurate results with a slightly higher number of HF evaluations. Fig. 39 (a) presents the convergence history for the clamped plate with the best performance of each

surrogate model. The KRG-G WEI curve overlaps the results obtained by the conventional optimization, while the 5-FCV is only 0.07% below the reference optimal solution.

In Fig. 39 (b) and (c), the hyperparameters obtained by the 5-FCV and KRG-G are shown for each iteration of the SAO. The 5-FCV width (all basis have the same width) varied between 1.5 and 10, while the Kriging hyperparameters varied between 0.1 and 3.0. It is interesting to point out that the optimum hyperparameters found by the optimization of the Maximum Likelihood Estimation translate numerically the fact that the objective function is significantly more sensitive to changes in the fibre orientation of outer layers than the ones close to the midplane. This is expected since the outer plies present a larger lever arm.

Figure 39 – Convergence history and hyperparameters for clamped plate

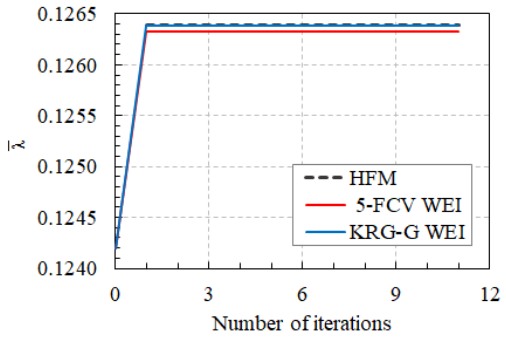

(a) Objective function

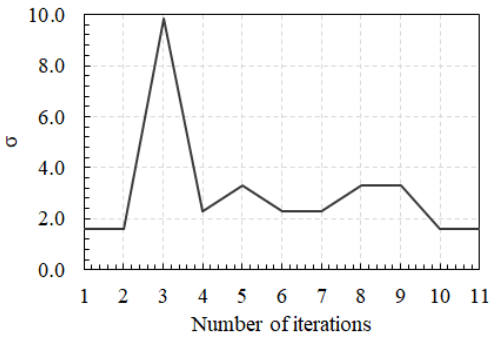

(b) 5-FCV WEI widths

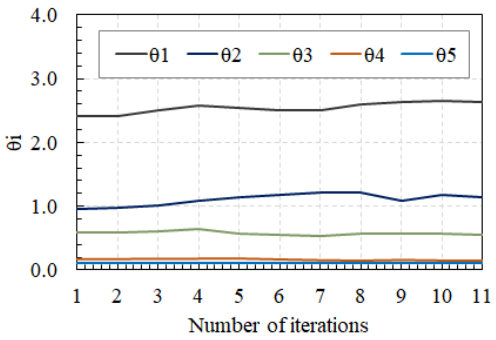

(c) KRG-G WEI θs

Source: the author.

Finally, the best designs obtained by the conventional optimization and the SAOs are shown in Table 23. The SAO results refer to the ASKIT WEI and KRG-G WEI for the SSSS and CCCC plates, respectively. For the first choice, an angle-ply layup with all plies at $\pm 45°$ is obtained, while the stacking sequence for the clamped plate contains more specially orthotropic

Table 23 – Optimal designs for laminated plate with different boundary conditions

	SSSS		CCCC	
	HF	SAO	HF	SAO
Layup	$[\pm 45^\circ_5]_s$	$[\pm 45^\circ_5]_s$	$[0^\circ_4/90^\circ_2/0^\circ_2/\pm 15^\circ]_s$	$[0^\circ_4/90^\circ_2/0^\circ_2/\pm 15^\circ]_s$
$\overline{\lambda}$	0.065	0.065	0.126	0.126
Difference	-	0.00%	-	0.00%
$\overline{N}_{iter}$	17	11	16	11
$\overline{n}_p$	900	46	855	46
Average time	3233 s	119 s	3034 s	238 s

Source: the author.

plies with the pair $\pm 15^\circ$ being introduced to fulfill the problem constraint.

7.2.3 Simply Supported-Clamped Plate with Cutout

This problem was originally proposed by Balreira[149] and deals with the maximization of the strength of a simply supported square laminated plate. The side length measures $a = b = 0.72$ m and a circular hole of $r = a/10$ is placed in its centre. The laminated plate is made of 40 plies, each with 0.3 mm, and fixed material (see Table 20).

The design variables are the fibre orientation of each ply. Only balanced symmetrical layups are allowed, which reduces the number of design variables to 10. In addition to that, a constraint limits the number of contiguous plies. In short, the optimization problem may be described as:

$$\begin{array}{ll} \text{Find} & \mathbf{x} = \{\theta_i\} \text{ for } i = 1, 2, \ldots, 10 \\ \text{that maximize} & \min(\lambda_s, \lambda_b) \\ \text{subjected to} & \text{Max contiguous plies} \leq 4 \\ \text{with} & \theta_i \in [0^\circ\ 45^\circ\ 90^\circ] \end{array} \tag{7.11}$$

where λ_s is the strain failure load factor and λ_b is the buckling load factor. The strain failure load factor is evaluated using the Maximum Strain Criterion with $S_f = 1.5$, as discussed in Section 7.2.1.

In this example, only one surrogate model is built, which means that only the minimum response between the load factors is considered. Alternatively, one could build two surrogate models, each for a load factor. However, this would double the size of the optimization problem (particularly for the maximization of the hyperparameters in Kriging).

In addition to that, the mutation and the swap probabilities for the maximization of the infill criteria are increased to $p_{mut} = p_{swap} = 0.05$. Also, for the maximization of MLE,

the swarm size is increased to $N_p = 250$. In this problem, only five runs of the conventional optimization using the HFM are performed due to the time-consuming optimizations (4-6 hours each). To confirm the optimal solutions found by the sequential runs, five more runs are carried out considering 20 threads simultaneously. In one of these, an optimum solution is found to be better than the best one obtained by the sequential runs. Therefore, this solution is used as the reference to calculate the accuracy of the SAO methods. The wall-clock times of the parallel executions are not accounted for the computation of the T_{HFM}. The performance of the SAO algorithms is described in Table 24.

Table 24 – Metrics for laminated plate with circular hole

Infill criterion	Surrogate model	$\bar{n}_p$	$\overline{NRMSE}$	STD_{NRMSE}	Speed-up
EI	KRG-G	71	**1.38**%	0.73%	14
	KRG-M	68	1.45%	0.66%	11
	5-FCV	64	4.31%	0.74%	31
	ASKIT	**61**	4.65%	**0.00**%	**35**
WEI	KRG-G	73	**1.27**%	0.39%	14
	KRG-M	71	1.48%	0.62%	8
	5-FCV	**61**	4.65%	**0.00**%	**34**
	ASKIT	66	3.40%	1.62%	29

Source: the author.

Again, the most accurate model is obtained using KRG-G and WEI, whilst the RBF-based algorithms do not exhibit a clear pattern on whether the EI or WEI is best suited. It is worth noting that the lowest value of STD_{NRMSE} should be carefully interpreted. For example, the low STD_{NRMSE} of the 5-FCV approach actually reflects the fact that the algorithm is not capable of finding a better solution than the best design found in the initial sampling plan and not the fact that the SAO is robust.

Table 25 presents the best designs for each case. The SAO results refer to the best solution found by the KRG-G WEI. Note that the layup obtained by the SAO is almost identical to the one obtained by the sequential conventional optimization and only differs in the last pair of fibre orientation.

It is also worth highlighting the search capacity of the PSO algorithm. The number of possible combinations of this problem is given by the number of allowable fibre orientations values raised to the the number of variable plies, which gives $3^{10} = 59049$ possibilities. In this case, both the sequential and the parallel HF executions explored less than 2% of the number of combinations. For the SAO approaches, this number is even lower: only 0.12%. This shows the capacity of exploration and exploitation of the methods in covering the design space.

Table 25 – Optimal designs for laminated plate with circular hole

	$HF_{parallel}$	$HF_{sequential}$	SAO
Layup	$[\pm45^\circ_3/90^\circ_2/0^\circ_2/\pm45^\circ/0_4^\circ/90^\circ_2/0^\circ_2]_s$	$[\pm45^\circ_2/90^\circ_2/(\pm45^\circ/0^\circ_4)_2/90^\circ_2]_s$	$[\pm45^\circ_2/90^\circ_2/(\pm45^\circ/0^\circ_4)_2/\pm45^\circ]_s$
λ_s	1254.38	1254.38	1272.74
λ_b	1215.31	1213.32	1204.22
λ_{min}	1215.31	1213.32	1204.22
Difference	-	-0.16%	-0.91%
$\overline{N}_{iter}$	21	21	23
$\overline{n}_p$	1120	1080	73
Av. time (s)	-	13076	1094

Source: the author.

Fig. 40 presents the convergence history for the optimizations shown in Table 25. For the SAO approach, the buckling load factor is, at all times, the lowest load factor. Therefore, the curve of the minimum load factor overlaps the buckling load factor curve. When compared to the optimization using the HFM, it can be seen that the SAO makes substantial progress during the initial stages of the search, but the "fine-tuning" is slow (if any). This behaviour is also discussed by Sóbester *et al.*[135], which is quite the opposite of the HF runs, where small, but gradual and constant improvement is made.

Figure 40 – Convergence history for laminated plate w/ circular hole

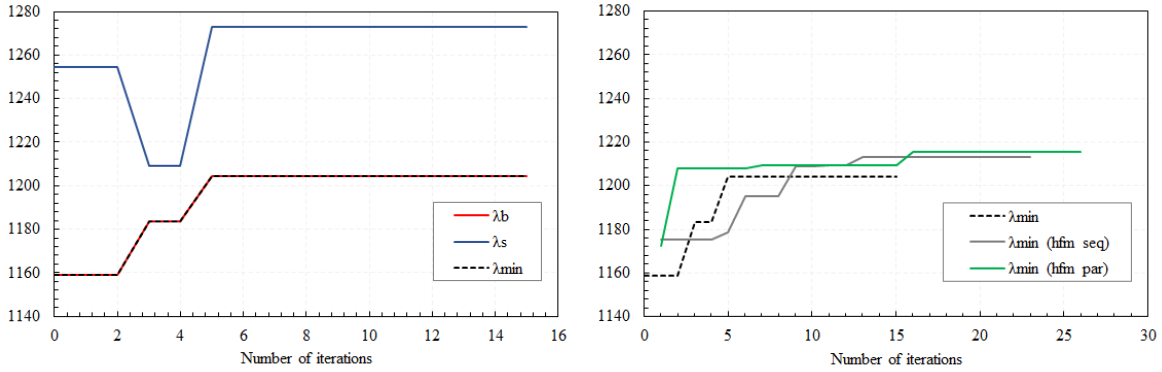

(a) Best SAO performance (b) Different methods

Source: the author.

8 CONCLUSION

This work investigated the use of Sequential Approximate Optimization techniques to the design of composite structures. For that matter, a set optimization methodologies were proposed involving two surrogate models, RBF and Kriging, and two infill criteria, the Expected Improvement and the Weighted Expected Improvement. For the RBF, two width-defining method were studied: a closed-form expression found in the literature and a k-FOLD CV. In the first case, each basis is assigned a width value, while the latter applies the same width for all bases. As for Kriging, two correlation functions were considered: the Gaussian and the Matérn 5/2 functions. To fit the hyperparameters of these functions, the Maximum Likelihood Estimator is maximized.

The main contributions from this work regard the implementation of Kriging and the SAO algorithms derived from it on BIOS, an academic software developed in C++ by the LMCV collaborators. The implementation included the creation of a class to handle common functions to all SAO algorithms such as the reading or creation of the initial sampling plan, selection of the proper infill strategy depending on the outputs being approximated, post-processing of the metrics used to assess SAO performance, etc.

In addition to that, the evaluation of the effective properties of FG structures (Voigt and Mori-Tanaka models) and other volume fraction distributions (Power-Law and Sigmoid functions) were also incorporated to the optimization program as an intern routine. That was also the case of the routines for the numerical integration of the constitutive matrix and an auxiliary matrix for the mass matrix evaluation. These matrices work as input data to the structural analysis carried out on FAST. The latter being particularly important for the free vibration analysis of FG structures without the need for through-thickness discretization methods (e.g. virtual layers).

The structural responses of the composite structures were evaluated using the Isogeometric Analysis (IGA). A cubic shallow shell element based on the Reissner-Mindlin plate theory and Marguerre strains was employed.

The numerical examples comprehend a wide range of relevant characteristics for the optimization of composite structures. There are eigenvalue problems, geometrically nonlinear analysis using an incremental-iterative process, complex geometries, different loading and boundary conditions, consideration of traditional and disperse laminates, among others. Another interesting aspect concerns the different strategies used to tackle the problem depending on the nature (expensive or cheap) of the objective function and the constraints. At this point, it is worth mentioning the scarce literature when it comes to Kriging-based SAO algorithms, particularly

for FG structures. This also holds for the surrogate-based optimization of composite structures considering the nonlinearity of the material, geometry, etc.

The results showed that the performance of Kriging-based algorithms is slightly better using the WEI criterion, while the RBF-based did not show a significant difference between the infill criteria studied. Although both correlation functions provided excellent and similar accuracy metrics, the Matérn 5/2 correlation function was found to be considerably more expensive than that of a Gaussian function the same number of HF evaluations. In general, the SAO algorithms based on Kriging provided excellent accuracy with the lowest number of infill points. At times, the SAO provided optimal solutions better than the optimal designs obtained by the conventional optimization using the HFM. In all cases, an expressive reduction in the number of HF evaluations was obtained compared to the traditional optimization, reaching up to 98% of reduction on the average number of HF evaluations.

The building and updating process of the Kriging-based algorithms demand a higher computational cost than the definition of the width parameter on RBFs (either using CV techniques or analytically). Recall that the definition of the Kriging hyperparameters is itself an optimization problem. On this matter, the RBFs have undoubtedly the fastest surrogate model building and updating processes, particularly when the k-Fold is used to define the basis function widths. This is the opposite of what is expected since the ASKIT methodology evaluates the width of the basis analytically. However, the CV technique showed faster convergence and more accurate results in most cases.

While the RBF-based algorithms present speed-up ranging from 16 to 46, the Kriging ones ranged between 8 to 45. This does not mean, however, that the Kriging-based algorithms are less efficient. Results actually show that these algorithms become particularly competitive regarding the speed-up as the analysis cost increases (and for problems with a low number of design variables). Furthermore, it should be stressed that these algorithms provide the most accurate and less variable results.

In general, the results illustrate that the use of the SAO can significantly reduce computational cost and greatly improve the optimization efficiency. This will hopefully ease the optimization of structures that demand expensive-to-evaluate analysis in future works, allowing the consideration of more sophisticated methods (e.g., progressive failure, consideration of loss of stability by limit load, etc.). The SAO approach also allows the designer to understand the relative importance of the design variables (i.e. screening study) by working on a cheap-to-run

model and through the understanding of the model hyperparameters.

The following suggestions can be further explored in future works:

a) The effect of the size of the initial sampling plan on the surrogate model performance;
b) Alternative methods for dealing with constrained problems;
c) Use of a variable global trend for the Kriging estimates, namely the Universal Kriging;
d) Use of other optimization algorithms on the SAO performance (e.g., Differential Evolution, Genetic Algorithms, etc.);
e) Use of SAO techniques (based on RBF or Kriging) in multiobjective problems;
f) Use of other approaches to tackle ill-conditioning problems of the correlation matrix in Kriging;
g) Study the effect of the problem dimension on the performance of the SAO;
h) Optimization of hybrid laminates or laminates with variable thickness;
i) Consideration of thermo-mechanical loads for the optimization of FG structures.

BIBLIOGRAPHY

1 ILCEWICZ, L.; HOFFMAN, D.; FAWCETT, A. Composite Applications in Commercial Airframe Structures. **Comprehensive Composite Materials**, p. 87–119, 2004.

2 REDDY, J. N.; KHDEIRF, A. A.; INTRODUCTION, I.; EQUATIONS, G. Plates Using Various Plate Theories. v. 27, n. 12, p. 1808–1817, 1989.

3 BARBERO, E. J.; RAFTOYIANNIS, I. G. Lateral and distortional buckling of pultruded I-beams. **Composite Structures**, v. 27, n. 3, p. 261–268, 1994. ISSN 02638223.

4 JONES, R. M. **Mechanics of Composite Materials**. 2d. ed. Philadelphia, USA: Taylor & Francis, 1999. ISBN 156032712X.

5 REDDY, J. N. **Mechanics of Laminated Composite Plates and Shells: Theory and Analysis**. 2nd. ed. [S.l.]: CRC Press, 2003. 858 p. ISBN 9780849315923.

6 KOIZUMI, M. Fgm activities in japan. **Composites Part B: Engineering**, v. 28, n. 1, p. 1 – 4, 1997. ISSN 1359-8368. Use of Composites Multi-Phased and Functionally Graded Materials.

7 SHEN, H.-S. **Functionally graded materials : nonlinear analysis of plates and shells**. [S.l.: s.n.], 2009. 278 p. ISSN 2321-581X. ISBN 9780080532943.

8 JHA, D. K.; KANT, T.; SINGH, R. K. A critical review of recent research on functionally graded plates. **Composite Structures**, Elsevier Ltd, v. 96, p. 833–849, 2013. ISSN 02638223.

9 LIN, D.; LI, Q.; LI, W.; ZHOU, S.; SWAIN, M. V. Design optimization of functionally graded dental implant for bone remodeling. **Composites Part B: Engineering**, v. 40, n. 7, p. 668 – 675, 2009. ISSN 1359-8368. Natural fiber composites.

10 KHORSAND, M.; TANG, Y. Design functionally graded rotating disks under thermoelastic loads : Weight optimization. **International Journal of Pressure Vessels and Piping**, Elsevier, v. 161, n. November 2017, p. 33–40, 2018. ISSN 0308-0161.

11 GASIK, M.; BILOTSKY, Y. Optimisation of functionally gradated material thermoelectric cooler for the solar space power system. **Applied Thermal Engineering**, Elsevier Ltd, v. 66, n. 1-2, p. 528–533, 2014. ISSN 1359-4311.

12 NIKBAKHT, S.; KAMARIAN, S.; SHAKERI, M. A review on optimization of composite structures Part II: Functionally graded materials. **Composite Structures**, Elsevier, v. 214, n. January, p. 83–102, 2019. ISSN 02638223.

13 NIKBAKT, S.; KAMARIAN, S.; SHAKERI, M. A review on optimization of composite structures part i: Laminated composites. **Composite Structures**, v. 195, p. 158 – 185, 2018. ISSN 0263-8223.

14 HUSSEIN, O. S.; MULANI, S. B. Multi-dimensional optimization of functionally graded material composition using polynomial expansion of the volume fraction. **Structural and Multidisciplinary Optimization**, Structural and Multidisciplinary Optimization, v. 56, n. 2, p. 271–284, 2017. ISSN 16151488.

15 SOFIYEV, A. H. Review of research on the vibration and buckling of the FGM conical shells. **Composite Structures**, v. 211, n. October 2018, p. 301–317, 2019. ISSN 02638223.

16 ARORA, J. S. **Introduction to Optimum Design**. Second. Iowa: Elsevier Academic Press, 2012. 657–679 p. ISSN 02668920. ISBN 9780123813756. Disponível em: <http://www.sciencedirect.com/science/article/pii/B9780123813756000176>.

17 HARDY, R. L. Multiquadric Equations of Topography and Other Irregular Surfaces. **Journal of Geophysical Research**, v. 76, n. 8, p. 1905–1915, 1971.

18 FORRESTER, A. I. J.; SBESTER, A.; KEANE, A. J. **Engineering Design via Surrogate Modelling**. [S.l.: s.n.], 2008. ISBN 9780470770801.

19 MARTIN, J. D.; SIMPSON, T. W. Use of Kriging Models to Approximate Deterministic Computer Models. v. 43, n. 4, 2005.

20 WENGUO, Z.; ZHIJUN, M.; JUN, H.; WEI, H. Optimization Design for Laminated Composite Structure Based on Kriging Model. n. 1, p. 179–183, 2012.

21 LUERSEN, M. A.; STEEVES, C. A.; NAIR, P. B. Curved fiber paths optimization of a composite cylindrical shell via kriging-based approach. **Journal of Composite Materials**, v. 49, n. 29, p. 3583–3597, 2015.

22 PASSOS, A. G.; LUERSEN, M. A. Multiobjective optimization of laminated composite parts with curvilinear fibers using Kriging-based approaches. **Structural and Multidisciplinary Optimization**, Structural and Multidisciplinary Optimization, v. 57, n. 3, p. 1115–1127, 2018. ISSN 16151488.

23 VALLADARES, H.; JONES, A.; TOVAR, A. Surrogate-based global optimization of composite material parts under dynamic loading. In: **WCX World Congress Experience**. [S.l.]: SAE International, 2018. ISSN 0148-7191.

24 KESHTEGAR, B.; NGUYEN-THOI, T.; TRUONG, T. T.; ZHU, S.-P. Optimization of buckling load for laminated composite plates using adaptive kriging-improved pso: A novel hybrid intelligent method. **Defence Technology**, 2020. ISSN 2214-9147.

25 CHENG, Y.-c.; JIANG, C.-p.; LIN, D.-h.; LIN, D.-h. Finite element based optimization design for a one-piece zirconia ceramic dental implant under dynamic loading and fatigue life validation. Structural and Multidisciplinary Optimization, p. 835–849, 2019.

26 JIN, R.; CHEN, W.; SIMPSON, T. W. Comparative studies of metamodelling techniques under multiple modelling criteria. **Structural and Multidisciplinary Optimization**, v. 23, n. 1, p. 1–13, 2001. ISSN 1615147X.

27 BARROSO, E. S.; PARENTE, E.; Cartaxo de Melo, A. M. A hybrid PSO-GA algorithm for optimization of laminated composites. **Structural and Multidisciplinary Optimization**, v. 55, n. 6, p. 2111–2130, jun 2017. ISSN 1615-147X.

28 ROCHA, I. B. C. M.; Parente Jr, E.; MELO, A. M. C. A hybrid shared/distributed memory parallel genetic algorithm for optimization of laminate composites. **Composite Structures**, Elsevier Ltd, v. 107, n. 1, p. 288–297, 2014. ISSN 02638223.

29 OMKAR, S.; SENTHILNATH, J. Artificial Bee Colony (ABC) for multi-objective design optimization of composite structures. **Applied Soft Computing**, v. 11, n. 1, p. 489–499, 2011. ISSN 15684946.

30 PUNCH, W.; AVERILL, R.; GOODMAN, E.; LIN, S.-C.; DING, Y.; YIP, Y. Optimal design of laminated composite structures using coarse-grain parallel genetic algorithms. **Computing Systems in Engineering**, v. 5, n. 4, p. 415 – 423, 1994. ISSN 0956-0521. 3rd National Symposium on Large-Scale Structural Analysis for High-Performance Computers and Workstations.

31 National Chung Hsing University. **Chapter 14 - Composites**. 2017. Disponível em: <http://web.nchu.edu.tw/{~}jillc/me/Ch14-Composites.p>.

32 DET NORSKE VERITAS. DNV-OS-F201 Dynamic Risers. n. October, p. 91, 2010. Disponível em: <http://rules.dnvgl.com/docs/pdf/DNV/codes/docs/2010-10/Os-F201.pdf>.

33 KOIZUMI, M. FGM activities in Japan. **Composites Part B: Engineering**, v. 28, n. 1-2, p. 1–4, 2002. ISSN 13598368.

34 NGUYEN, T. T.; LEE, J. Optimal design of thin-walled functionally graded beams for buckling problems. **Composite Structures**, Elsevier Ltd, v. 179, p. 459–467, 2017. ISSN 02638223.

35 GÜRDAL, Z.; HAFTKA, R. T.; HAJELA, P. **Design and Optimization of Laminated Composite Materials**. Danvers, USA: Wiley, 1999. 352 p.

36 MALLICK, P. K. **Fiber-Reinforced Composites: Materials, Manufacturing and Design**. 3rd. ed. New York: CRC Press, 2008. 616 p. ISBN 9780849342059.

37 MAJI, A.; MAHATO, P. K. Development and applications of shear deformation theories for laminated composite plates: An overview. **Journal of Thermoplastic Composite Materials**, v. 0, n. 0, p. 0892705720930765, 0.

38 TEÓFILO, F. A. F.; JÚNIORMELO, E. P.; MELO, A. M. C. de; HOLANDA, Á. S. de; SILVA, R. F. da. Premilinary design of composite catenary risers using optimization techniques. **Asociación Argentina de Mecánica Computacional**, XXIX, p. 7927–7948, 2010.

39 LOPEZ, R. H.; LUERSEN, M. A.; CURSI, E. S. Optimization of laminated composites considering different failure criteria. **Composites Part B: Engineering**, Elsevier Ltd, v. 40, n. 8, p. 731–740, 2009. ISSN 13598368.

40 DANIEL, I. M. Failure of composite materials under multi-axial static and dynamic loading. **Procedia Engineering**, v. 88, p. 10–17, 12 2014.

41 Medeiros JR., M. S.; Parente Jr., E.; MELO, A. M. C. de. Influence of the Micromechanics Models and Volume Fraction Distribution on the Overall Behavior of SiC/Al Functionally Graded Pressurized Cylinders. **Latin American Journal of Solids and Structures**, v. 16, n. 4, p. 1–15, apr 2019. ISSN 1679-7825.

42 UDUPA, G.; RAO, S. S.; GANGADHARAN, K. Functionally Graded Composite Materials: An Overview. **Procedia Materials Science**, v. 5, p. 1291–1299, 2014. ISSN 22118128.

43 DELALE, F.; ERDOGAN, F. The crack problem for a nonhomogeneous plane. **Journal of Applied Mechanics, Transactions ASME**, v. 50, 07 1983.

44 BAO, G.; WANG, L. Multiple cracking in functionally graded ceramic/metal coatings. **International Journal of Solids and Structures**, v. 32, n. 19, p. 2853 – 2871, 1995. ISSN 0020-7683.

45 CHUNG, Y.-L.; CHI, S. The residual stress of functionally graded materials. **Journal of the Chinese Institute of Civil and Hydraulic Engineering**, v. 13, p. 1–9, 01 2001.

46 TAHERI, A.; HASSANI, B. Simultaneous isogeometrical shape and material design of functionally graded structures for optimal eigenfrequencies. **Computer Methods in Applied Mechanics and Engineering**, v. 277, p. 46 – 80, 2014. ISSN 0045-7825. Disponível em: <http://www.sciencedirect.com/science/article/pii/S004578251400139X>.

47 LIEU, Q. X.; LEE, J.; LEE, D.; LEE, S.; KIM, D.; LEE, J. Shape and size optimization of functionally graded sandwich plates using isogeometric analysis and adaptive hybrid evolutionary firefly algorithm. **Thin-Walled Structures**, Elsevier Ltd, v. 124, n. September 2017, p. 588–604, 2018. ISSN 02638231. Disponível em: <https://doi.org/10.1016/j.tws.2017.11.054>.

48 DO, D. T.; LEE, D.; LEE, J. Material optimization of functionally graded plates using deep neural network and modified symbiotic organisms search for eigenvalue problems. **Composites Part B: Engineering**, Elsevier, v. 159, n. September 2018, p. 300–326, 2019. ISSN 13598368.

49 WANG, C.; YU, T.; CURIEL-SOSA, J. L.; XIE, N.; BUI, T. Q. Adaptive chaotic particle swarm algorithm for isogeometric multi-objective size optimization of FG plates. **Structural and Multidisciplinary Optimization**, Structural and Multidisciplinary Optimization, v. 60, n. 2, p. 757–778, 2019. ISSN 16151488.

50 RIBEIRO, L. G.; MAIA, M. A.; Parente Jr., E.; MELO, A. M. C. de. Surrogate based optimization of functionally graded plates using radial basis functions. **Composite Structures**, v. 252, p. 112677, 2020. ISSN 0263-8223.

51 GROSS, D.; SEELIG, T. **Fracture Mechanics With an Introduction to Micromechanics**. [S.l.: s.n.], 2011. ISBN 9783642192401.

52 PELLETIER, J. L.; VEL, S. S. Multi-objective optimization of fiber reinforced composite laminates for strength, stiffness and minimal mass. **Computers and Structures**, v. 84, n. 29-30, p. 2065–2080, 2006. ISSN 00457949.

53 TOULOUKIAN, Y. S. **Thermophysical Properties Research Literature Retrieval Guide: Editor: YS Touloukian**. [S.l.]: Plenum Press, 1967.

54 SHEN, H.-S.; WANG, Z.-X. Assessment of voigt and mori–tanaka models for vibration analysis of functionally graded plates. **Composite Structures**, v. 94, n. 7, p. 2197 – 2208, 2012. ISSN 0263-8223.

55 KOU, X. Y.; PARKS, G. T.; TAN, S. T. Optimal design of Functionally Graded Materials using a procedural model and Particle Swarm Optimization. **CAD Computer Aided Design**, Elsevier Ltd, v. 44, n. 4, p. 300–310, 2012. ISSN 00104485. Disponível em: <http://dx.doi.org/10.1016/j.cad.2011.10.007>.

56 ASGARI, M. Material optimization of functionally graded heterogeneous cylinder for wave propagation. **Journal of Composite Materials**, v. 50, n. 25, p. 3525–3538, 2016. ISSN 1530793X.

57 MOITA, J. S.; ARAÚJO, A. L.; FRANCO, V.; MOTA, C. M. Material distribution and sizing optimization of functionally graded plate- shell structures. **Composites Part B**, Elsevier, v. 142, n. November 2017, p. 263–272, 2018. ISSN 1359-8368. Disponível em: <https://doi.org/10.1016/j.compositesb.2018.01.023>.

58 TAMURA, I. Strength and ductility of fe-ni-c alloys composed of austenite and martensite with various strength. **Proceedings of the third international conference on strength of metals and alloys, 1973**, Cambridge, Institute of Metals, v. 1, p. 611–615, 1973. Disponível em: <https://ci.nii.ac.jp/naid/80013184461/en/>.

59 JIN, Z.-H.; PAULINO, G. H.; DODDS, R. H. Cohesive fracture modeling of elastic–plastic crack growth in functionally graded materials. **Engineering Fracture Mechanics**, v. 70, n. 14, p. 1885 – 1912, 2003. ISSN 0013-7944. Cohesive Models.

60 VEL, S. S.; PELLETIER, J. L. Multi-objective optimization of functionally graded thick shells for thermal loading. **Composite Structures**, v. 81, p. 386–400, 2006.

61 BORST, R. D.; CRISFIELD, M. A.; REMMERS, J. J.; VERHOOSEL, C. V. **Nonlinear finite element analysis of solids and structures**. [S.l.]: John Wiley & Sons, 2012.

62 REISSNER, E. On bending of elastic plates. **Quarterly of Applied Mathematics**, v. 5, p. 55–68, 1947.

63 CHATTERJEE, S. N.; KULKARNI, S. V. Shear correction factors for laminated plates. **AIAA Journal**, v. 17, n. 5, p. 498–499, 1979. ISSN 00011452.

64 NGUYEN, T.-K.; VO, T. P.; THAI, H.-T. Vibration and buckling analysis of functionally graded sandwich plates with improved transverse shear stiffness based on the first-order shear deformation theory. **Proceedings of the Institution of Mechanical Engineers**, v. 24, n. August, p. 1–44, 2013. ISSN 1741-0398.

65 GRUTTMANN, F.; WAGNER, W. Shear correction factors for layered plates and shells. **Computational Mechanics**, Springer Berlin Heidelberg, v. 59, n. 1, p. 129–146, 2017. ISSN 01787675.

66 HUGHES, T.; COTTRELL, J.; BAZILEVS, Y. Isogeometric analysis: Cad, finite elements, nurbs, exact geometry and mesh refinement. **Computer Methods in Applied Mechanics and Engineering**, v. 194, n. 39, p. 4135 – 4195, 2005. ISSN 0045-7825.

67 SHI, P.; DONG, C.; SUN, F.; LIU, W.; HU, Q. A new higher order shear deformation theory for static, vibration and buckling responses of laminated plates with the isogeometric analysis. **Composite Structures**, Elsevier, v. 204, n. June, p. 342–358, 2018. ISSN 02638223. Disponível em: <https://doi.org/10.1016/j.compstruct.2018.07.080>.

68 PRACIANO, J. S. C.; BARROS, P. S. B.; BARROSO, E. S.; PARENTE, E.; HOLANDA, A. S.; SOUSA, J. B. M. An isogeometric formulation for stability analysis of laminated plates and shallow shells. **Thin-Walled Structures**, v. 143, p. 106224, 2019.

69 AUAD, S. P.; PRACIANO, J. S. C.; BARROSO, E. S.; SOUSA, J. B. M.; PARENTE, E. Isogeometric analysis of fgm plates. **Materials Today: Proceedings**, v. 8, p. 738–746, 2019.

70 BARROSO, E. **Análise e Otimizacão de Estruturas Laminadas Utilizando a Formulacão Isogeométrica**. 163 p. Tese (Master of Civil Engineering) — Universidade Federal do Ceará, 2015.

71 AUAD, S. P. **Análise Isogeométrica de Cascas Cilíndricas de Materiais com Gradação Funcional**. 93 p. Tese (Master of Civil Engineering) — Universidade Federal do Ceará, 2019.

72 PIEGL, L.; TILLER, W. **The NURBS Book (2nd Ed.)**. Berlin, Heidelberg: Springer-Verlag, 1997. ISBN 3540615458.

73 COOK, R.; MALKUS, D.; PLESHA, M.; WITT, R. J. **Concepts and Applications of Finite Element Analysis**. 4. ed. [S.l.]: John Wiley & Sons, 2002.

74 SURESH, S.; P.B, S.; RAO, A. Particle swarm optimization approach for multi-objective composite box-beam design. **Composite Structures**, v. 81, p. 598–605, 12 2007.

75 SÖRENSEN, K. Metaheuristics-the metaphor exposed. **International Transactions in Operational Research**, p. 1–16, 2013. ISSN 14753995.

76 JR, I. F.; YANG, X.-s.; FISTER, I.; BREST, J. A Brief Review of Nature-Inspired Algorithms for. v. 80, n. 3, p. 1–7, 2013. ISSN 00135852.

77 LAGAROS, N. D.; PAPADRAKAKIS, M.; KOKOSSALAKIS, G. Structural optimization using evolutionary algorithms. **Computers Structures**, v. 80, n. 7, p. 571 – 589, 2002. ISSN 0045-7949.

78 KOU, X.; PARKS, G.; TAN, S. Optimal design of functionally graded materials using a procedural model and particle swarm optimization. **Computer-Aided Design**, v. 44, n. 4, p. 300 – 310, 2012. ISSN 0010-4485.

79 RICHE, R. L.; HAFTKA, R. T. Optimization of laminate stacking sequence for buckling load maximization by genetic algorithm. **AIAA Journal**, v. 31, n. 5, p. 951–956, 1993. ISSN 0001-1452. Disponível em: <http://arc.aiaa.org/doi/10.2514/3.11710>.

80 JING, Z.; FAN, X.; SUN, Q. Stacking sequence optimization of composite laminates for maximum buckling load using permutation search algorithm. **Composite Structures**, Elsevier Ltd, v. 121, p. 225–236, 2015. ISSN 02638223.

81 HUANG, L.; NG, C.-T.; SHEIKH, A. H.; GRIFFITH, M. C. Niching particle swarm optimization techniques for multimodal buckling maximization of composite laminates. **Applied Soft Computing**, Elsevier B.V., v. 57, p. 495–503, 2017. ISSN 15684946.

82 LIU, B.; T. Haftka, R.; A. Akgün, M.; TODOROKI, A. Permutation genetic algorithm for stacking sequence design of composite laminates. **Computer Methods in Applied Mechanics and Engineering**, v. 186, n. 2-4, p. 357–372, 2000. ISSN 00457825.

83 APALAK, M. K.; YILDIRIM, M.; EKICI, R. Layer optimisation for maximum fundamental frequency of laminated composite plates for different edge conditions. **Composites Science and Technology**, v. 68, n. 2, p. 537–550, 2008. ISSN 02663538.

84 SADR, M. H.; Ghashochi Bargh, H. Optimization of laminated composite plates for maximum fundamental frequency using Elitist-Genetic algorithm and finite strip method. **Journal of Global Optimization**, v. 54, n. 4, p. 707–728, 2012. ISSN 09255001.

85 RAHUL; SANDEEP, G.; CHAKRABORTY, D.; DUTTA, A. Multi-objective optimization of hybrid laminates subjected to transverse impact. **Composite Structures**, v. 73, n. 3, p. 360–369, 2006. ISSN 02638223.

86 GHASEMI, A. R.; HAJMOHAMMAD, M. H. Multi-objective optimization of laminated composite shells for minimum mass/cost and maximum buckling pressure with failure criteria under external hydrostatic pressure. **Structural and Multidisciplinary Optimization**, 2017. ISSN 16151488.

87 NA, K.-S.; KIM, J.-H. Optimization of volume fractions for functionally graded panels considering stress and critical temperature. **Composite Structures**, v. 89, n. 4, p. 509 – 516, 2009. ISSN 0263-8223.

88 TAHERI, A.; HASSANI, B.; MOGHADDAM, N. Thermo-elastic optimization of material distribution of functionally graded structures by an isogeometrical approach. **International Journal of Solids and Structures**, v. 51, n. 2, p. 416 – 429, 2014. ISSN 0020-7683. Disponível em: <http://www.sciencedirect.com/science/article/pii/S0020768313004034>.

89 KENNEDY, J.; EBERHART, R. Particle swarm optimization. **Neural Networks, 1995. Proceedings., IEEE International Conference on**, v. 4, p. 1942–1948 vol.4, 1995. ISSN 19353812.

90 Kennedy, J.; Mendes, R. Neighborhood topologies in fully informed and best-of-neighborhood particle swarms. **IEEE Transactions on Systems, Man, and Cybernetics, Part C (Applications and Reviews)**, v. 36, n. 4, p. 515–519, July 2006. ISSN 1558-2442.

91 Kennedy, J.; Mendes, R. Population structure and particle swarm performance. In: **Proceedings of the 2002 Congress on Evolutionary Computation. CEC'02 (Cat. No.02TH8600)**. [S.l.: s.n.], 2002. v. 2, p. 1671–1676 vol.2.

92 BRATTON, D.; KENNEDY, J. Defining a standard for particle swarm optimization. **2007 IEEE Swarm Intelligence Symposium**, 2007.

93 CLERC, M. **Standard Particle Swarm Optimisation**. [S.l.]: hal-00764996, 2012. 1–16 p.

94 DEB, K. An efficient constraint handling method for genetic algorithms. **Computer Methods in Applied Mechanics and Engineering**, v. 186, n. 2, p. 311 – 338, 2000. ISSN 0045-7825.

95 ALMEIDA, F. S.; AWRUCH, A. M. Design optimization of composite laminated structures using genetic algorithms and finite element analysis. **Composite Structures**, Elsevier Ltd, v. 88, n. 3, p. 443–454, 2009. ISSN 0263-8223.

96 ROCHA, I. B. C. M. **Análise e otimização de cascas laminadas considerando não-linearidade geométrica e falha progressiva**. 165 p. Tese (Masters of Civil Engineering) — Universidade Federal do Ceará, 2013.

97 MULLUR, A. A.; MESSAC, A. Metamodeling using extended radial basis functions: A comparative approach. **Engineering with Computers**, v. 21, n. 3, p. 203–217, 2006. ISSN 01770667.

98 SONG, X.; LV, L.; SUN, W.; ZHANG, J. A radial basis function-based multi-fidelity surrogate model: exploring correlation between high-fidelity and low-fidelity models. **Structural and Multidisciplinary Optimization**, Structural and Multidisciplinary Optimization, 2019. ISSN 1615-147X.

99 NIK, M. A.; FAYAZBAKHSH, K.; PASINI, D.; LESSARD, L. A comparative study of metamodeling methods for the design optimization of variable stiffness composites. **Composite Structures**, Elsevier Ltd, v. 107, p. 494–501, 2014. ISSN 02638223.

100 SIMPSON, T. W.; LIN, D. K. J.; CHEN, W. Sampling Strategies for Computer Experiments: Design and Analysis. **International Journal of Reliability and Applications**, v. 2, n. 3, p. 209–240, 2001. ISSN 1598-0073.

101 JAISWAL, P.; PATEL, J.; RAI, R. Build orientation optimization for additive manufacturing of functionally graded material objects. **International Journal of Advanced Manufacturing Technology**, The International Journal of Advanced Manufacturing Technology, v. 96, n. 1-4, p. 223–235, 2018. ISSN 14333015.

102 WANG, G. G.; SHAN, S. Review of Metamodeling Techniques in Support of Engineering Design Optimization. **Journal of Mechanical Design**, p. 1–42, 2006.

103 ZHAO, D.; XUE, D. A comparative study of metamodeling methods considering sample quality merits. **Structural and Multidisciplinary Optimization**, v. 42, n. 6, p. 923–938, 2010. ISSN 1615147X.

104 CARDOZO, S. D.; GOMES, H. M.; AWRUCH, A. M. Optimization of laminated composite plates and shells using genetic algorithms , neural networks and finite elements. **Latin Amarican Journal of Solid and Structures**, v. 8, p. 413–427, 2011.

105 FORSBERG, J.; NILSSON, L. On polynomial response surfaces and Kriging for use in structural optimization of crashworthiness. **Structural and Multidisciplinary Optimization**, v. 29, n. 3, p. 232–243, 2005. ISSN 1615147X.

106 JIN, S.-s.; JUNG, H.-j. Sequential surrogate modeling for efficient finite element model updating. **Computers and Structures**, Elsevier Ltd, v. 168, p. 30–45, 2016. ISSN 0045-7949.

107 AMOUZGAR, K.; STRÖMBERG, N. Radial basis functions as surrogate models with a priori bias in comparison with a posteriori bias. **Structural and Multidisciplinary Optimization**, v. 55, n. 4, p. 1453–1469, Apr 2017. ISSN 1615-1488.

108 De Ath, G.; EVERSON, R. M.; RAHAT, A. A. M.; FIELDSEND, J. E. Greed is Good: Exploration and Exploitation Trade-offs in Bayesian Optimisation. n. November, 2019. Disponível em: <http://arxiv.org/abs/1911.12809>.

109 KALAGNANAM, J. R.; DIWEKAR, U. M. An efficient sampling technique for off-line quality control. **Technometrics**, [Taylor Francis, Ltd., American Statistical Association, American Society for Quality], v. 39, n. 3, p. 308–319, 1997. ISSN 00401706. Disponível em: <http://www.jstor.org/stable/1271135>.

110 HAMMERSLEY, J. M. Monte carlo methods for solving multivariable problems. **Annals of the New York Academy of Sciences**, v. 86, n. 3, p. 844–874, 1960. Disponível em: <https://nyaspubs.onlinelibrary.wiley.com/doi/abs/10.1111/j.1749-6632.1960.tb42846.x>.

111 STEPONAVIČė, I.; SHIRAZI-MANESH, M.; HYNDMAN, R. J.; SMITH-MILES, K.; VILLANOVA, L. On Sampling Methods for Costly Multi-Objective Black-Box Optimization. In: **Advances in Stochastic and Deterministic Global Optimization**. [S.l.: s.n.], 2016. v. 107, p. 273–296. ISBN 978-3-319-29973-0.

112 CHO, I.; LEE, Y.; RYU, D.; CHOI, D. H. Comparison study of sampling methods for computer experiments using various performance measures. **Structural and Multidisciplinary Optimization**, Structural and Multidisciplinary Optimization, v. 55, n. 1, p. 221–235, 2017. ISSN 16151488.

113 MORRIS, M. D.; MITCHELL, T. J. Exploratory designs for computational experiments. **Journal of Statistical Planning and Inference**, v. 43, n. 3, p. 381 – 402, 1995. ISSN 0378-3758.

114 MASCHIO, C.; SCHIOZER, D. J. Journal of Petroleum Science and Engineering Probabilistic history matching using discrete Latin Hypercube sampling and nonparametric density estimation. **Journal of Petroleum Science and Engineering**, Elsevier, v. 147, p. 98–115, 2016. ISSN 0920-4105.

115 SACKS, J.; WELCH, W. J.; MITCHELL, T. J.; WYNN, H. P. Design and Analysis of Computer Experiments. **Statistical Science**, v. 4, n. 4, p. 409–435, 1989.

116 JONES, D. R. A Taxonomy of Global Optimization Methods Based on Response Surfaces. **Journal of Global Optimization**, v. 21, n. 4, p. 39, 2001. ISSN 09255001.

117 SNOEK, J.; LAROCHELLE, H.; ADAMS, R. P. Practical bayesian optimization of machine learning algorithms. In: **Proceedings of the 25th International Conference on Neural Information Processing Systems - Volume 2**. Red Hook, NY, USA: Curran Associates Inc., 2012. (NIPS'12), p. 2951–2959.

118 KIANIFAR, M. R.; CAMPEAN, F. Performance evaluation of metamodelling methods for engineering problems: towards a practitioner guide. **Structural and Multidisciplinary Optimization**, 07 2019.

119 NEAL, R. M. **Bayesian Learning for Neural Networks**. 195 p. Tese (Doctor of Philosophy) — University of Toronto, 1995.

120 RASMUSSEM, C. E.; WILLIAMS, C. K. I. **Gaussian Processes for Machine Learning**. [S.l.]: The MIT Press, 2006. 266 p. ISBN 026218253X.

121 ELSAYED, K.; LACOR, C. Robust parameter design optimization using Kriging, RBF and RBFNN with gradient-based and evolutionary optimization techniques. **Applied Mathematics and Computation**, Elsevier Inc., v. 236, p. 325–344, 2014. ISSN 00963003.

122 WANG, J. T.; WANG, C. J.; ZHAO, J. P. Frequency response function-based model updating using Kriging model. **Mechanical Systems and Signal Processing**, Elsevier, v. 87, n. August 2016, p. 218–228, 2017. ISSN 0888-3270.

123 BACHOC, F. Cross validation and maximum likelihood estimations of hyper-parameters of Gaussian processes with model misspecification. **Computational Statistics and Data Analysis**, v. 66, n. 0, p. 55–69, 2013. ISSN 01679473.

124 MYUNG, I. J. Tutorial on maximum likelihood estimation. **Journal of Mathematical Psychology**, v. 47, n. 1, p. 90–100, 2003. ISSN 00222496.

125 DAVIS, G. J.; MORRIS, M. D. Six factors which affect the condition number of matrices associated with kriging. **Mathematical Geology**, v. 29, n. 5, p. 669–683, 1997. ISSN 08828121.

126 ROUSTANT, O.; GINSBOURGER, D.; DEVILLE, Y. Dicekriging, diceoptim: Two r packages for the analysis of computer experiments by kriging-based metamodeling and optimization. **Journal of Statistical Software, Articles**, v. 51, n. 1, p. 1–55, 2012. ISSN 1548-7660.

127 JONES, D. R.; SCHONLAU, M.; W. J. Welch. Efficient Global Optimization of Expensive Black-Box Functions. **Journal of Global Optimization**, v. 13, p. 455–492, 1998.

128 TUTUM, C. C.; DEB, K.; BARAN, I. Constrained efficient global optimization for pultrusion process. **Materials and Manufacturing Processes**, Taylor Francis, v. 30, n. 4, p. 538–551, 2015.

129 WU, Z.; WANG, D.; Okolo N., P.; JIANG, Z.; ZHANG, W. Unified estimate of Gaussian kernel width for surrogate models. **Neurocomputing**, v. 203, p. 41–51, 2016.

130 NAKAYAMA, H.; ARAKAWA, M.; SASAKI, R. Simulation-based optimization using computational intelligence. **Optimization and Engineering**, v. 3, n. 2, p. 201–214, Jun 2002. ISSN 1573-2924.

131 KITAYAMA, S.; ARAKAWA, M.; YAMAZAKI, K. Sequential Approximate Optimization using Radial Basis Function network for engineering optimization. **Optim. Eng. Journal**, p. 535–557, 2011.

132 KITAYAMA, S.; YAMAZAKI, K. Simple estimate of the width in Gaussian kernel with adaptive scaling technique. **Applied Soft Computing Journal**, Elsevier B.V., v. 11, n. 8, p. 4726–4737, 2011. ISSN 1568-4946.

133 FERREIRA, A.; FASSHAUER, G.; BATRA, R.; RODRIGUES, J. Static deformations and vibration analysis of composite and sandwich plates using a layerwise theory and rbf-ps discretizations with optimal shape parameter. **Composite Structures**, v. 86, p. 328–343, 12 2008.

134 MECKESHEIMER, M.; BOOKER, A. J.; BARTON, R.; SIMPSON, T. W. Computationally inexpensive metamodel assessment strategies. **AIAA Journal**, v. 40, n. 10, p. 2053–2060, 2012. ISSN 0001-1452.

135 SÓBESTER, A.; LEARY, S. J.; KEANE, A. J. On the design of optimization strategies based on global response surface approximation models. **Journal of Global Optimization**, v. 33, n. 1, p. 31–59, 2005. ISSN 09255001.

136 MEHMANI, A.; CHOWDHURY, S.; MEINRENKEN, C.; MESSAC, A. Concurrent surrogate model selection (cosmos): Optimizing model type, kernel function, and hyper-parameters. **Struct. Multidiscip. Optim.**, Springer-Verlag, Berlin, Heidelberg, v. 57, n. 3, p. 1093–1114, mar. 2018. ISSN 1615-147X.

137 RIBEIRO, L. G.; MAIA, M. A. Comparative Study on Multiple Width-Defining Methods for Radial Basis Functions. In: **XL Ibero-Latin American Congress on Computational Methods in Engineering**. Natal, RN: [s.n.], 2019. p. 1–20.

138 SCHMIT, L.; FARSHI, B. Some approximation concepts for structural synthesis. **AIAA Journal**, v. 12, n. 5, p. 692–699, 1974.

139 KUSHNER, H. J. A new method of locating the maximum point of an arbitrary multipeak curve in the presence of noise. **Journal of Basic Engineering**, v. 86, 01 1964.

140 SCHONLAU, M.; WELCH, W.; JONES, D. Global versus local search in constrained optimization of computer models. In: ____. [S.l.: s.n.], 1998. v. 34, p. 11–25.

141 JONES, D. R. A taxonomy of global optimization methods based on response surfaces. **Journal of Global Optimization**, v. 21, n. 4, p. 345–383, Dec 2001. ISSN 1573-2916.

142 ANDREWS, L. C. **Special functions of mathematics for engineers**. Bellingham, Wash., USA : Oxford: SPIE Optical Engineering Press ; Oxford University Press, 1998. ISBN 9780819426161.

143 MOCKUS, J.; TIESIS, V.; ZILINSKAS, A. The application of bayesian methods for seeking the extremum. In: ____. [S.l.: s.n.], 1978. v. 2, p. 117–129. ISBN 0-444-85171-2.

144 GAN, N.; GU, J. Hybrid meta-model-based design space exploration method for expensive problems. **Structural and Multidisciplinary Optimization**, Structural and Multidisciplinary Optimization, p. 907–917, 2018. ISSN 16151488.

145 GELBART, M. A.; SNOEK, J.; ADAMS, R. P. Bayesian Optimization with Unknown Constraints. In: **Proceedings of the Thirtieth Conference on Uncertainty in Artificial Intelligence**. Quebec City, Quebec, Canada: AUAI Press, 2014. p. 1–14.

146 LOCATELLI, M. Bayesian Algorithms for One-Dimensional Global Optimization. **Journal of Global Optimization**, v. 10, n. 1, p. 57–76, 1997. ISSN 09255001.

147 SCHONLAU, M.; WELCH, W. J. .; JONES, D. R. . Global versus Local Search in Constrained Optimization of Computer Models. **New Developments and Applications in Experimental Design**, v. 34, p. 11–25, 1998.

148 ZHAN, D.; XING, H. Expected improvement for expensive optimization: a review. **Journal of Global Optimization**, Springer Science and Business Media LLC, jul. 2020. Disponível em: <https://doi.org/10.1007/s10898-020-00923-x>.

149 BALREIRA, D. S. **Otimização Sequencial Aproximada de Estruturas Laminadas de Material Compósito**. 97 p. Tese (Master of Civil Engineering) — Universidade Federal do Ceará, 2018.

150 FRANCO, V. M.; MADEIRA, J. F. A.; ARAÚJO, A. L.; MOTA, C. M. Multiobjective optimization of ceramic-metal functionally graded plates using a higher order model. **Composite Structures**, Elsevier Ltd, v. 183, p. 146–160, 2018. ISSN 0263-8223.

151 SMITH, M. **ABAQUS/Standard User's Manual, Version 6.9**. United States: Dassault Systèmes Simulia Corp, 2009.

152 KIM, K.-D.; LOMBOY, G.; HAN, S.-C. Geometrically non-linear analysis of functionally graded material (fgm) plates and shells using a four-node quasi-conforming shell element. **Journal of Composite Materials - J COMPOS MATER**, v. 42, p. 485–511, 03 2008.

153 NGUYEN, H. M.; COUCKUYT, I.; KNOCKAERT, L.; DHAENE, T.; GORISSEN, D.; SAEYS, Y. An Alternative Approach to Avoid Overfitting for Surrogate Models. In: **2011 Winter Simulation Conference**. Phoenix, AZ, USA: [s.n.], 2011. p. 2760–2771. ISBN 9781457721090.